atmosphere. As mentioned earlier, CO^+ is highly variable with solar activity and not by season, resulting in substantial solar cycle variability in the production of hot carbon by dissociative recombination of CO^+. Furthermore, the horizontal distribution of CO^+ is anticorrelated with that of O_2^+, because CO^+ charge exchanges with CO_2 immediately in the thermosphere (as detailed description in Paper I). The resulting hot carbon density distribution, thus, exhibits different horizontal distribution than that of hot oxygen.

CO^+ is one of the major ionospheric species that is produced mainly by photochemical processes. CO^+ is predominantly produced through photoionization of CO and photodissociative ionization of CO_2, which are highly sensitive to the solar EUV flux in the upper atmosphere. The newly produced CO^+ ions quickly charge exchange with CO_2 deep in the thermosphere, forming a horizontal distribution pattern that is anticorrelated to that of O_2^+. O_2^+ is generated through charge exchange between CO_2^+ and O, where the parent sources are directly related to the local background O and CO_2. The main removal process for O_2^+ is dissociative recombination of O_2^+, which allows O_2^+ to retain similar solar cycle and seasonal variability as that of neutral background species. However, CO^+ displays inverse behavior because its loss process is tightly related to the local CO_2 density.
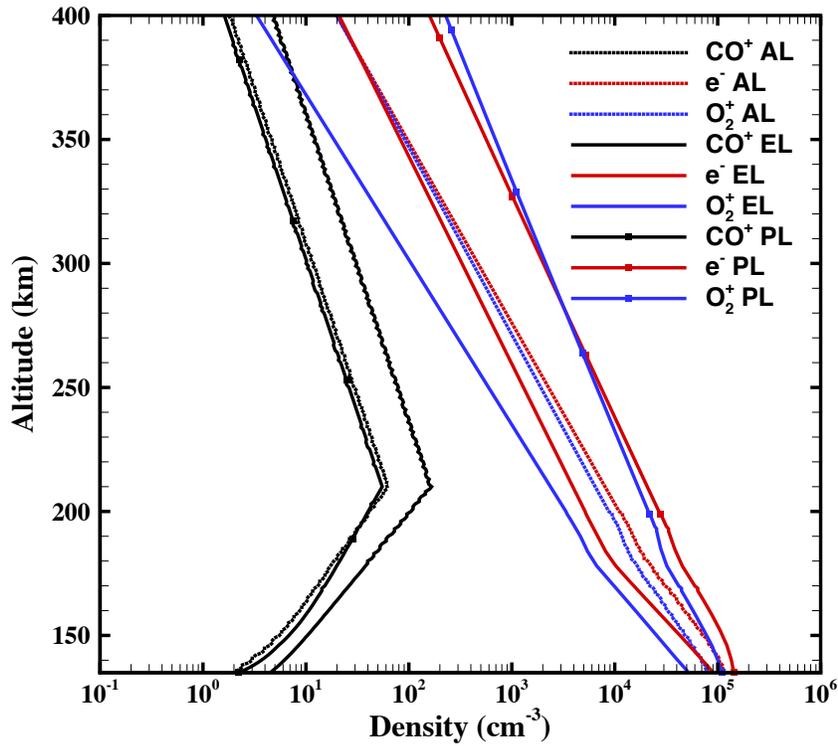
Figure 6.4. Background ion density altitude profiles for the AL, EL, and PL cases.

A change in solar activity, which can be characterized as a variation of the solar EUV flux, expands the thermosphere and ionosphere and enhances the densities of the local thermospheric and ionospheric constituents. The overall magnitude of the ionospheric density increases by about an order of magnitude over the dayside as solar activity advances from low to high. As a response to the increase in the solar EUV flux, the magnitude of the O_2^+ peak density is enhanced, while the peak height of O_2^+ does not appreciably change since the nominal O_2^+ peak is situated in the lower thermosphere region; *i.e.,* altitudes near/below ~120 km are subject to the solar IR flux which do not vary over the solar cycle [*Valeille et al.*, 2009b]. On the other hand, CO^+ displays different responses to the solar EUV flux variation due to its different characteristic altitude profile in the upper atmosphere. As explained in detail in *Lee et al.* [2014a],

the nominal density peak of CO^+ is located above 200 km both for the low and high solar activity cases because of its parent sources and production and loss reactions. The upper atmosphere will be more affected by the solar EUV flux than the lower atmosphere, and CO^+ density near its peak changes according to the mixing ratio of the parent sources. As a result, both the peak height and the magnitude of the peak of CO^+ are highly variable with solar cycle. Different scale heights and peak altitudes for the low and high solar activity cases are adopted. These parameters determine the solar cycle variability in the upper atmosphere where the escape to space is important.

The seasonal responses in the thermosphere and ionosphere are characterized as the expansion of the lower atmosphere mostly by the IR flux. The solar IR flux on Mars varies as solar longitude (L_s) and heliocentric distance change. Because the O_2^+ density peak is located where the ionosphere is influenced more by IR flux, seasonal variability is more apparent in O_2^+; the peak height is at an altitude of about 120 km and varies by $+12 - 15$ km from the AL case to the PL case [*Valeille et al.,* 2009b]. By contrast, the seasonal change on Mars affects CO^+ to a lesser degree than O_2^+, due to the different source dependency in the thermosphere. As shown in figure 6.4, the production of CO^+ is maximized in the upper atmosphere where IR radiation is not effectively absorbed. Although the magnitude of the CO^+ density increases in response to the seasonal change from the aphelion to perihelion cases, the seasonal variability for CO^+ is quite minimal compared to the solar cycle variability for CO^+. Since the lower altitude region contains hot C particles that do not ultimately manage to escape to space, the overall escape rate does not show pronounced differences with season.

Several space missions have measured the electron density profile by the radio occultation method [*e.g., Hinson et al.,* 2001; *Zhang et al.,* 1990; *Pätzold et al.,* 2005], for

middle and high solar zenith angles near the terminator during different solar activity periods. Overall, the peak height of electron density is observed to increase while its magnitude decreases. The scale height decreases as solar zenith angle increases, due to the possible interaction of the solar wind with the upper thermosphere [*Fox and Yeager*, 2006].

VI.3. Results and discussion

VI.3.1. Local features and structure of the hot carbon corona

In this study, the global dynamics of hot carbon and its variations with the solar cycle and seasons are simulated. As discussed previously, the hot particle criterion in the model is set by the value of $V_{threshold}$. The model particle in the computational domain is determined as a hot species when its speed exceeds the local $V_{threshold}$. For counting all hot carbon (*i.e.*, including ones that can be thermalized before they escape), the $V_{threshold}$ is defined as twice the local thermal speed corresponding to the background atmospheric temperature [*Lee et al.*, 2014a; *Valeille et al.*, 2010a]. The definition of the $V_{threshold}$ is important, since the local thermalization rate depends on the local thermospheric parameters (*e.g.*, background temperatures, source rate, and frequency of collisions with background atmosphere), which results in a variation in the spatial distribution of hot carbon from the source mechanisms. This variation in the hot carbon corona is described in detail in the following sections. Two dominant source reactions, photodissociation of CO and dissociative recombination of CO^+, display different features in the simulated hot carbon distributions. Therefore, these two mechanisms are discussed individually in the following sections.

VI.3.1.1 Photodissociation of CO

As discussed in the previous section, CO is spatially distributed in the pattern that resembles elements from that of thermal CO_2 and of thermal O features. Figure 6.5 shows the variation of hot carbon density produced by photodissociation of CO over the solar cycle for the equinox and perihelion cases, respectively, in the noon-midnight plane. While the spatial distribution over the planet does not change significantly as the solar cycle advances, the hot carbon density is enhanced by about a factor of $9 - 10$. As the color contours show in figure 6.5, the density distribution peaks globally on the dayside only and extends over the poles as it decreases by about an order of magnitude. The hot density distribution shows an abrupt decrease on the nightside and a tenuous coverage. The low hot carbon density on the nightside is an important feature resulting from the effect of gravity on particles that are produced in the dayside; *i.e.,* moving away from Mars in the anti-sunward direction and known as the 'bouncing' effect [*Valeille et al.,* 2010a].
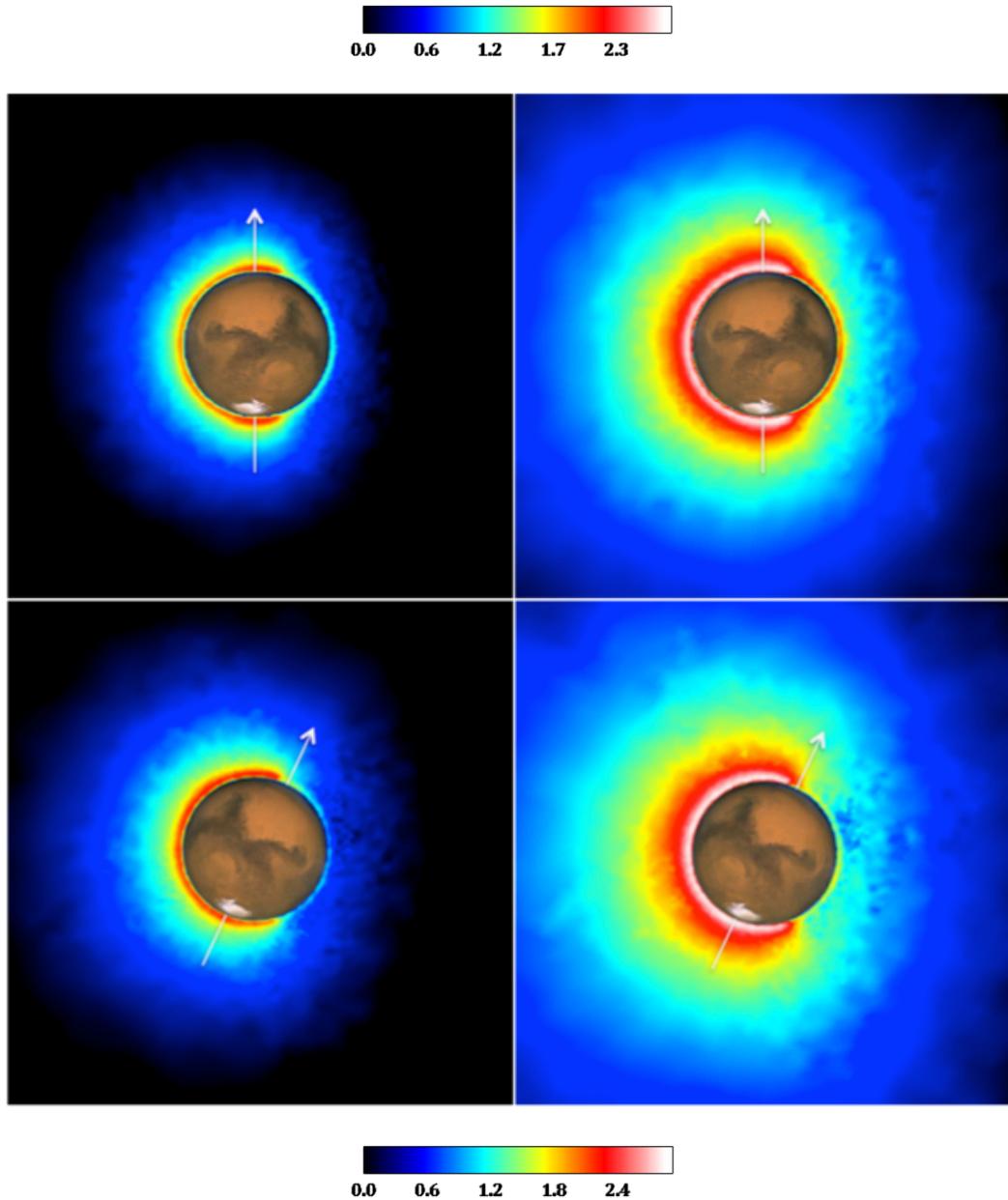
Figure 6.5. From left to right, hot C produced from photodissociation of CO for the EL and EH cases (top) and the PL and PH cases (bottom). Sun-Mars meridian plane with the Sun toward the left. The color scale indicates the log of the hot C density (cm^{-3}).

Seasonal variation on Mars is driven by several factors. The variable solar EUV flux (about ±22%), due to the large orbital eccentricity of Mars, controls the thermospheric circulation. This thermospheric circulation is further modified by upward propagating tidal

and/or wave momentum forcing from the lower atmosphere [*Bell et al.,* 2007*; Bougher et al.*, 2006, 2014a; *Forget et al.,* 2009]. Seasonal variation is also characterized by the solar IR flux that influences mostly the lower atmosphere, resulting in the expansion/contraction of the lower atmosphere with the changing seasons. Variable dust loading (episodic dust storm evolution) also contributes to this seasonal expansion/contraction [*Bougher et al.* 2014a].

CO becomes an important neutral background species above an altitude where O is a dominant neutral species; this altitude ranges from ~190 km to 240 km, varying with solar activity and season. In this altitude range, the thermalization of nascent hot carbon atoms becomes locally minimized, due to the decrease in the densities of the collision partners, O and CO_2, in the background atmosphere. The resulting effect can be easily identified by the density peak in the altitude profile and the density contours. The seasonal variation is a factor of about 1.3 – 1.6 in the densities at the subsolar point of the AL and PL cases compared to that of the EL case, respectively. This variation implies that the seasonal variation in the magnitude of hot carbon density is significantly milder than the solar cycle variation. Thus, the seasonal variability of the hot carbon corona is characterized by changes in the spatial distribution and structure of the density profiles of hot carbon.
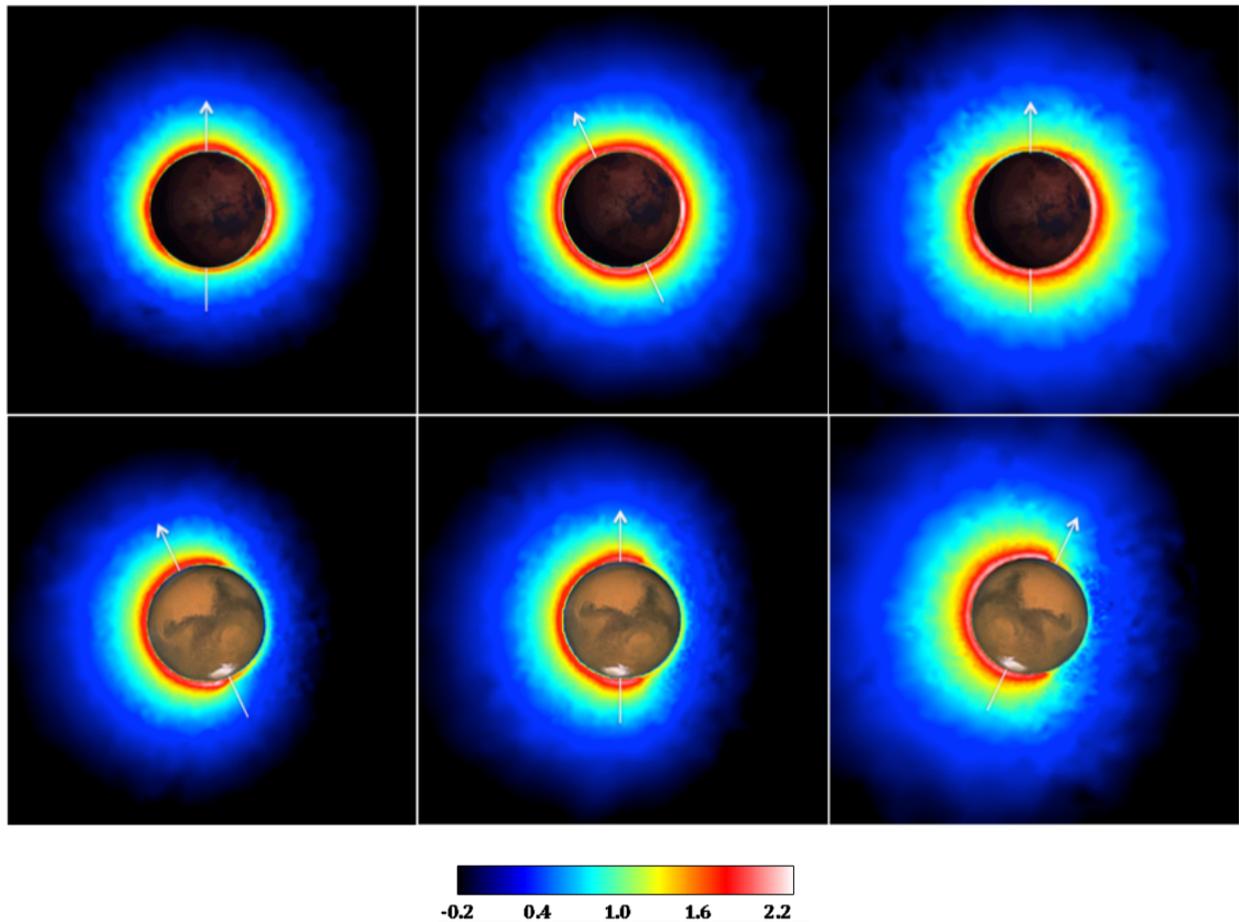
Figure 6.6. From left to right, hot C density produced from photodissociation of CO for the AL, EL, and PL cases. Tail-to-Sun view (top) and Sun-Mars meridian plane with the Sun on the left (bottom). The color scale indicates the log of the hot C density (cm^{-3}).

Among the several factors that affect the hot carbon density enhancement near the winter pole, neutral temperature and background thermospheric CO and O play the major role, with atmospheric circulation serving as a minor role. As illustrated in figure 6.6, the meridian plane view of the density distribution does not display distinctive differences over the seasons, except for the enhancements near the south and north poles for the AL and PL cases, respectively. The seasonal variability is more distinguishable in the tail-to-Sun view, as shown in figure 6.6. The locations of the highly populated regions change over the seasons, in addition to the

113

enhancement of hot density as the heliocentric distance changes. According to the map of the neutral temperature at the altitude of the lower exosphere level (figure 6.1), these highly populated regions correspond to the local minima of the neutral temperature. This feature is a logical result to expect, since the local $V_{threshold}$ is relatively low in the regions of the low neutral temperature (*e.g.*, morning terminator region). The low local velocity criterion allows the addition of the relatively lower velocity population of hot C. This slow hot C does not have enough energy to escape to space and is easily thermalized. This situation can be confirmed by increasing $V_{threshold}$ up to escape speed, which can eliminate the slow hot C without affecting the calculation of the total escape rate of hot C. More detailed description about this is given in section 6.3.4.

Thermalization of hot carbon is determined by the local macroscopic parameters such as the density of collision partners, the speed of a nascent hot carbon, and background atmospheric temperatures. Hot carbon that sustains enough energy to escape is produced more in the summer hemisphere, while a relatively large fraction of the nascent hot carbon is thermalized in the winter hemisphere. In the computational domain, the hot carbon that attains its velocity below the escape speed, but above the local $V_{threshold}$, travels along ballistic trajectories and falls back to the thermosphere because of the gravity attraction of the planet. These hot carbon atoms with relatively low velocities populate mostly the altitudes below $190 - 240$ km, beyond which the effect of collision with background atmosphere becomes negligible.

Figure 6.7 shows the escape probability of hot carbon resulting from photodissociation of CO for different levels of solar activity and seasonal effects (*i.e.,* AL/EL/PL for seasonal variability and EL/EH and PL/PH for solar cycle variability). The escape probability is plotted as a function of log pressure to eliminate the effect of atmospheric expansion and to show only the

effects from the solar cycle and seasons on the escape of hot carbon. The level where the slopes of the probability curves change and begin to converge is at a pressure level of $\sim 10^{-5}$ dyne cm^{-2}, which corresponds to 180 km – 240 km of altitude ranges for the cases considered in this study. The escape probabilities from all cases converge to 0.5 in the upper atmosphere. In 3D, 0.5 is the highest escape probability once hot particles reach the collisionless regime in the exosphere, because the radial velocity component of half of the hot population points towards the planet.

Solar cycle as well as seasonal variation is more noticeable in the lower atmosphere than in the upper atmosphere. This indicates that the solar cycle and seasonal variation plays an effective role in the collision-dominated regime, due to the variability of the background properties and hot carbon source mechanisms. As solar activity increases, the escape probability decreases by a factor of ~ 2 below an altitude of ~ 150 km and 165 km for the equinox and perihelion cases, respectively. However, the hot particles from these altitude regions are not likely to escape to space because of the high collision frequency. The seasonal variation is attributed to the change in heliocentric distance of the planet and in the lower atmosphere due to the variation in the solar IR flux. Since the production of hot carbon from photodissociation is more responsive to solar EUV flux, the variability of the escape probability by season is weaker than by solar cycle.
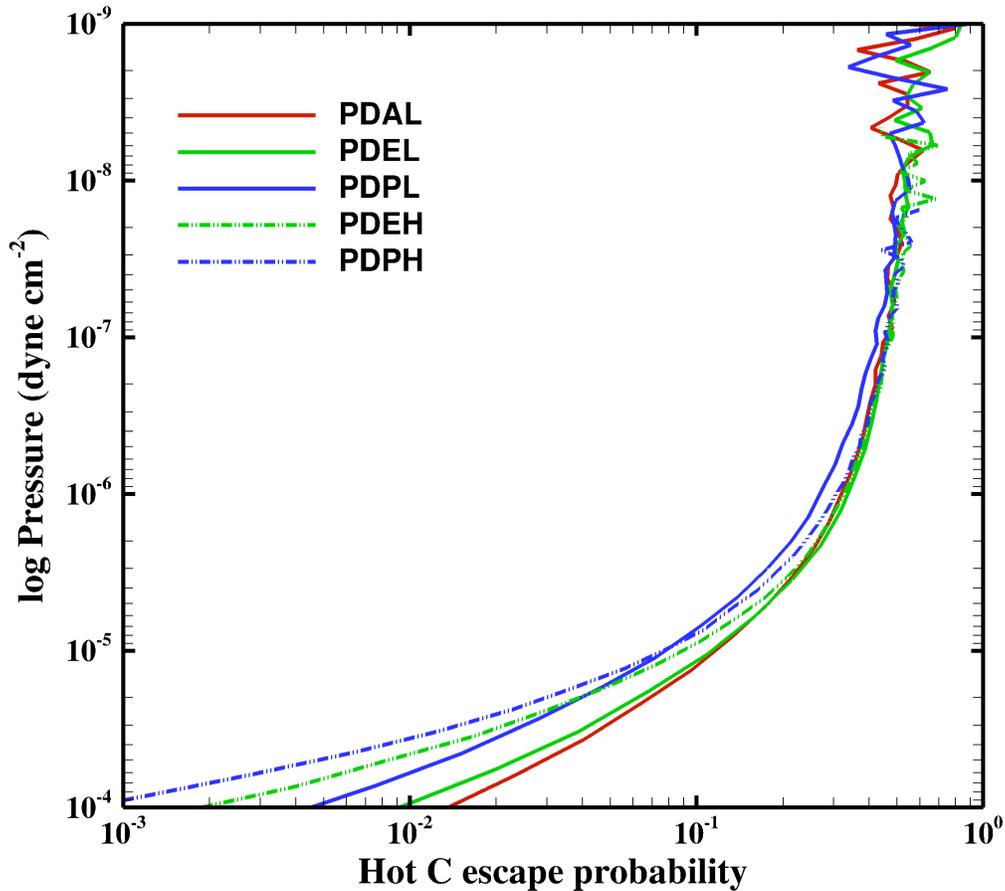
Figure 6.7. Hot carbon escape probability for photodissociation of CO case.

VI.3.1.2. Dissociative recombination of CO^+

CO^+ is one of the primary ions in the Martian ionosphere, where most of the production (*e.g.*, dissociative ionization and ionization events) in the Martian atmosphere is from photoionization of CO and photodissociative ionization of CO_2. The production rate of CO^+ increases slightly from the low to high solar activity cases, due to the increase in the CO mixing ratio [*Fox and Sung*, 2001].

The CO^+ ion distribution differs from that of the major ion, O_2^+, in several ways. The CO^+ ionospheric peak is located above an altitude of approximately 210 km and 240 km for low and high solar activity, respectively. Compared to the O_2^+ peak height (~135 km), the CO^+

density near its peak height is more sensitive to solar activity variation, since the density peak is situated where the solar EUV radiation is more effectively absorbed by the background atmosphere. As mentioned earlier, CO^+ is highly variable with solar activity and not by season, resulting in substantial solar cycle variability in the production of hot carbon by dissociative recombination of CO^+. Furthermore, the horizontal distribution of CO^+ is anticorrelated with that of O_2^+, because CO^+ charge exchanges with CO_2 immediately in the thermosphere (as detailed in the description in chapter 5 and *Lee et al.* [2014a]). The resulting hot carbon density distribution, thus, exhibits different horizontal distribution than that of hot oxygen.

Figure 6.8 presents the solar cycle variation of the hot carbon density resulting from dissociative recombination of CO^+. It is logical to expect that the density profile is spatially distributed, which is similar to the case of photodissociation of CO for the EL and EH cases – or for the PL and PH cases (solar cycle variation). The peak densities are located at high latitudes and near the terminator on the dayside, with the minima being on the nightside. The hot C density is maximized near the equator on the morning terminator due to the strong convergence of winds. The density is enhanced by a factor of about $10 - 12$ as solar activity increases. The nightside density, which is populated due to the return flux of hot carbon, increases by a similar factor, $10 - 13$.
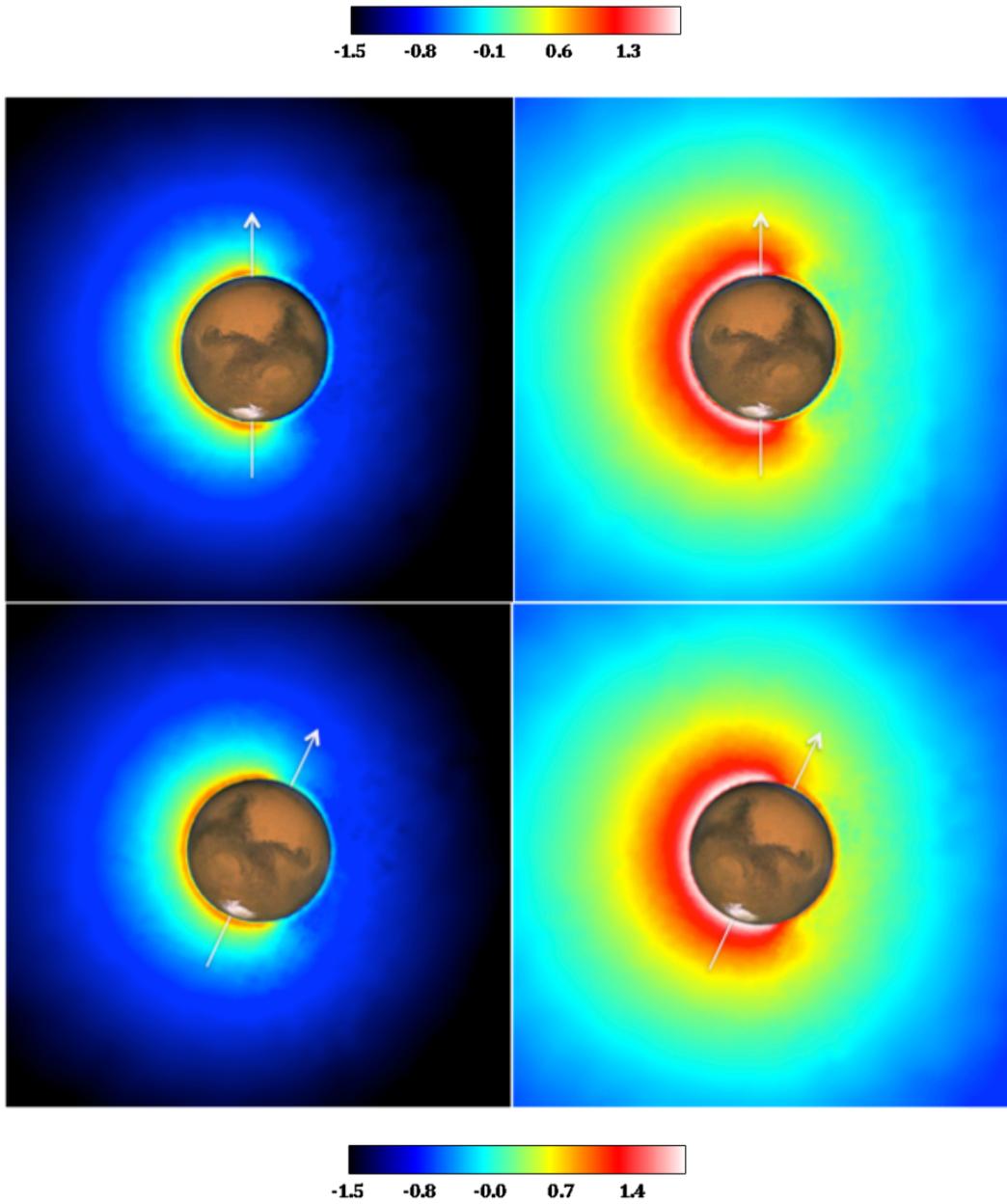
Figure 6.8. From left to right, hot C density from dissociative recombination of CO^+ for the EL and EH cases (top) and the PL and PH cases (bottom). Sun-Mars meridian plane is shown with the Sun on the left. Color scale indicates the log of the hot C density (cm^{-3}).
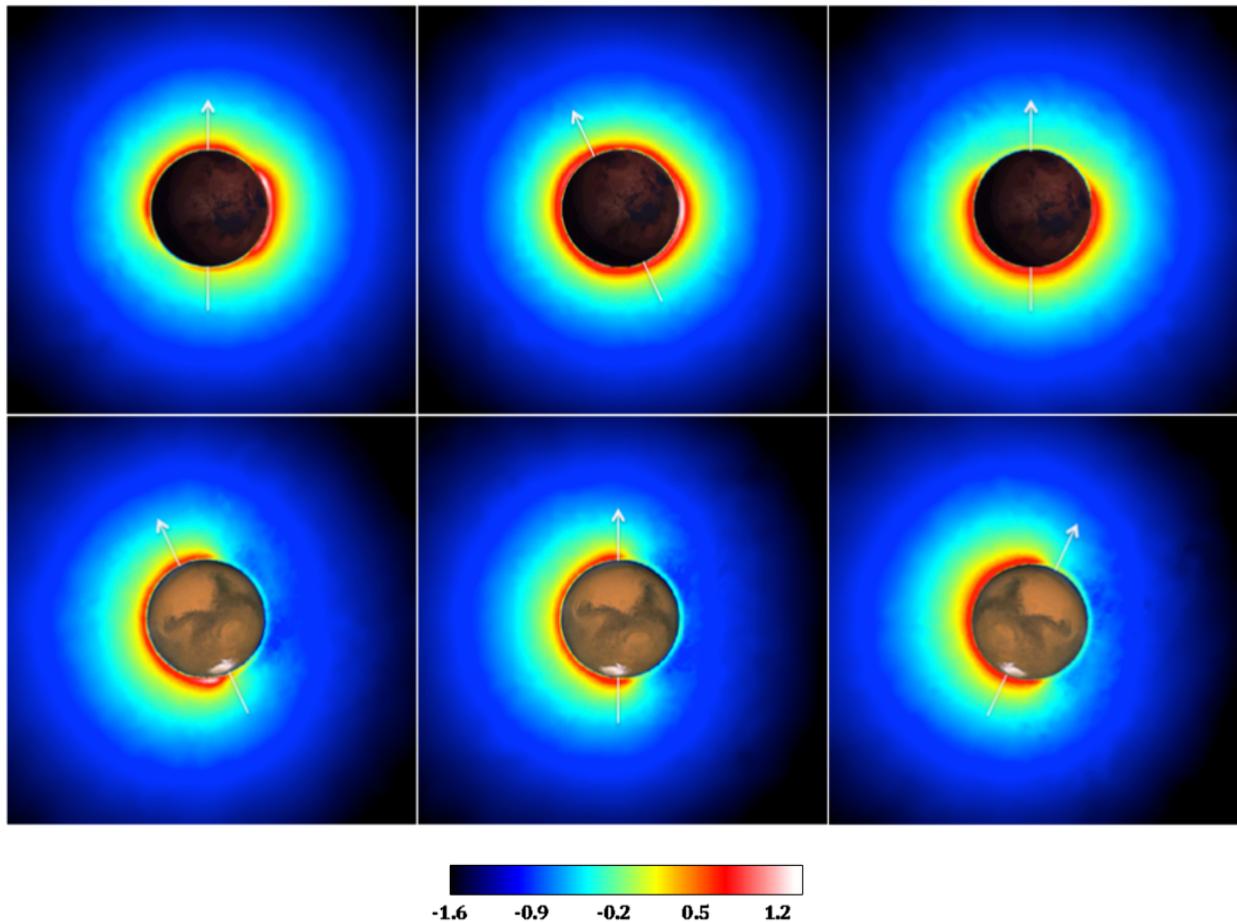
Figure 6.9. From left to right, hot C density from dissociative recombination of CO^+ for the AL, EL, and PL cases. Tail-to-Sun view (top) and Sun-Mars meridian plane with the Sun on the left (bottom). Color scale indicates the log of the hot C density (cm^{-3}).

The seasonal influence is shown as the shift of the dayside regions toward the summer pole (figure 6.9) for the aphelion and perihelion cases. Compared to the equinox case, the hot density changes by a factor of about $1.2 - 1.5$ as the heliocentric distance changes, while the density on the nightside varies only slightly. In the tail-to-Sun view, the structural variation of the hot density profile is more prominent. For the AL case, the production of hot carbon is high in the high latitudes on the morning terminator, due to the maximum of CO^+ density. The sudden density deficient region corresponds to the region of low electron and CO^+ density. For the PL

case, the winter pole and summer pole are clearly distinguishable as in the AL case. The sources for dissociative recombination of CO^+ (*i.e.*, electron and CO^+) are situated mostly on the dayside, which generate this clear distinction between the winter and summer pole.

Escape is controlled mainly by the two factors: local thermalization and production rate. The enhanced escape is shown in the AL case (figure 6.9, in the meridian plane and the tail-to-Sun view) near the southern winter pole, at altitude of about 240 km, and in the high latitudes at the morning terminator. These regions are where the production rate remains substantial, and the collision rate between the nascent hot carbon and background atmosphere becomes the lowest. On the nightside, hot carbon from the 'bouncing' effect [*Valeille et al.,* 2010a] has less of a chance to escape to space due to the deceleration and significantly lower collisional frequency.

As in the case of photodissociation of CO, the escape probability (figure 6.10) resulting from dissociative recombination of CO^+ shows a similar behavior as a function of log pressure. The seasonal effect on the Martian atmosphere appears as the change in the pressure and density in the lower background atmosphere. The variation of the escape probability for different seasons is not significant in the upper atmosphere. The escape probability decreases by a factor of about $1.5 - 2$ deep in the thermosphere - below altitudes of ~160 km or 175 km for the aphelion and perihelion cases, respectively. The effect of increase in solar activity is characterized by the enhancement in the whole atmosphere by the increased solar flux. The collisionless regime is shifted to slightly higher altitudes in the high solar activity case than in the low solar activity case.
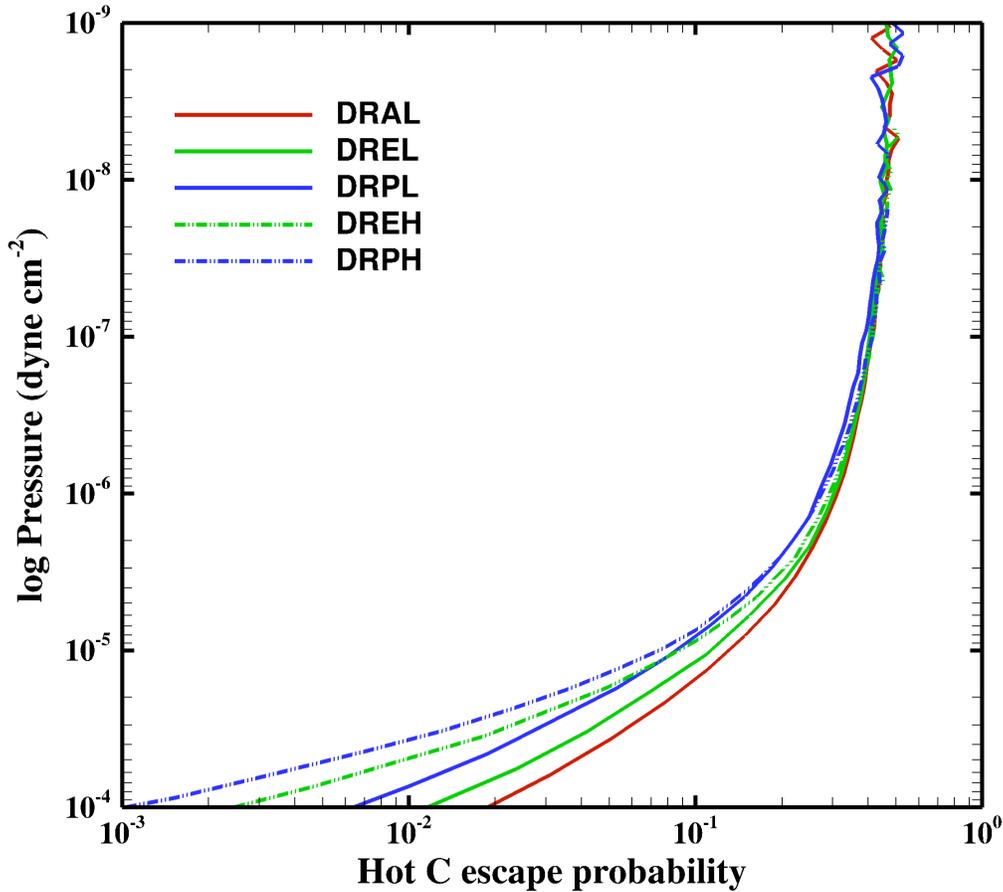
Figure 6.10. Hot carbon escape probability from dissociative recombination of CO^+ case.

VI.3.2. Escape flux of hot carbon

Due to the spatial distribution of the production and loss of the hot C population, the map of escape flux at some distance away from the planet displays different local values in response to the variation in solar cycle and season. In the vicinity of the upper boundary of the computational domain, the local macroscopic parameters exhibit small fluctuations in their quantities over the dayside, because all the features of hot population are averaged over a larger region. The escape flux map also shows the smooth variation of the hot population escape in the regions from the dayside to the terminators to the nightside.

Figure 6.11a illustrates the effect of the variation in solar activity level on the escape flux resulting from photodissociation of CO at 1 Mars radius above the surface, or about 6800 km from the center of Mars. As for the density distribution, the solar cycle variability does not induce a change spatial distribution of the low and high escape flux regions but enhances the magnitude of the escape flux as the solar EUV flux increases. The maxima of the escape flux are located at the subsolar point, whereas all the minima are located on the nightside near the anti-subsolar point. The variation in the escape flux over the solar cycle is a factor of about 2.5 (EL to EH) – 4 (PL to PH) on the dayside, and about a factor of 2 on the nightside.

The seasonal change in the escape flux is minimal (a factor of ~1.2), but the influence of the planet's axial tilt of about 25° results in a shift of the subsolar point (coinciding with the location of the maximum flux) toward the summer pole. As shown in figure 6.11b (AL, EL, and PL), there is a slight regional variation of the magnitude of the escaping atoms over the seasons. Since the exosphere tends to homogenize the density due to the averaging over a wider area similar to the case of hot O [*Valeille et al.*, 2009b], the spatial gradient of the flux is much milder further away from the lower exosphere.

(a)

(b)
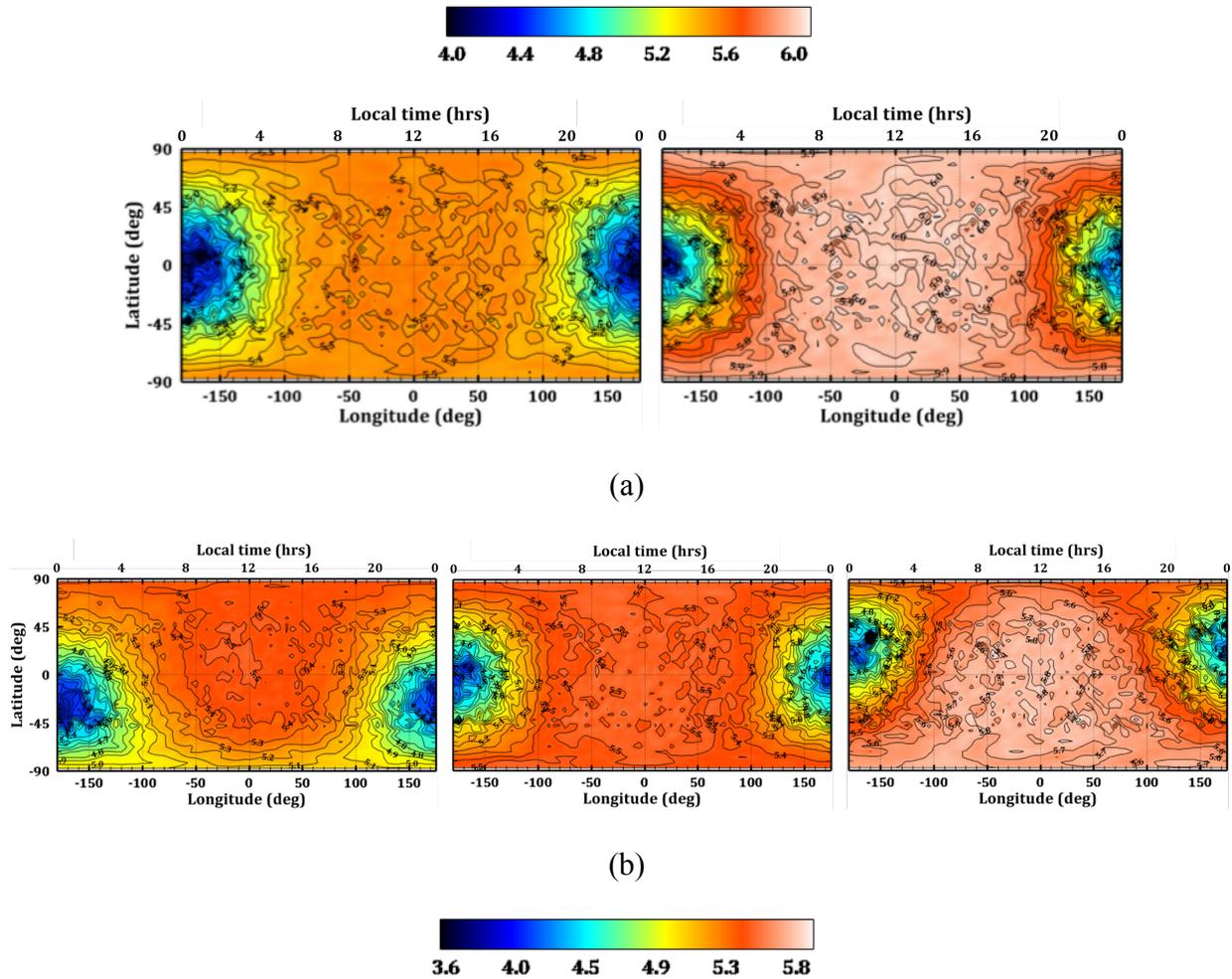
Figure 6.11. Escape flux of hot C at about 1 Mars radius above the surface (at an altitude of ~3400 km) resulting from photodissociation of CO for (a) the EL and EH cases and for (b) the AL, EL, and PL cases. The contours and color scale show the log of escape flux (cm^{-2} s^{-1}).

Escape fluxes by dissociative recombination of CO^+ for the EL and EH cases are illustrated in figure 6.12a. The maximum escape flux regions on the dayside occur a little more toward the morning terminator, due to the fact that there are more hot carbon atoms escaping near this region with the relatively low thermalization rate. The escape flux is enhanced by a factor of about $8 - 10$ from the EL to EH case on the dayside and 8 on the nightside. The seasonal variation in the escape fluxes is about a factor of 1.2 moderating the solar cycle

influence on the hot carbon density. The major influence from the seasonal change is on the spatial distribution of the low and high flux regions, as shown in figure 6.12b.


(a)

(b)
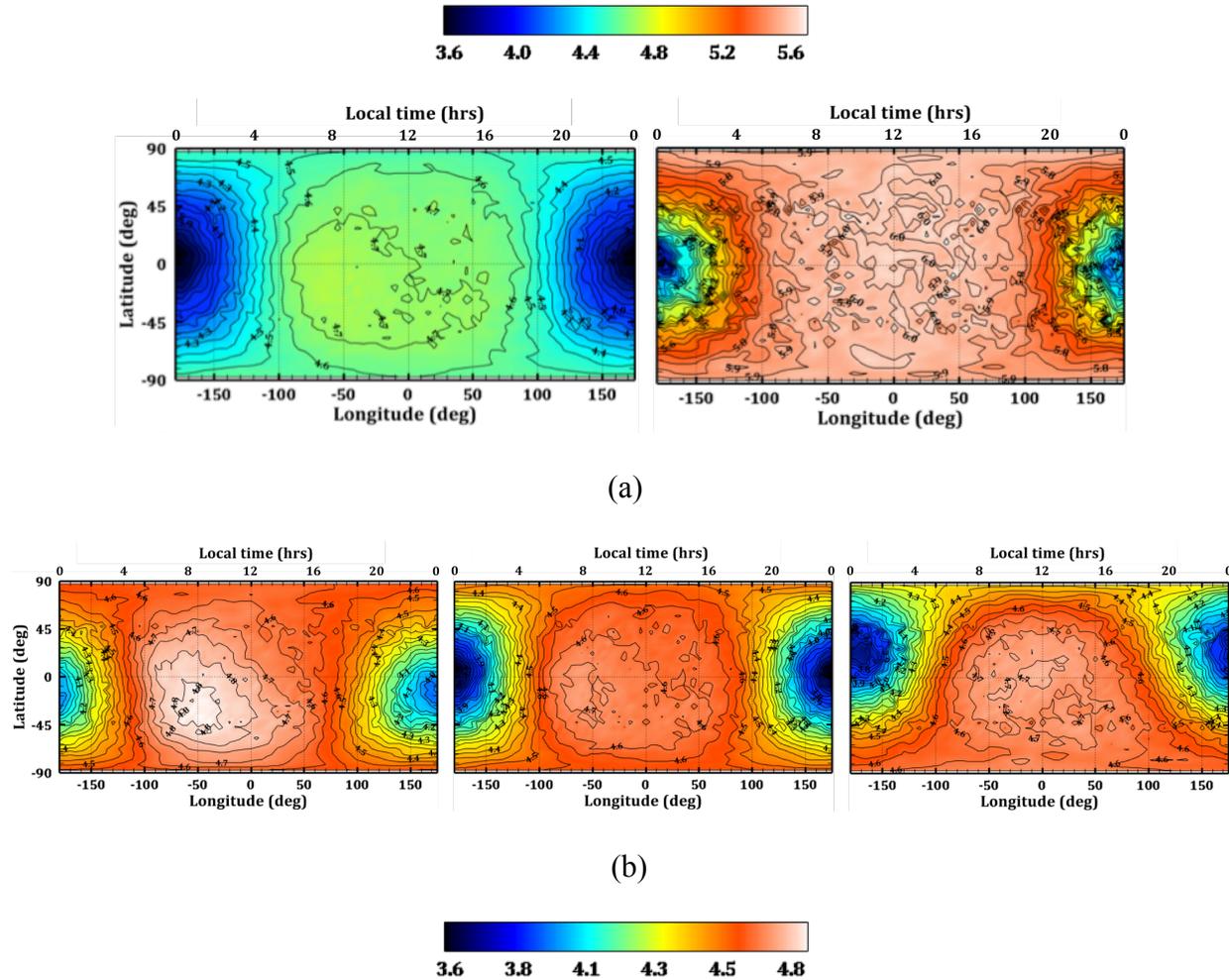
Figure 6.12. Escape flux of hot C at about 1 Mars radius above the surface (at an altitude of ~3400 km) resulting from dissociative recombination of CO^+ for (a) the EL and EH cases and for (b) the AL, EL, and PL cases. The contours and color scale show the log of escape flux (cm^{-2} s^{-1}).

VI.3.3. Altitude variations of hot carbon

The profiles of hot carbon density produced by photodissociation of CO and dissociative recombination of CO^+ are extracted from the three-dimensional global Martian

thermosphere/ionosphere and exosphere simulation at a solar zenith angle of 60° in the

equatorial east plane, which is assumed to be a representation of the dayside average.
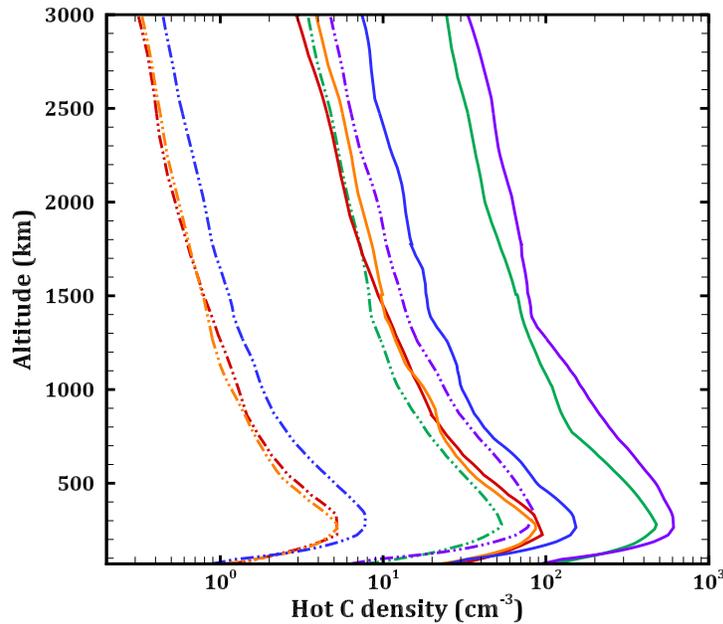
Figure 6.13. Density profiles of hot C at SZA60 eastward at equator for photodissociation of CO (solid lines) and dissociative recombination of CO^+ (dash-dot-dot lines) for AL (red), EL (orange), PL (blue), EH (green), and PH (purple).

Figure 6.13 presents the hot carbon densities as a function of altitude for the AL, EL, PL,

EH, and PH cases from photodissociation of CO and dissociative recombination of CO^+. The

relative distances between the profiles display the seasonal (orbital eccentricity) and solar cycle

(solar flux) influences. The simulated hot carbon is dominantly produced by photodissociation of

CO, which is shown as solid curves. The hot carbon densities at low solar activity are

represented by the AL (red), EL (orange), and PL (blue) cases, and at high solar activity by the

EH (green) and PH (purple) cases. The density peaks for both source mechanisms are situated at

about 250 – 300 km, where a large fraction of hot carbon can escape to space or return to the

125

corona. The ratio of the peak densities of the solar high to low cases for photodissociation of CO is about $4 - 5.5$ and $10 - 11$ for dissociative recombination of CO^+. The larger response of dissociative recombination of CO^+ to the solar flux variation is mainly due to the increase of CO^+ production as mentioned previously (*i.e.*, larger CO mixing ratio). Furthermore, the increase in solar flux is attributed to the larger CO^+ scale height and electron density, which increase the dissociative recombination rate.

The seasonal influence is illustrated for the AL, EL, and PL cases (or the EH and PH). The ratios of aphelion and perihelion cases to equinox range from 1.1 to 1.8. The differences between the three seasons are more apparent in the higher altitudes above the lower exosphere (or in the collisionless regime). The density profiles in the lower altitudes between the AL and EL cases are less distinctive and more or less identical. Again, these profiles, however, only represent one particular location on the dayside, and this structure of the lower altitude profiles can be different depending on the local thermospheric/ionospheric conditions. As discussed in the previous section, the study of the seasonal variation needs two- or three-dimensional aspects, since the seasonal variation impacts the spatial distribution of most of the thermospheric parameters rather than their magnitudes [*Valeille et al.*, 2009a, 2009b]. The seasonal influence is more observable when the dynamics and inherent asymmetries in the atmosphere are incorporated.

VI.3.4. Loss rates and comparisons

Several previous models have investigated the hot C component of the Martian corona resulting from various nonthermal source mechanisms [*Cipriani et al.*, 2007; *Fox and Bakalian*, 2001; *Fox*, 2004; *Fox and Haᶜ*, 1999; *Nagy et al.*, 2001]. The direct comparison with the model

and the previous models is difficult, since models differ by many aspects, such as the description of their thermosphere and ionosphere, numerical scheme, or types of source mechanisms. Here, the global escape flux from the previous EL model is listed, and the possible discrepancies are discussed to better understand all aspects of the Martian hot C corona.

Table 6.1 lists previous models, their results, and the descriptions of their atmospheric inputs. For comparison purposes, the solar high and low cases only (for equinox) are listed, and the global escape fluxes at 400 km are calculated. *Fox and Hać* [1999] carried out Monte Carlo calculations to compute the velocity distributions of hot carbon atoms and their global escape fluxes from dissociative recombination of CO^+. The computed global escape flux for dissociative recombination of CO^+ is about 5.6×10^4 cm^{-2} s^{-1} and 5.0×10^5 cm^{-2} s^{-1} for solar low and high conditions, respectively. The escape flux for solar low case is larger by about a factor of 3 than that (eroded case) of *Fox and Hać* [1999], but their solar high case flux is similar to this study's value (a factor of about 1.1 lower in the solar high case). *Fox and Bakalian* [2001] have estimated the global average escape fluxes of six source mechanisms using the exobase approximation, which are 2.1 and 26×10^5 cm^{-2} s^{-1} for low and high solar activity conditions, respectively. In their study, *Fox and Bakalian* [2001] compared their model with the model from *Nagy et al.* [2001]. They also concluded that dissociative recombination of CO^+ has the largest dependency on solar activity. Their separate calculation of the escape flux for photodissociation of CO at low solar activity is about 1.7 lower than this study's value, 2.8×10^5 cm^{-2} s^{-1}, but, again, the solar high case value is close to this study's escape flux (about a factor of 1.1 larger than ours, 1.62×10^6 cm^{-2} s^{-1}). It is logical to expect the similarity in escape flux at the high solar activity since *Fox and Hać* [1999], *Fox and Bakalian* [2001], and *Fox* [2004] used the MTGCM (one column of the upper atmosphere at a particular location) supplied by Bougher.

127

Models	Low solar activity	High solar activity	Thermosphere/Ionosphere model	Numerical scheme
Photodissociation of CO				
Nagy et al. [2001][e]	0.27[e]	3.9[e]	1D	Two-stream method
Fox and Bakalian [2001]	0.165	1.8	1D	Exobase approximation
Fox [2004]	0.73	3.5	1D	Exobase approximation
This study[a]	0.28	1.62	3D	DSMC
Dissociative recombination of CO$^+$				
Fox and Hać [1999][b]	0.019	0.58	1D	Monte Carlo
Nagy et al. [2001][e]	0.27[e]	3.9[e]	1D	Two-stream method
Fox and Bakalian [2001]	0.029	0.62	1D	Exobase approximation
Fox [2004]	0.128	0.77	1D	Exobase approximation
Cipriani et al. [2007][b]	0.00025	0.023	1D[d]	Monte Carlo test particle
This study	0.056	0.50	3D	DSMC

Table 6.1. Comparison of escape fluxes between current model for this study and previous models.

[a]Fluxes are in 10^6 cm^{-2} s^{-1}.
[b]Global escape rates are converted to global averaged escape fluxes at the altitude of 400 km.
[c]Eroded case.
[d]Kim atmosphere ([*Kim et al.*, 1998]).
[e]*Nagy et al.* [2001] included photodissociation of CO, dissociative recombination of CO$^+$, and collisions with hot O in their computation. They provided the combined global averaged escape rate and flux for all photochemical mechanisms.

Nagy et al. [2001] used a two-stream calculation adopting the ionosphere description from *Fox and Hać* [1999] and *Kim et al.* [1998]. The differences between those two models are inherent in the slightly different descriptions of the background atmosphere and the local

parameters (*e.g.*, collisional cross section), where the main discrepancy comes from the different numerical schemes. *Fox* [2004] included dissociative recombination of CO_2^+ together with other minor mechanisms to study the sources of ambient and escaping C atoms. They predicted that the most important source mechanism is photodissociation of CO, followed by electron impact dissociation of CO as the second most important mechanisms rather than dissociative recombination of CO^+. The escape fluxes from *Fox and Bakalian* [2001] and *Fox* [2004] are comparable to each other and to that from *Nagy et al.* [2001] at low solar activity only. *Cipriani et al.* [2007] used a 1D-spherical Monte Carlo test particle approach to investigate the production of hot molecules (CO_2 and CO) in addition to hot O and C atoms. Their estimated escape rates of C from dissociative recombination of CO^+ for both low and high solar activity are more than an order of magnitude lower than other model results, including the current study results. *Cipriani et al.* [2007] have adopted the universal potential (UP) in their molecular dynamic scheme to describe collisions with ambient atmosphere, and stated several drawbacks that affect the energy level relevant to the dissociative recombination process.
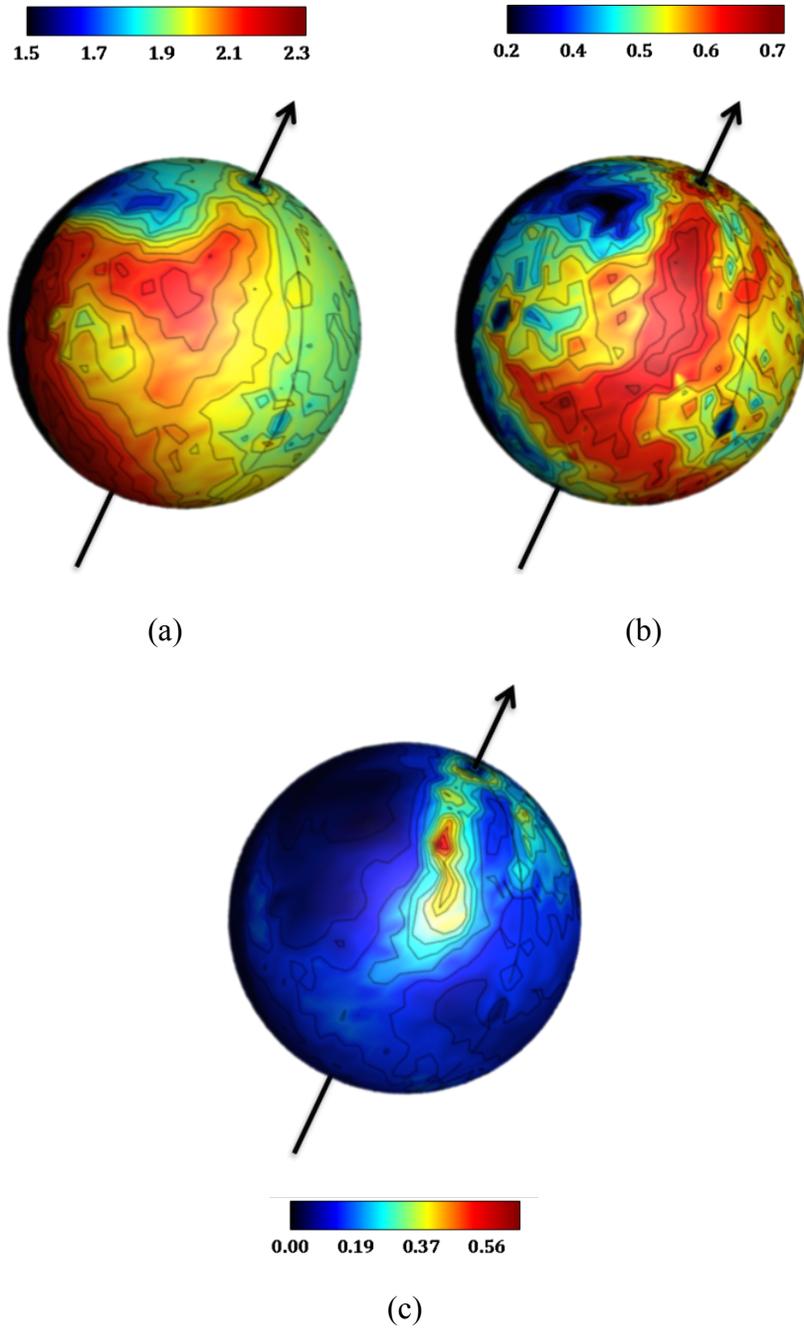
Figure 6.14. Longitude-latitude variation of (a) hot C density (in unit of log (cm^{-3})) with $V_{threshold}$ = local thermal speed, (b) hot C density with $V_{threshold}$ = escape speed, and (c) collisional frequency (in unit of s^{-1}) between hot C and background species from photodissociation of CO for the AL case at altitude of 200km. The planet is rotated to show the region around LT = 0900. The Sun is located on the right.

Previous models differ from each other by ranges of different factors, including different numerical schemes, and descriptions of background atmosphere and interaction between the nascent and ambient species. According to table 6.1, the previous models have employed one-dimensional thermosphere/ionosphere atmosphere describing the background atmosphere spherically symmetric on the dayside. The simulations with a one-dimensional background atmosphere essentially neglect the three-dimensional effects, which account for spatial variation of densities and fluxes due to non-axisymmetry of the thermospheric/ionospheric structure, tangential velocity of particles, zonal/meridional winds, and planetary rotation. The global escape fluxes from each source mechanism for low/high solar activity from this study are higher / lower than those calculated by *Fox and Hać* [1999], *Nagy et al.* [2001], and *Fox and Bakalian* [2001], whereas the results from *Fox* [2004] and *Cipriani et al.* [2007] are the upper and lower limits to the current estimation of the global carbon escape, respectively. The three-dimensional thermosphere/ionosphere accounts for the spatial variation of collisional frequency between a nascent hot carbon and a background cold atmospheric species, which depends on the spatial distribution of background atmosphere densities (explained in detail in section 4) and tangential velocity of hot species.

Figure 6.14 shows one example of the effects of the three-dimensional background atmosphere on the hot corona. The local maxima for hot carbon with its velocity exceeding twice the local thermal speed are located in different regions from those for the hot carbon with its velocity exceeding the local escape speed. Local hot carbon density is maximized along the morning terminator (figure 6.14a), where hot carbon is most likely to attain relatively lower velocity compared to that of hot carbon produced in other regions. The regions where modeled hot carbon atoms exhibit relatively higher velocity (*i.e.,* exceeding the escape speed) coincide

with higher collisional frequency and maximum hot carbon regions (figure 6.14b – collisional frequency; 6.14a and 6.14c – hot carbon density with different $V_{threshold}$). The regions with large thermalization are predicted to be situated where the local hot carbon is relatively slower and the collisional frequency is locally maximized. Since this spatial variation is inherently absent in one-dimensional descriptions of the thermosphere/ionosphere, the previous models could have underestimated/overestimated the escape flux for low/high solar activity.

$10^{23}s^{-1}$	Aphelion (A)		Equinox (E)		Perihelion (P)	
Solar activity	Low (L)	High (H)	Low (L)	High (H)	Low (L)	High (H)
Photodissociation of CO (PD)	4.02	-	4.94	29.4	8.42	46.6
Dissociative recombination of CO^+ (DR)	1.18	-	0.96	9.06	1.06	10.5
Sputtering[a]	-	-	1.5	-	-	-
Ion escape[b]	-	-	$\leq$30	$\leq$232	-	-

Table 6.2. Escape rates of hot carbon for different source mechanisms for different seasons and solar cycle.

[a]Originally calculated by *Luhmann et al.* [1992] and corrected by *Jakosky et al.* [1994].
[b]Upper limits to the C-containing ion escape estimated by *Fox* [1997b].

Here, the global escape rates for different solar conditions and seasons are estimated. Table 6.2 shows the escape rates computed here separately for the two source mechanisms and compared with those from sputtering and ion escape. The estimated escape rates for the two extreme cases at the AL and PH cases range from 4.02×10^{23} s^{-1} to 46.6×10^{23} s^{-1} for photodissociation of CO, and from 1.18×10^{23} s^{-1} to 10.5×10^{23} s^{-1} for dissociative recombination

of CO^+. The solar cycle variation is a factor of about 5.5 and 9.5 for the former and latter reactions, respectively, showing the higher sensitiveness of dissociative recombination of CO^+ to the increase in the solar flux. The variation by season is small for the dissociative recombination case, but it is about $1.3 - 1.6$ for photodissociation case, which is similar to the rough estimated ratios of the heliocentric distances, $(1.5/1.38)^2 \sim 1.18$ and $(1.67/1.5)^2 \sim 1.24$. The estimated escape rate from dissociative recombination of CO^+ for the AL case is somewhat similar to that for the EL case (instead of being larger as in the case of photodissociation of CO). As shown in figure 6.9, the maxima in the hot carbon density are located in the high latitudes on the morning terminator, where the collisions with the background thermal species are relatively low. This region is also enhanced with relatively faster hot carbon, which contributes to the total escape rate that is comparable to that of the EL case. Overall, the estimated total escape rate ranges $\sim (5.2 - 57.1) \times 10^{23}$ s^{-1} for the aphelion solar low to perihelion solar high case.

The global sputtering loss rate of CO_2 computed by *Luhmann et al.* [1992] for low solar activity is about 1.5×10^{23} s^{-1} (a factor of ~2 numerical error was corrected by *Jakosky et al.* [1994]). This C sputtering loss rate (as C, CO, or CO_2) is of the same order of magnitude as the estimated total escape rate from all dominant photochemical source mechanisms for the EL case. If we scale the age of the sun backward in time and assume that the sun had been more active, in terms of the ionizing radiation and coronal activity, the solar-induced-loss of the primordial Martian atmosphere would be magnified [*Ayres*, 1997]. Previous modeling studies for the earlier history of the Martian atmosphere [*e.g., Luhmann et al.*, 1992; *Zhang et al.*, 1993] have suggested that nonthermal escape of C due to photochemistry and exospheric erosion of hot carbon corona by the solar wind may have played significant roles in CO_2 loss in the content of the early Martian atmosphere. The escape rate of C induced by photodissociation of CO and

dissociative recombination of CO^+ is assumed to have been enhanced in the past due to the larger photoionization rate of about 5 times contemporary value (*i.e.*, larger electron and CO^+ densities) [*Ayres*, 1997] and the increase of the fraction of CO in the thermosphere [*Fox and Hać*, 1999]. The sputtering of C is expected to have been more efficient and likely to be orders of magnitudes larger in the earlier Martian history than at present.

Chapter VII

Two atmospheric models – MTGCM and M-GITM

MTGCM [*Bougher et al.*, 1999, 2000, 2002, 2004, 2006, 2009] results have been employed into the kinetic particle model to model the variation of the hot O and C coronae for different solar cycle and seasons. Recently, a newly improved atmospheric model, M-GITM [*Bougher et al.,* 2014], has also been used as inputs. The detailed description of the difference in physics of the MTGCM and M-GITM was given in chapter 3. This chapter presents a comparison to highlight the major differences in advance of the following hot O study in chapter 8, which uses the new M-GITM.

VII.1. MTGCM vs. M-GITM

	MTGCM	M-GITM
Domain range	135 km – 200 km Coupled with MGCM at the 1.32 μbar level	0 km – 300 km (as inputs to Mars-AMPS, ~100 km – 300 km)
Horizontal and vertical resolution	5°×5° horizontal grid Log-pressure vertical coordinate grid with 0.5 scale height spacing	5°×5° horizontal grid Capable of using stretched vertical coordinate grid 2.5 km vertical resolution (currently in use; ~0.25 scale height spacing)
Assumption	Hydrostatic	Non-hydrostatic
Model species	Major and minor neutrals Photochemical ion species	Major and minor neutrals Photochemical ion species

		Basic set of primitive equations • Solve the NS equations in the radial direction separately from the horizontal directions • Relax the assumption of hydrostatic equilibrium (neutrals have own continuity and momentum equation in vertical direction, self-consistently • Calculate sources and losses explicitly
Governing equations	Basic set of primitive equations • Hydrostatic equilibrium	
Chemistry	Same	Same
Topography	On	Off (In process of testing MGS/MOLA inputs)

Table 7.1. Comparison of the MTGCM and M-GITM.

The studies conducted in this thesis apply the simulated thermosphere and ionosphere from two numerical models, the Mars Thermosphere General Circulation Model (MTGCM) and Mars Global Ionosphere Thermosphere Model (M-GITM). The detailed model descriptions for these models are provided in chapter III. The major improvement in M-GITM in comparison with the MTGCM is the treatment of the entire Martian atmosphere as an integrated system from the surface to the base of the exosphere. The atmosphere is assumed as non-hydrostatic in M-GITM, which allows the atmospheric constituents to have their own vertical continuity and momentum equations. This explicit calculation of momentum in the vertical direction for each species enables the model to describe the specific localized features. The main improvements in M-GITM compared to the MTGCM are addressed in table 7.1.

Numerical modeling efforts of the Martian atmosphere has been significantly improved in order to understand the fundamental atmospheric processes that drive the time dependent dynamics and structural variation on the atmosphere of Mars. Since Mars has a strongly coupled atmospheric system, the detailed characterization of the thermosphere and ionosphere is crucial

for modeling the hot atomic corona in the upper atmosphere on Mars. The mechanisms that form the structure of the hot atomic corona develop deep within the thermosphere and ionosphere, which have to be well-addressed in order to investigate the hot corona accurately. Following sections will present features in the thermosphere and ionosphere modeled by the MTGCM and M-GITM at several different solar and seasonal conditions, which are important for the hot atomic corona simulation.

VII.2. Low solar activity at equinox

In this section, the Martian hot coronae are simulated with a fixed Martian season and solar condition parameters: equinox (L_s = 180°) and low solar activity (F10.7 = 70 at Earth) for the purpose of studying the difference in structure and features only between MTGCM and M-GITM. This particular condition of Mars corresponds to the equinox and low solar activity (EL) case from MTGCM and the autumnal equinox low solar activity case (AEQUMIN) from M-GITM.

VII.2.1. Temperature and global wind variation

The longitudinal and latitudinal distribution of the background neutral temperatures from MTGCM and M-GITM are shown in figure 7.1. The neutral temperature from MTGCM displays high temperature regions at high latitudes near the polar regions and warmer temperature regions near the evening terminator. The peak temperature is visible near North and South Pole in the morning, which is ~ 275 K, as a result of the subsiding and converging atmospheric flow. The lowest temperature appears on the nightside at LT = ~2200 − 0200 from the equator to middle latitudes (~120K). Diurnal variations are large, which are about 90 K.

These high and low temperature regions are consistent with the global atmospheric flow. Zonal winds blow from the subsolar region towards the evening and morning terminator with speeds of ~100 m/s and -350 m/s, respectively. The morning terminator regions near the equator show relatively low temperatures, in accordance with the atmospheric flow upwelling and diverging. These regions are characterized by the meridional winds (~50 m/s and -50 m/s) approaching the North and South Poles, and ascending vertical winds as shown in figure 7.1. Converging strong meridional winds towards both polar regions with descending vertical winds are consistent with those peak temperatures.

Analogously, the neutral temperature simulated by M-GITM (figure 7.1b) peaks on the equator and at low latitudes near the evening terminator with temperature of ~240 K. Warmer temperature regions are shown in the afternoon from the equator to mid-latitudes. Both South and North polar region temperatures are about 190 K. The temperature reaches the lowest on the nightside, ~120 K, between LT = 0000 and 0600. As in the neutral temperature from MTGCM, diurnal variation is larger by ~120K.

The global wind variations are quite similar to ones from MTGCM. Descending vertical winds near the evening terminator on the equator converge with eastward zonal winds with speeds of about 100 m/s. Meridional winds blow towards both polar regions from the equator, across the poles, and converge on the nightside. Strong zonal winds of about 250 m/s and -250 m/s blowing towards North and South Poles, respectively.

The main difference in the spatial distribution of temperatures from the MTGCM and M-GITM is the polar warming. These warm temperatures in the polar regions in the MTGCM temperature distribution are resulted from propagating nonmigrating tides, which are currently missing in M-GITM. The polar warming is likely to appear if these nonmigrating tides are

included with inclusion of topography [*Bougher et al.,* 2014b]. Due to this difference in the neutral temperature distribution, the local $V_{threshold}$ from the MTGCM and M-GITM for hot particles produces a difference in their horizontal variations, since $V_{threshold}$ is twice the local thermal speed. Consequently, the effect of different temperature distribution is evident in the horizontal distribution of the resulting hot corona.


Tn

Un

Vn

Wn

(a)   (b)
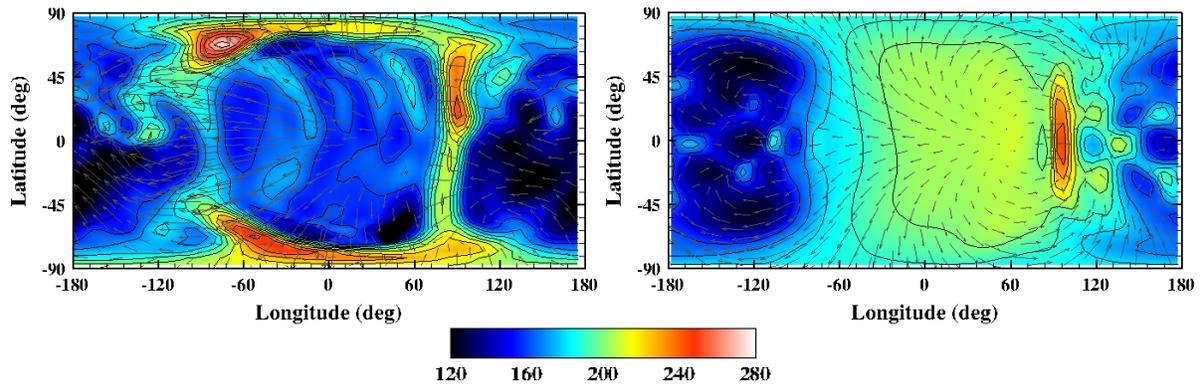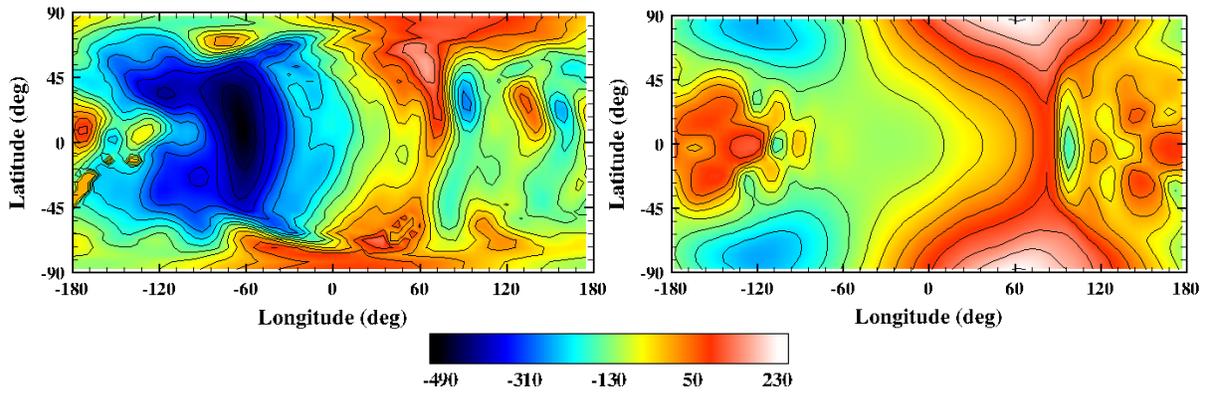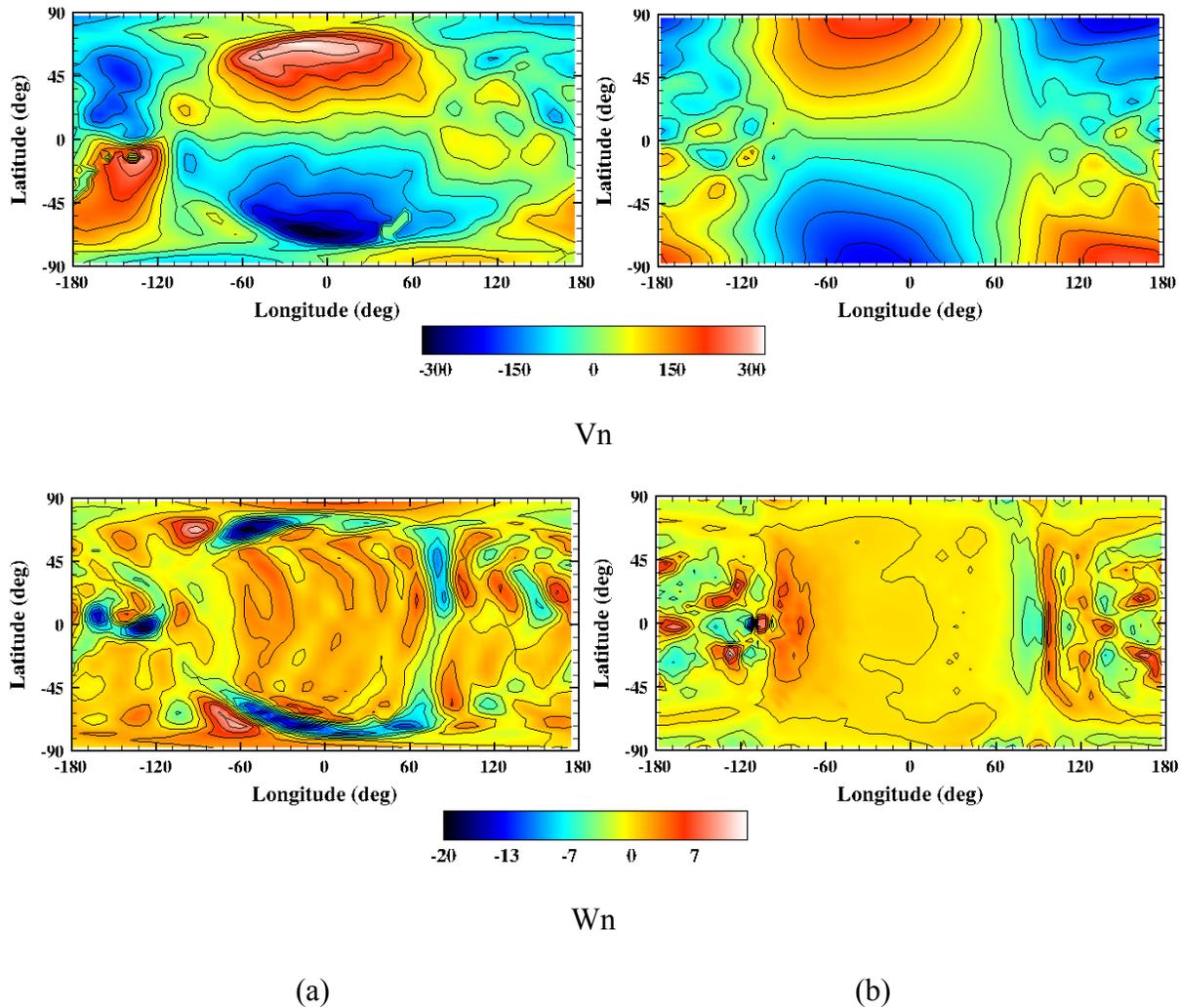
Figure 7.1. The horizontal variations of the neutral temperatures (K) and zonal (Un; m/s), meridional winds (Vn; m/s), and vertical winds (Wn; m/s) from (a) MTGCM and (b) M-GITM at an altitude of about 200 km.

VII.2.2. Thermosphere (O, CO$_2$, CO) / MTGCM /M-GITM comparison - Structure and features

Illustrations of thermospheric species (O, CO$_2$, and CO) are shown in figure 7.2. As described in the earlier section on hot carbon investigation, the global O distribution is remarkably different from the CO$_2$ distribution. Displaying peak density on the nightside, atomic O densities are distributed in a pattern that is roughly anticorrelated to that of neutral

temperature. The peak of O density is located near the equator and at low latitudes (LT = 0000 – 0400). Most of high-density regions appear in the regions of cold background temperature. Density variation from day to night is a factor of about 10. Contrarily, the distribution of the CO_2 density closely resembles the one of neutral temperature, as shown in figure 7.1. The locations of peak and high densities are consistent with high neutral temperature regions. The diurnal variation of CO_2 density is a factor of ~15. Similar to the CO_2 density distribution, CO densities are spatially distributed in a pattern that is correlated to those of neutral temperature and CO_2 density.

Figure 7.2b shows the same set of thermospheric species distributions from M-GITM. The O distribution from M-GITM shows large bulges of densities on the nightside compared to those simulated by MTGCM at LT = 0200 – 0400. O is produced on the dayside from CO_2 photolysis and ion-neutral chemical reactions and is transported by atmospheric flow to the nightside, forming density bulges at low and mid latitudes [*Bougher et al.,* 2014a]. The CO_2 and CO spatial distributions are analogous to those in the MTGCM case. Figure 7.2 shows the anticorrelation of CO_2 density distribution compared to that of O density. Unlike the MTGCM case, high CO_2 densities are populated at low and mid latitude regions, and the peak density is situated where the neutral temperature maximizes. CO densities at this altitude show slightly larger density in general (*c.f.,* CO_2 and CO density distributions in the MTGCM case). As in the case of the CO density simulated by MTGCM, some high densities are shown on the nightside, resembling the bulges in the O distribution. These noticeable differences shown in the spatial distributions from the MTGCM and the current M-GITM codes will be alleviated after adding topography into M-GITM [*Bougher et al.,* 2014b].

O

CO₂

CO

(a)   (b)
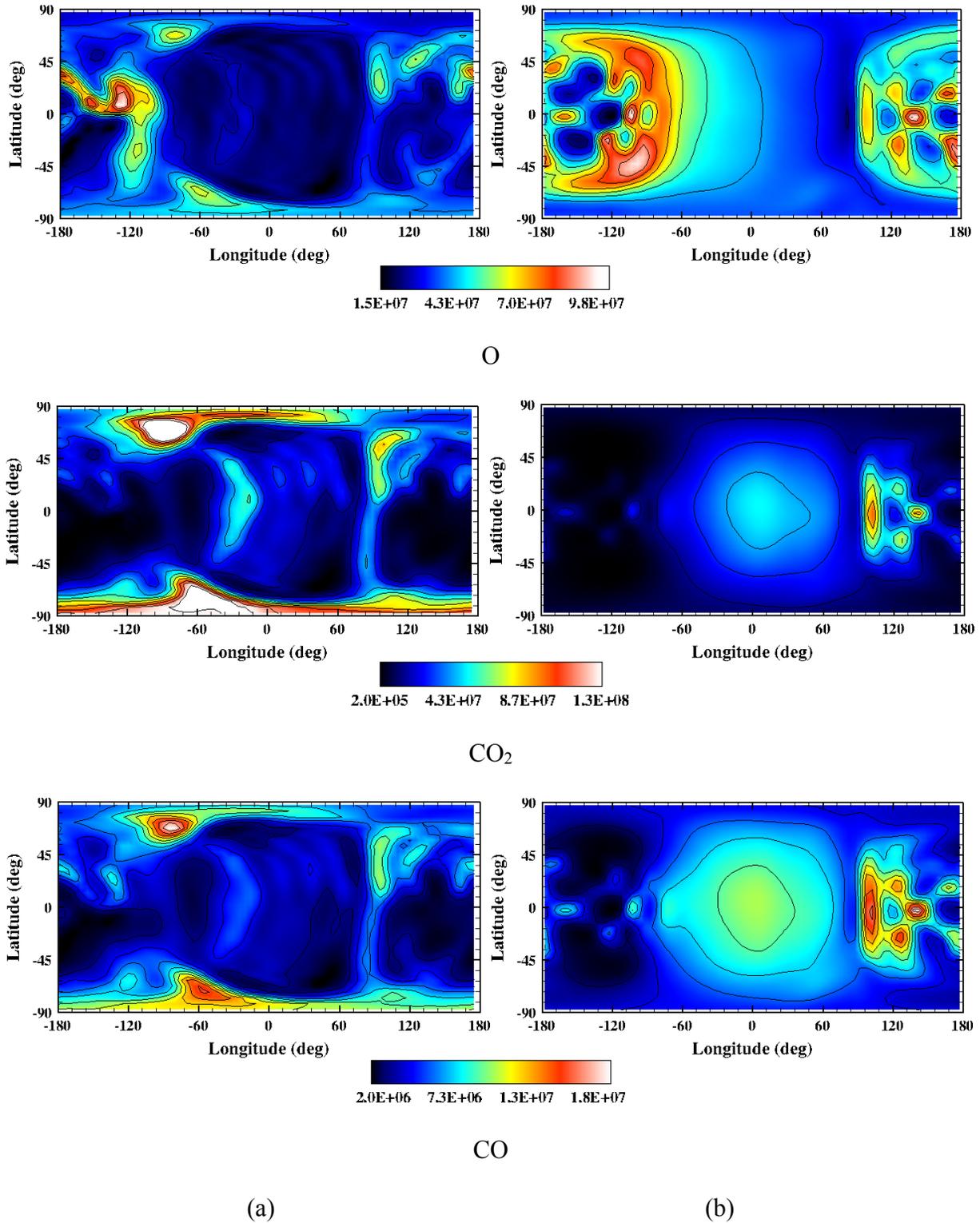
Figure 7.2. Spatial variation of neutrals (O, top; CO$_2$, middle; CO, bottom) from (a) MTGCM and (b) M-GITM at near 200 km altitude. The color contour represents the density in the unit of cm^{-3}.

VII.2.3. Ionosphere (O$_2^+$) / MTGCM /M-GITM comparison - Structure and features

$$O_2^+$$
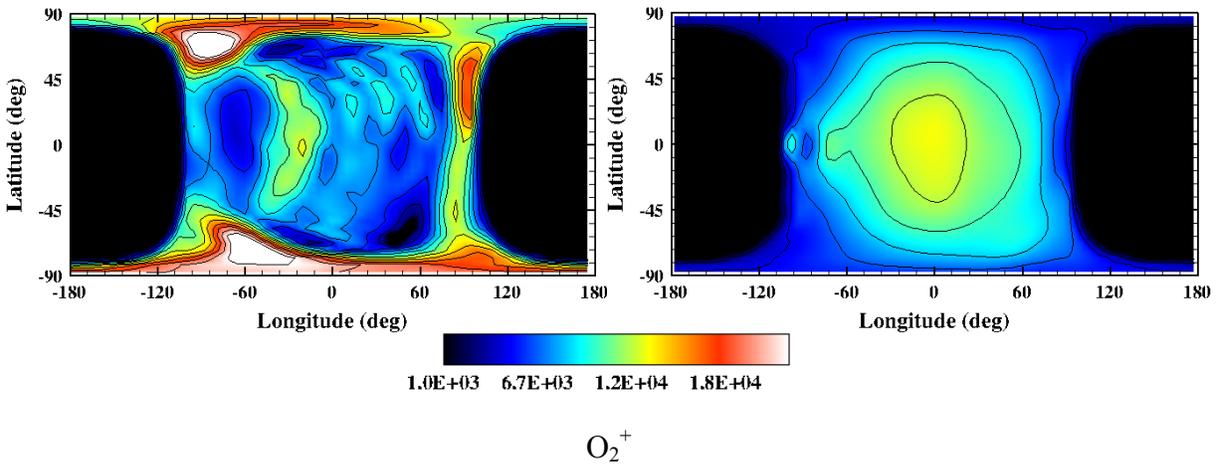
**Figure 7.3.** O$_2^+$ density at ~200 km for equinox and low solar activity.

The major ionospheric species O$_2^+$ is shown in figure 7.3 modeled by the MTGCM and M-GITM. The major difference between O$_2^+$ simulated by two models comes from the structure of the spatial distribution of density. The MTGCM O$_2^+$ density exhibits more fluctuation of density over the dayside, and the locations of extrema are consistent with the local temperature. As mentioned in the previous section, these detailed features will be also shown in M-GITM after inclusion of topography [*Bougher et al.,* 2014b]. In spite of the distinct difference in the distribution of density, the average O$_2^+$ density in the subsolar region in both models are similar, which is ~10^4 cm^{-3}. Furthermore, M-GITM is in process of adding ion transport in the upper atmosphere, which will allow further modification of the ionosphere by diffusing O$^+$ ions (see *Bougher et al.* [2014b]).

**VII.3. Solar cycle and seasonal variation**

Various Martian seasons (based on the seasons on the northern hemisphere) and solar condition cases can be run in the MTGCM and M-GITM, utilizing the appropriate model parameters (figure 7.4). Particularly, the solar cycle and seasonal cases considered in the model simulations using MTGCM are for L_s = 90° (aphelion), 180° (autumnal equinox), and 270° (perihelion) for low solar activity (F10.7 = 70) and high solar activity (F10.7 = 200) conditions. The five cases are considered from the combination of the parameters above: aphelion and low solar activity (AL), equinox and low solar activity (EL), perihelion and low solar activity (PL), equinox and high solar activity (EH), and perihelion and high solar activity (PH). This set of five cases is an excellent suite for investigating the seasonal and solar cycle variation of the Martian atmosphere.

In addition to the five MTGCM cases, M-GITM's typical simulations focus upon a few with more variety. M-GITM considers cases for L_s = 0° (vernal equinox), 90° (aphelion), 180° (autumnal equinox), and 270° (perihelion) for low solar activity (F10.7 = 70), moderate solar activity (F10.7 = 130), and high solar activity (F10.7 = 200) conditions. Thus, a total 12 cases from M-GITM are incorporated into the kinetic particle model, Mars-AMPS, for the hot coronae simulations. An abbreviation for each of the 12 cases will be used hereafter: VEQUMIN, VEQUMED, VEQUMAX, AEQUMIN, AEQUMED, AEQUMAX, APHMIN, APHMED, APHMAX, PERMIN, PERMED, and PERMAX. The prefixes VEQU-, AEQU-, APH-, and PER- correspond to vernal equinox, autumnal equinox, aphelion, and perihelion, respectively, and the suffixes -MIN, -MED, and -MAX correspond to low, moderate, and high solar activity conditions, respectively. In the following sections, solar cycle variability is characterized at a fixed orbital position, autumnal equinox (L_s = 180°), and seasonal variability is represented by

three seasons, aphelion ($L_s = 90°$), equinox ($L_s = 180°$), and perihelion ($L_s = 270°$), with a fixed solar condition (F10.7 = 70; low solar activity).
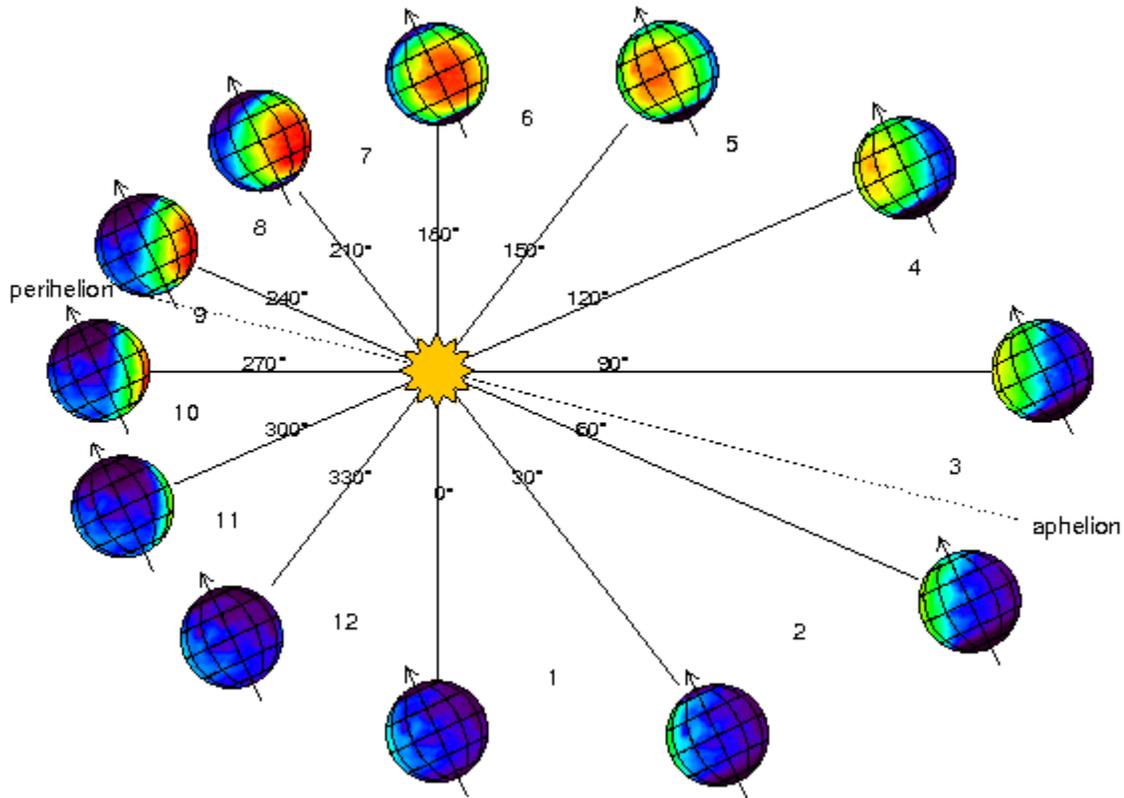
Figure 7.4. Diagram of Martian solar longitude (L_s) and seasons.

VII.3.1. Temperature and global wind variation

Neutral temperature is highly dependent on the variable solar fluxes. As discussed in chapter VI for hot C investigation, the locations of the maxima and minima temperatures are consistent with increasing solar activity. The dayside temperature (near the subsolar region) increases by about 100 K while the nightside temperature varies by about 30 K (figure 7.5a).
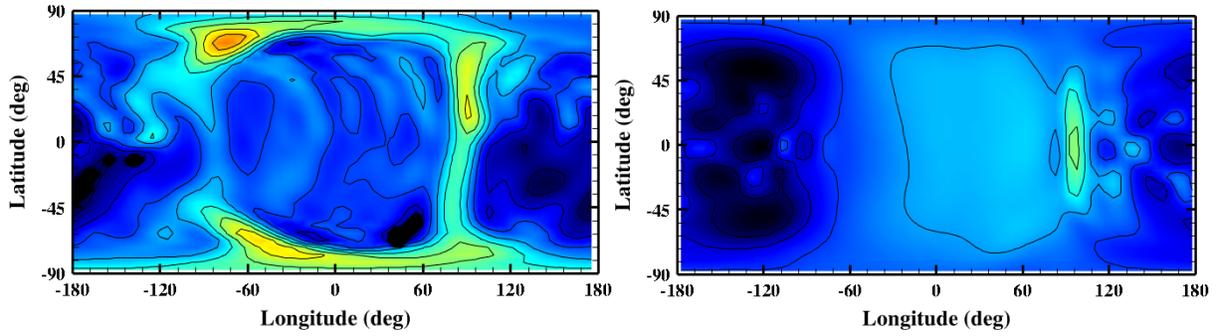
Low solar activity
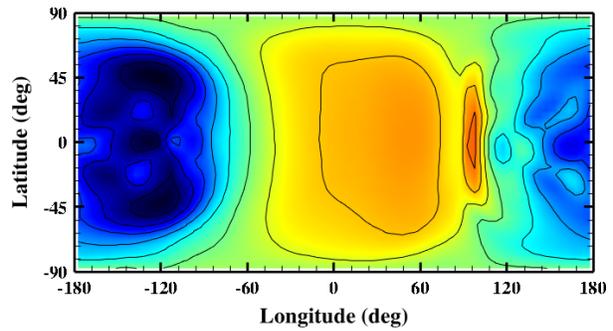
Moderate solar activity
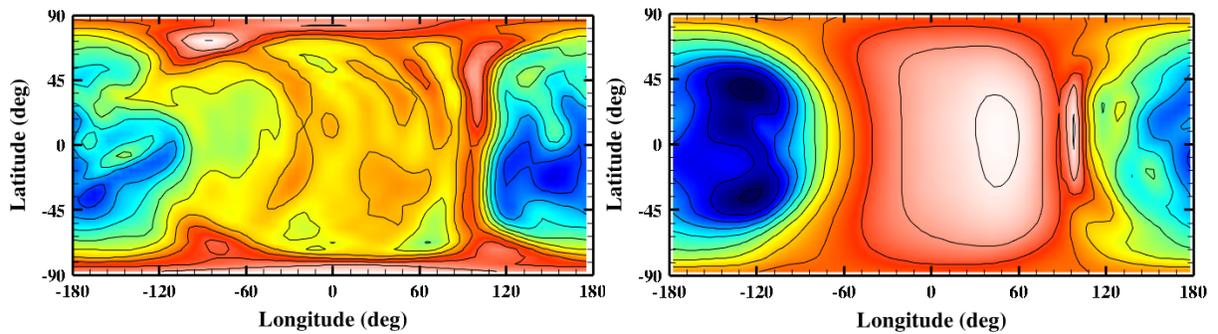
High solar activity
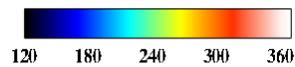
(a)   (b)

Figure 7.5. Solar cycle variation of Tn for (a) low and high solar activities simulated by MTGCM and (b) low, moderate, and high solar activities simulated by M-GITM.

Figure 7.5b displays the solar cycle variability of the neutral temperature simulated by M-GITM at near 200 km for a fixed orbital position (autumnal equinox, L_s = 180°). The spatial patterns of neutral temperature from M-GITM also remain nearly constant over the globe, whereas the magnitudes of neutral temperature increase with increasing solar EUV-UV fluxes. Neutral temperature at the subsolar region varies from ~200 K (low solar activity) to ~350 K (high solar activity), ~280 K for the moderate solar activity case.

The neutral temperatures modeled by the MTGCM and M-GITM show similar variation as solar activity increases. The current M-GITM atmosphere estimates a slightly warmer atmosphere for the high solar activity condition, which is shown as higher dayside temperatures than those from the MTGCM. M-GITM has been in process of investigating the use of topography measurements by the Mars Orbiter Laser Altimeter (MOLA) onboard Mars Global Surveyor (MGS). Implementation of topography will allow the atmosphere simulated by M-GITM to have detailed features in the spatial distribution, similar to that computed in the MTGCM atmospheres.
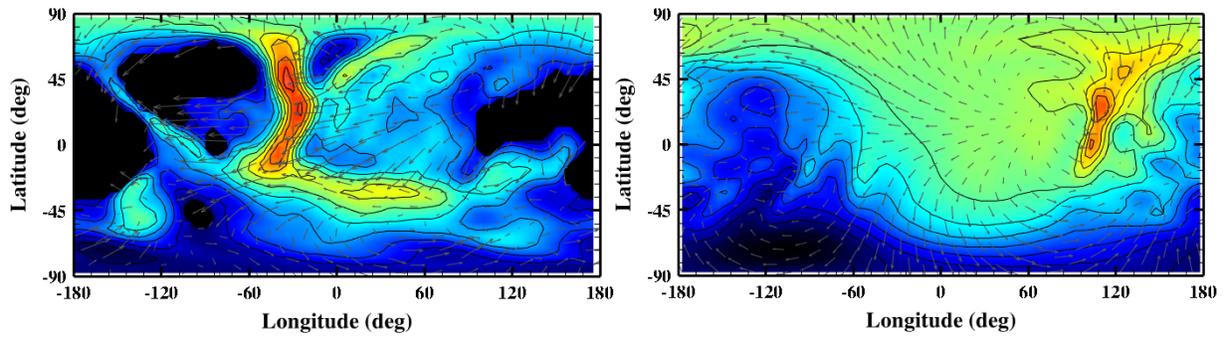
Aphelion ($L_s = 90°$)
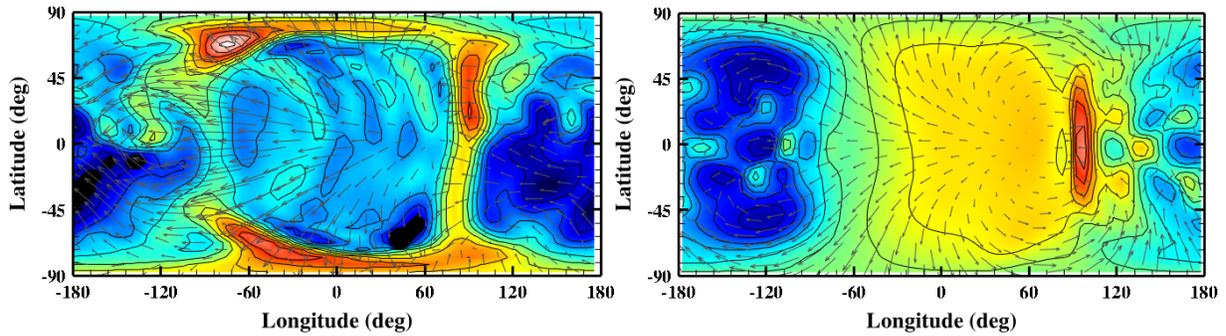
Equinox ($L_s = 180°$)
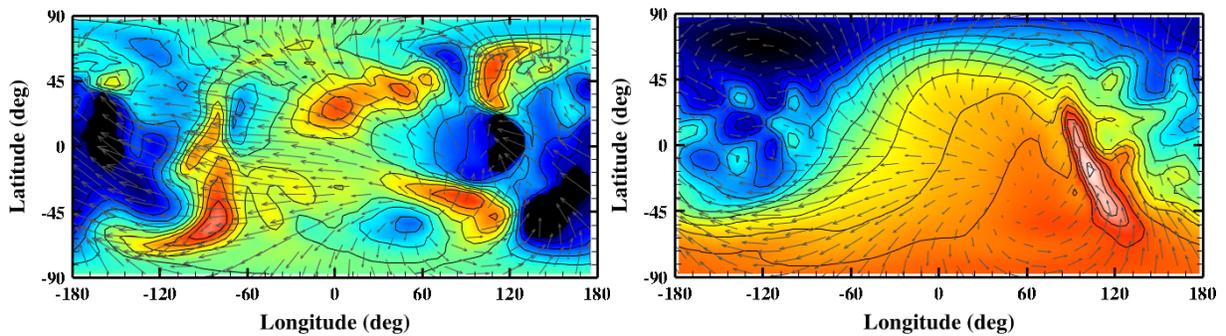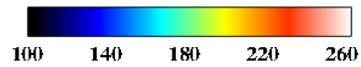
Perihelion ($L_s = 270°$)

(a)   (b)

Figure 7.6. Seasonal variation of Tn for three representative orbital positions. Aphelion, autumnal equinox, and perihelion simulated by (a) MTGCM and (b) M-GITM.

The neutral temperatures from the MTGCM for three different seasons, aphelion (L_s = 90°), equinox (L_s = 180°), and perihelion (L_s = 270°), are shown in figure 7.6a. The spatial locations of minimum and maximum temperatures are on the nightside and the dayside, respectively, for all seasons. However, the high and low temperature regions are distinctly differently situated for each season. The seasonal variability of neutral temperature is rather small compared to the solar cycle variability. The seasonal variation in the atmosphere is affected mostly by the solar IR fluxes rather than EUV-UV fluxes. The seasonal variation is characterized as absorption of these long-wave radiations in the lower atmosphere, which results in the expansion and lifting of ionospheric peaks. While the spatial variation of temperature distribution changes dramatically over seasons, the magnitude of temperature does not change by a large degree.

Compared to the MTGCM temperatures, the M-GITM temperatures (figure 7.6b) show fewer features in the spatial distribution of high and low temperature regions. As mentioned previously, these differences in the spatial features of temperature distribution will likely be removed after inclusion of topography in M-GITM (propagating nonmigrating tides will cool the maximum temperature regions near the subsolar region). The maximum temperature regions for all seasonal cases are located near the evening terminator at low and mid latitudes due to the local convergence of horizontal flow and downwelling of winds. The dayside average temperature does not also vary by a large degree in the M-GITM case, but the spatial distribution of extrema remains consistent for all seasons. This different seasonal variation in temperature affects the horizontal distribution of the resulting hot particle density, since the distribution of $V_{threshold}$ is correlated with the local neutral temperature.

VII.3.2. Thermosphere variation (O, CO$_2$, CO) / MTGCM and M-GITM comparison - Structure and features

The variation of the thermosphere over solar cycle and seasons is presented in this section for two dominant neutral species, O and CO$_2$. These two thermospheric species are important for thermalization of hot atoms and heating of the neutral atmosphere. These two species show distinctive spatial density variations, due to different sources and losses.

O density is characterized by its spatial distribution, which has an inverse correlation with that of neutral temperature (figure 7.7). In both the MTGCM and M-GITM cases, the maximum density is concentrated in the nightside at about UT = 0000 – 0600 near the equator and low latitudes, where neutral temperature becomes the lowest. Most of the dayside regions have low O density that varies by a factor ~3 and ~2 from solar low to high for the MTGCM and M-GITM, respectively. The high-density regions of the M-GITM oxygen are more widely situated than those of the MTGCM oxygen in the directions of both latitude and local time.
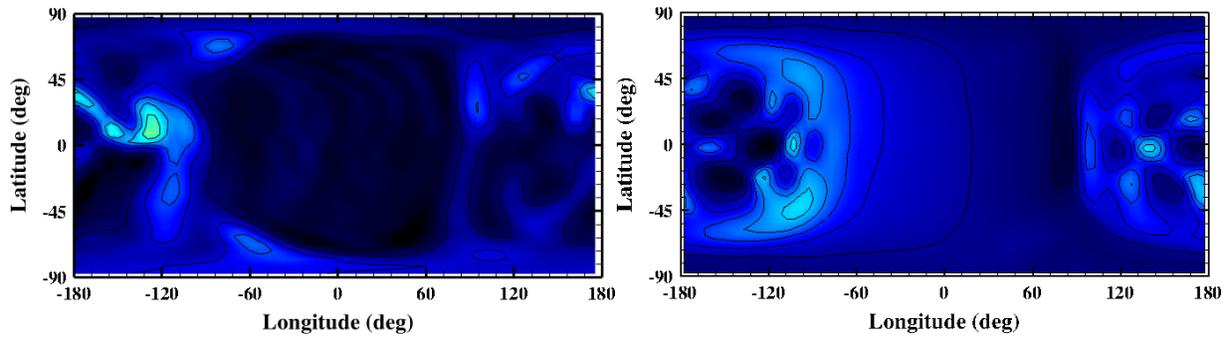
Low solar activity
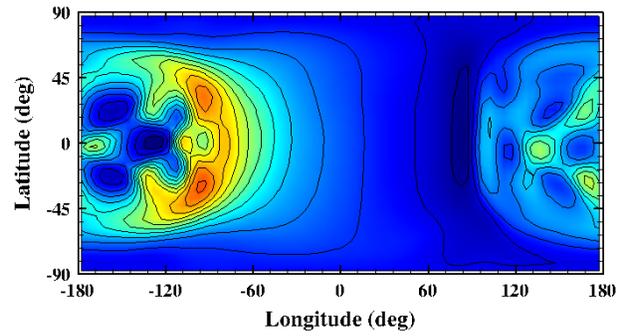

Moderate solar activity
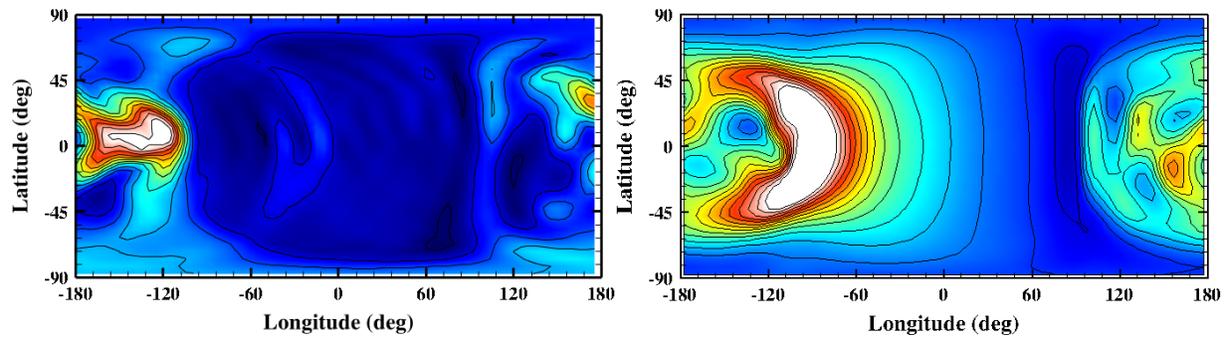
High solar activity
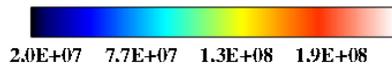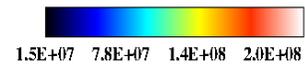
(a)   (b)

Figure 7.7. Solar cycle variation of thermal O for three solar activity levels. Low, moderate, high solar activities simulated by (a) MTGCM and (b) M-GITM.

The current M-GITM O distribution in the thermosphere is subject to strong global winds whose structure is primarily driven by solar heating and migrating tides. Consequently, the spatial distribution of O is more focused and symmetric about the equator as the focused flow from day-to-nightside builds up the O density on the nightside as shown in figure 7.7b. The inclusion of the missing nonmigrating tides into M-GITM will modify the spatial distribution of O by adding further asymmetry about the equator and suppressing the flow from day-to-nightside. This nonmigrating tides is included fro the MTGCM. Thus, the O distribution for the MTGCM is resulted in a smaller buildup and more asymmetric about the equator on the nightside than that for M-GITM.

As mentioned before, the spatial distribution of CO_2 shows anticorrelation with that of O (figure 7.8). Because of the relatively lighter O mass, the horizontal variation of O density is more likely to be homogenized by the atmospheric circulation than that of CO2 density. Consequently, CO_2 has a strong correlation in the distribution of density extrema with the distribution of high neutral temperatures, since the CO_2 distribution is more subject to temperature distribution than the O distribution. The spatial pattern of density is different in the MTGCM and M-GITM cases, but the correlation with neutral temperature is similar. The CO_2 density in the MTGCM case is populated in the polar regions, unlike the M-GITM CO_2 density that is populated at the subsolar regions and the late evening regions. The solar cycle variation in CO_2 density is a factor of ~3 and ~6 for the MTGCM and M-GITM cases, respectively, showing a larger solar cycle variation in M-GITM CO_2 density.
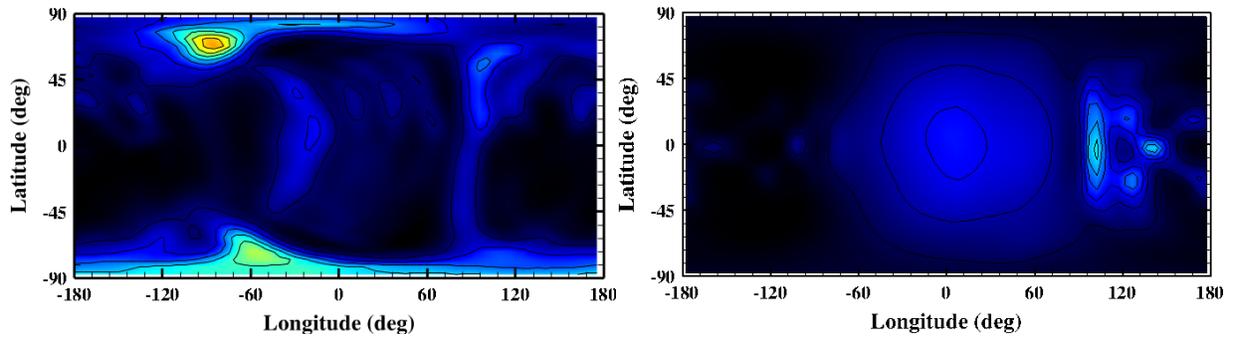
Low solar activity
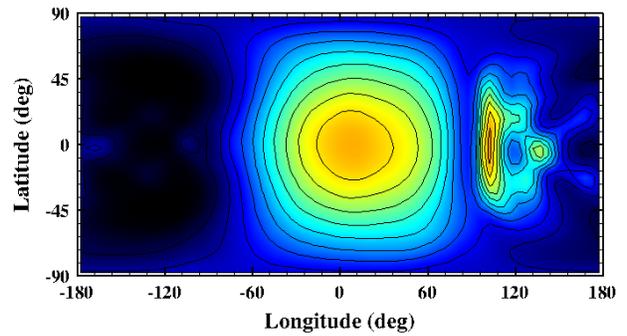
Moderate solar activity
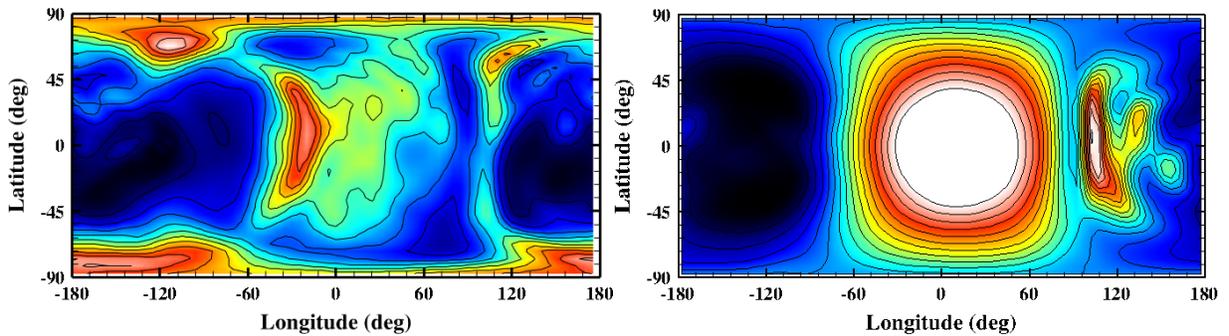
High solar activity
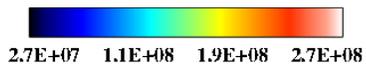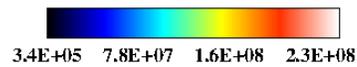
(a)   (b)

Figure 7.8. Solar cycle variation of thermal CO_2 for three solar activity levels. Low, moderate, high solar activities simulated by (a) MTGCM and (b) M-GITM.

153

Seasonal variability (figure 7.9) is recognizable by the spatial distribution of a corresponding species or temperature. From aphelion to perihelion, the maximum O density varies by a factor of ~2 and ~1.5, which is smaller than the solar cycle variability. Since an inverse correlation of O density with neutral temperature is evident in the density distribution, both the MTGCM O and M-GITM O exhibit highly concentrated density in the regions of low neutral temperature. More of the MTGCM O is populated near the poles (South Pole region for aphelion and North Pole region for perihelion), while on the equator for the M-GITM O. The missing nonmigrating tides yield a more focused O distribution for M-GITM near the equator, as the buildup of the O density between dusk and dawn appears to occur more broadly. Until the implement of topography into M-GITM, this O distribution affects the thermalization of hot species over a larger region through collisions at high altitudes than the MTGCM O does (topography included).

Aphelion ($L_s = 90°$)

Equinox ($L_s = 180°$)

Perihelion ($L_s = 270°$)

(a)

(b)
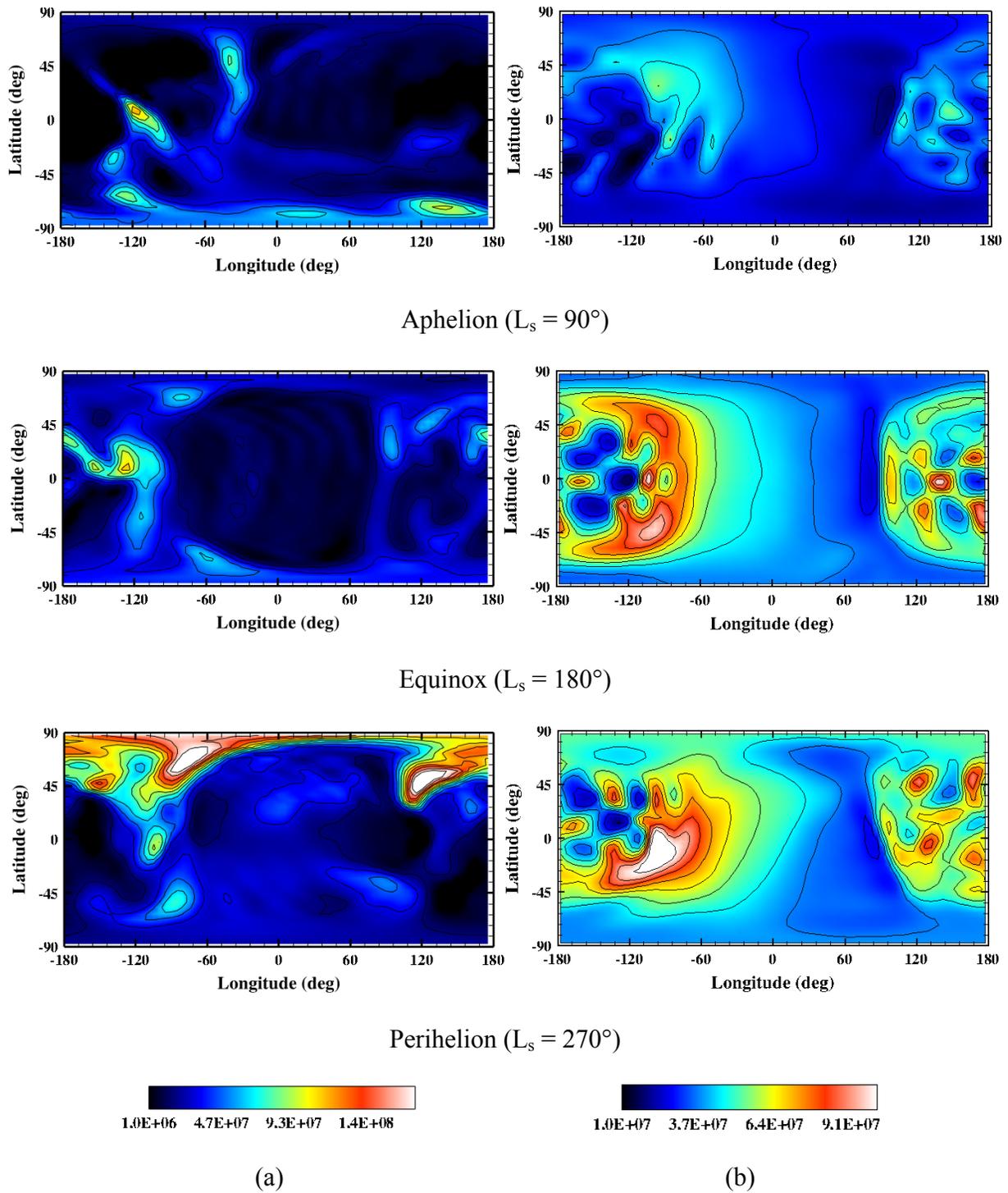
Figure 7.9. Seasonal variation of O for three representative orbital positions. Aphelion, autumnal equinox, and perihelion simulated by (a) MTGCM and (b) M-GITM.

The seasonal response of CO_2 density from both atmospheric models also exhibits the same correlation with the temperature and the global winds (figure 7.10). The seasonal variation of CO_2 density from the MTGCM and M-GITM is a factor of ~2.5 and ~3, respectively. The modeled CO_2 by M-GITM shows high CO_2 density in the late evening throughout three seasons, which follows closely the neutral temperature distribution shown in figure.7.6. This feature is absent in the density modeled by the MTGCM due to the effect of the nonmigrating tides. The absence of polar warming for M-GITM results in different distribution of CO_2 near the polar regions, compared to that of MTGCM the CO_2. As shown in figure 7.10, M-GITM CO_2 tends to be populated more near the equator during aphelion and perihelion than the MTGCM does. Correspondingly, the structures of the resulting hot corona are different for the MTGCM and M-GITM. The enhanced CO_2 density for M-GITM near the subsolar region and evening terminator thermalizes more hot species than the MTGCM CO_2. Thus, the horizontal distribution of hot species displays slightly different pattern, when the M-GITM thermosphere is used.
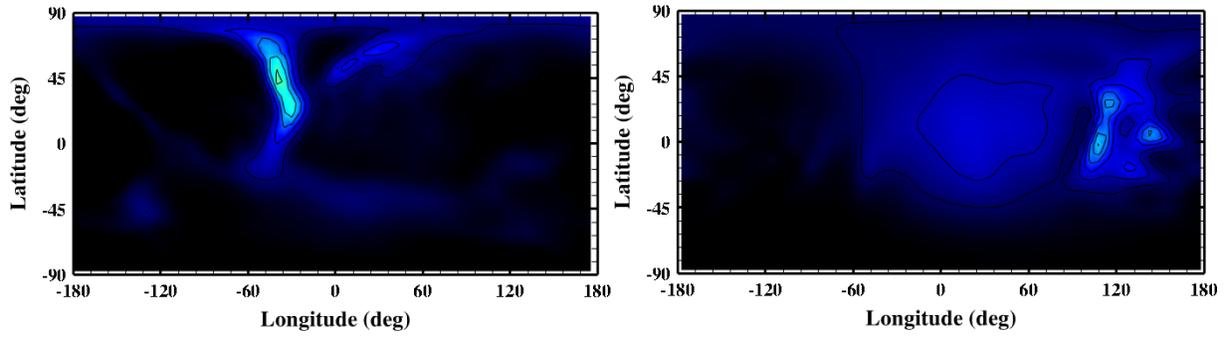
Aphelion ($L_s = 90°$)
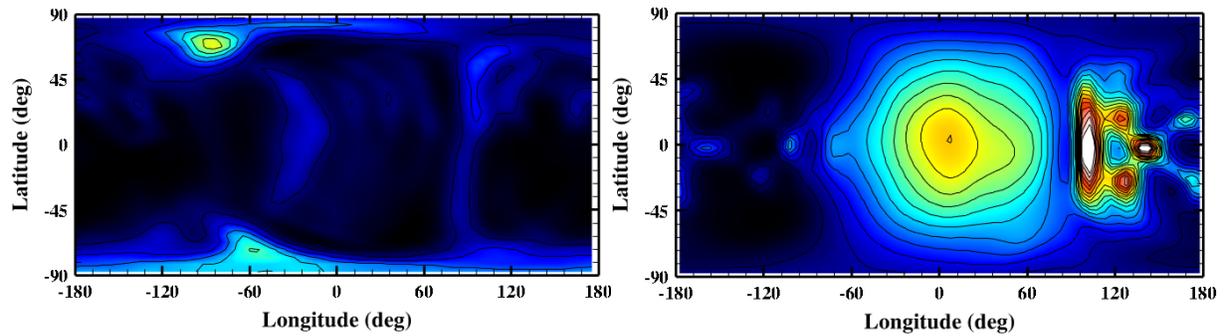
Equinox ($L_s = 180°$)
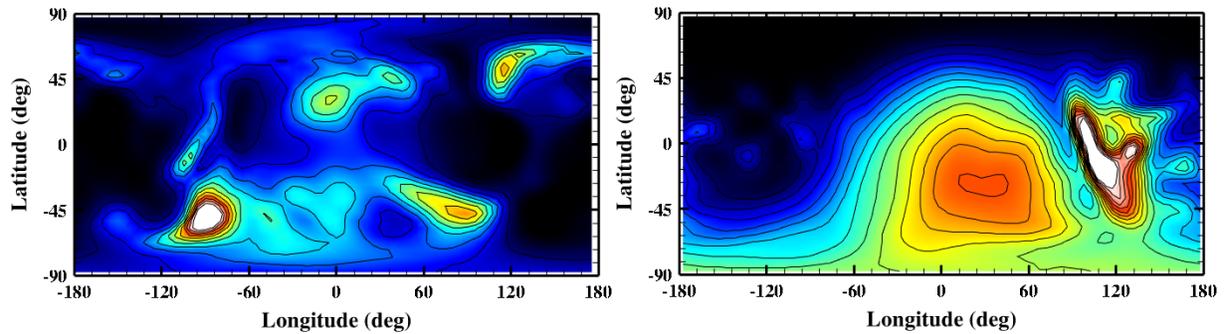
Perihelion ($L_s = 270°$)
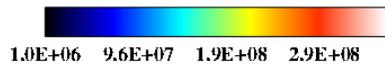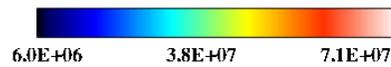
(a)   (b)

Figure 7.10. Seasonal variation of CO_2 for three representative orbital positions. Aphelion, autumnal equinox, and perihelion simulated by (a) MTGCM and (b) M-GITM.

VII.3.3. Ionosphere variation (O_2^+) / MTGCM and M-GITM comparison - Structure and features

Solar cycle variability in O_2^+ densities from both models is also manifested by an enhancement of density as expected with increasing solar activity. The spatial distribution does not change from solar low to high and retains the aforementioned spatial distribution pattern of density maximum and minimum. The M-GITM O_2^+ distribution shows only few spatial feature compared to that of the MTGCM. The missing nonmigrating tides from topography will add asymmetry to the M-GITM O_2^+, as the distributions of its parent molecules, O and CO_2, will be further modified. O_2^+ densities modeled by both models show similar solar cycle variation, which corresponds to the increase in density by a factor of ~3.7.

The variation over seasons is shown in figure 7.11. The effect of planetary tilt appears as the shift of the subsolar regions northwards and southwards for aphelion and perihelion cases, respectively, for both models. The localized features in the MTGCM O_2^+ are not shown in M-GITM O_2^+, such as high densities at high latitudes. Seasonal variability in O_2^+ density modeled by the MTGCM is a factor of ~1.7 and, that modeled by M-GITM is a factor of ~1.9. The M-GITM O_2^+ distribution is predominantly populated near the subsolar region, where it does not display the polar warming effect shown in the MTGCM O_2^+. Due to this difference, the local production rate of hot O will be more focused near the subsolar region, yielding in a different hot O corona density structure for M-GITM.
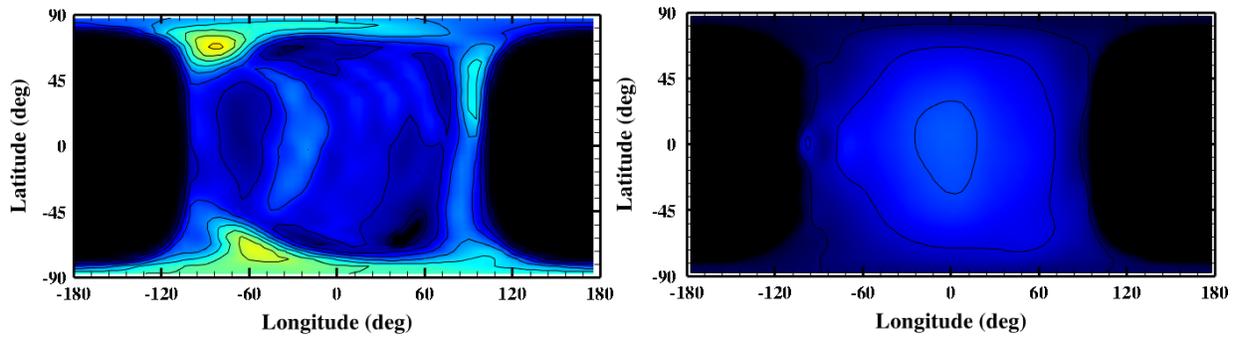
Low solar activity
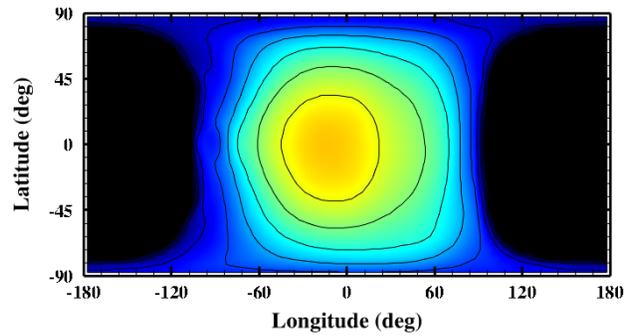
Moderate solar activity
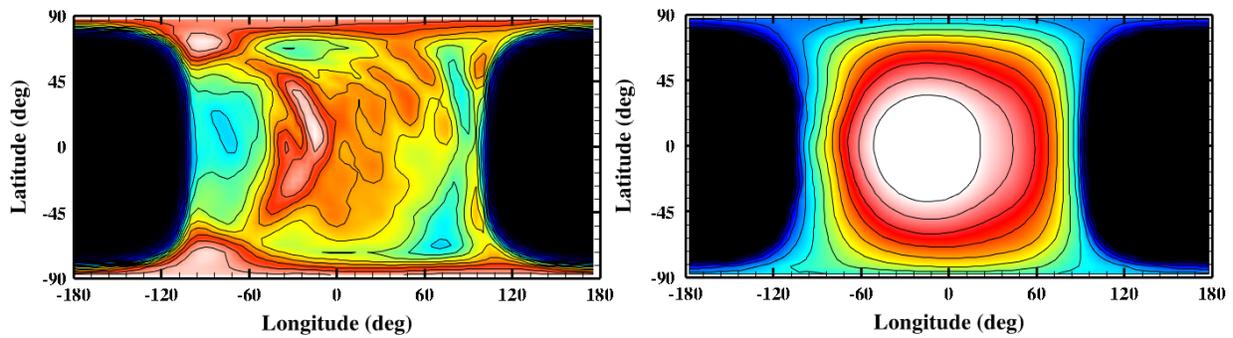
High solar activity
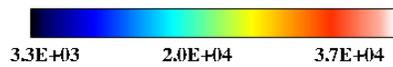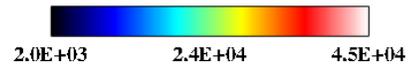
(a)   (b)

Figure 7.11. Solar cycle variation of thermal O_2^+ for three solar activity levels. Low, moderate, high solar activities simulated by (a) MTGCM and (b) M-GITM.

Aphelion ($L_s = 90°$)

Equinox ($L_s = 180°$)

Perihelion ($L_s = 270°$)

3.2E+03 1.9E+04 3.5E+04	9.9E+02 7.0E+03 1.3E+04
(a)	(b)
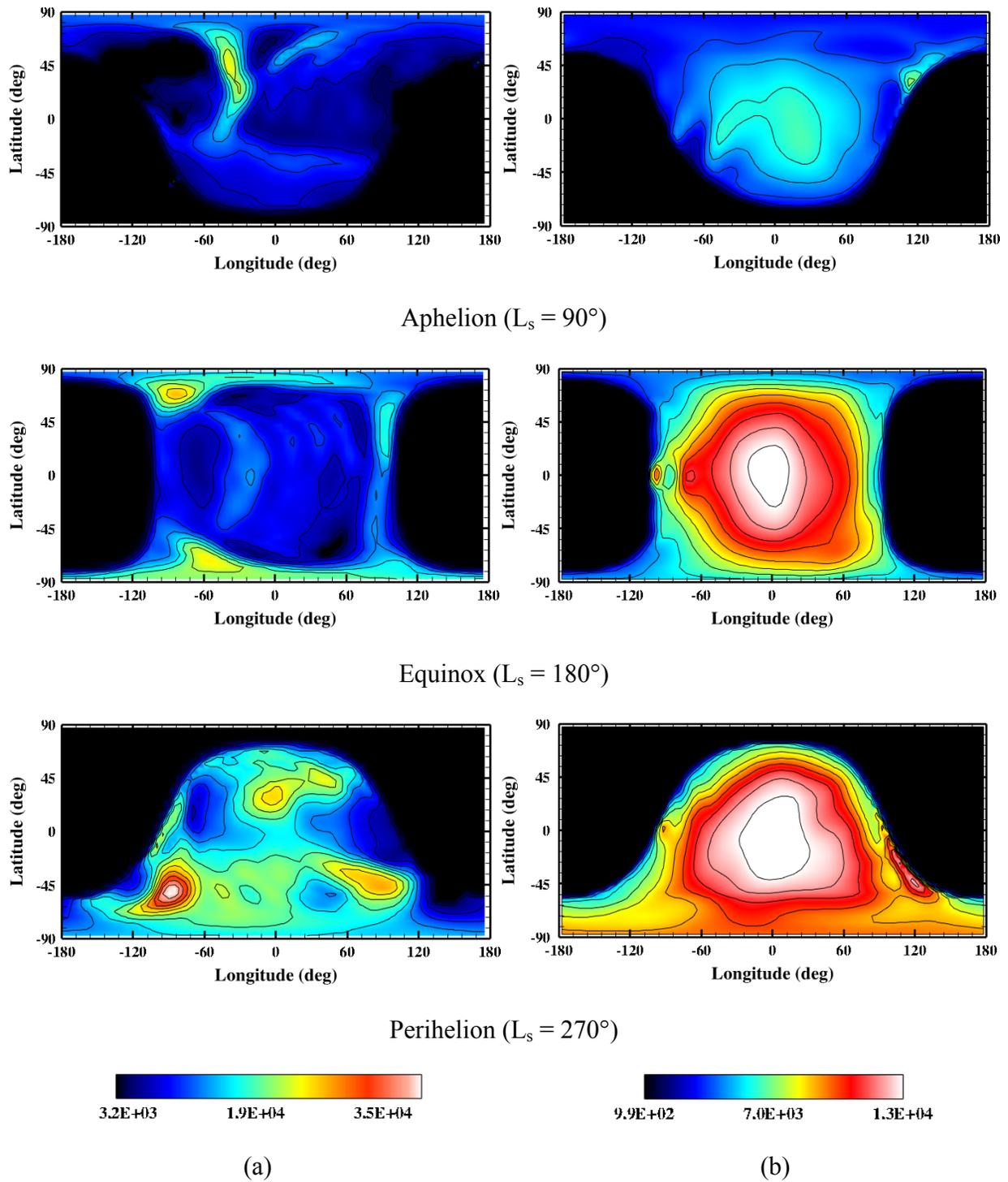
Figure 7.12. Seasonal variation of O_2^+ for three representative orbital positions. Aphelion, autumnal equinox, and perihelion simulated by (a) MTGCM and (b) M-GITM.

VII.4. Major thermospheric/ionospheric constituents' profiles (O, CO_2, CO, N_2, O_2^+, e)

Another key improvement in M-GITM is a larger altitude range of domain (surface of the planet – 300 km altitude) while the MTGCM resolves from ~70 km to 200 km. Figure 7.13 shows the profiles of the background thermospheric and ionospheric constituents, which are extracted at SZA 60° from the modeled atmospheres by the MTGCM and M-GITM. More of the lower atmosphere is captured in the M-GITM atmosphere than that of the MTGCM. Important atmospheric dynamics and density gradients, such as the ionospheric peak of O_2^+ and major thermalizing neutrals, in the lower atmosphere are available in M-GITM.

The escape probabilities calculated using both the MTGCM and M-GITM are consistent at higher altitudes – above ~165 km and ~200 km during low and high solar, respectively (figure 7.14). At lower altitudes, the collisions between hot and cold particles are highly probable, and the frequency of collisions is dependent on the ambient thermospheric condition. Consequently, higher pressure in M-GITM's atmosphere results in smaller escape probability at lower altitudes than that of the MTGCM, which is noticeable as some deviation in the escape probability curves in the lower atmosphere.
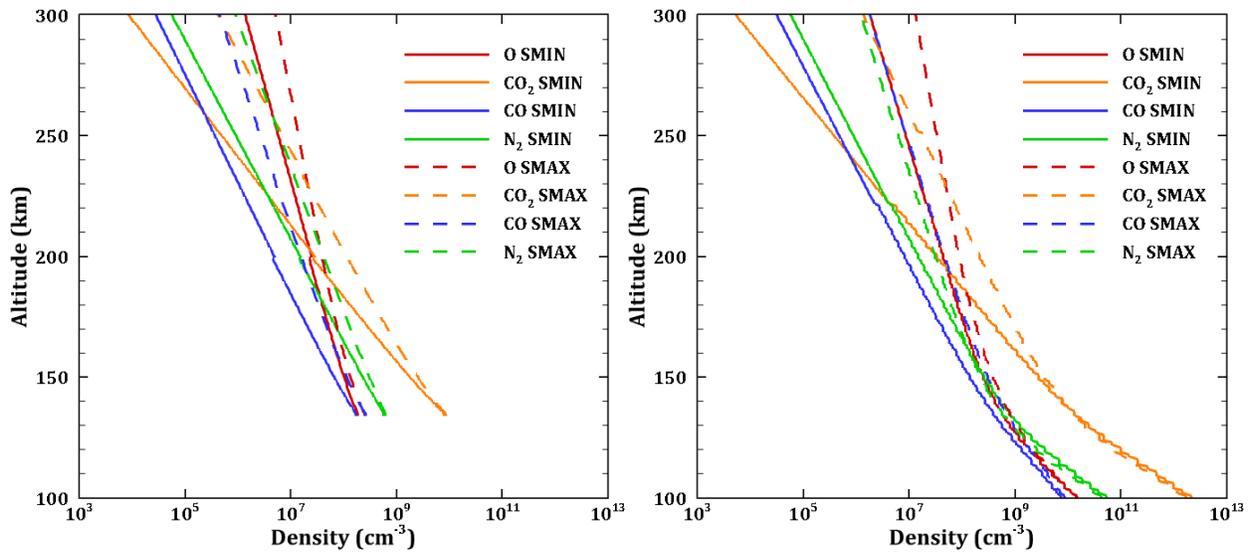
(a)
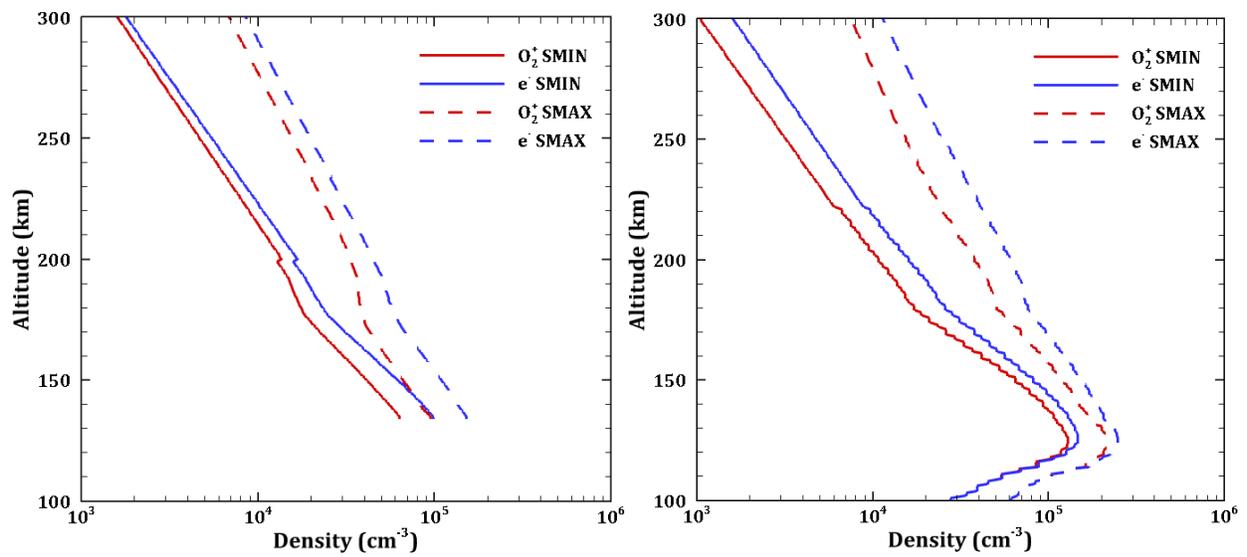
(b)

Figure 7.13. Profiles of (a) the major thermospheric species (O, CO_2, CO, and N_2) and (b) ionospheric species (O_2^+ and e) from the MTGCM (left) and M-GITM (right) for the low (solid) and high (dash) solar activity cases at equinox ($L_s = 180°$).
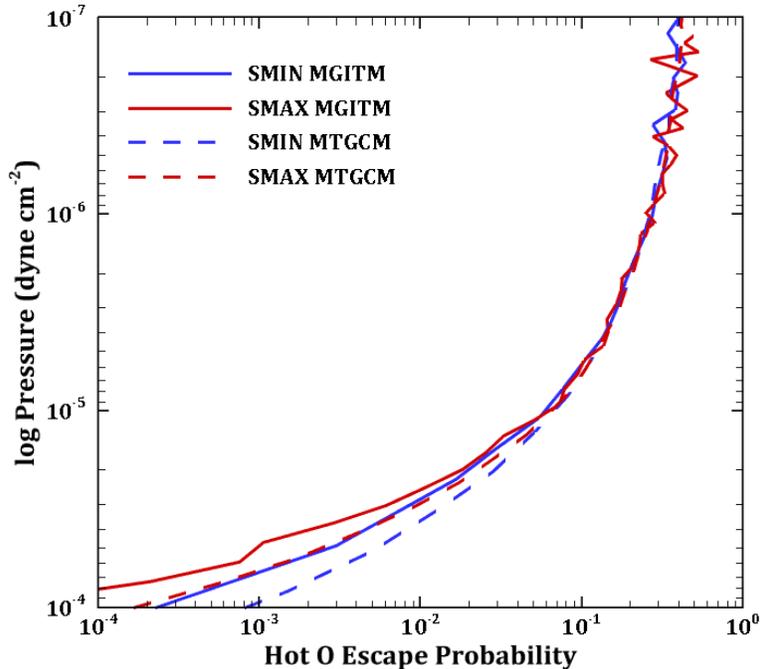
Figure 7.14. Escape probabilities computed using the MTGCM (solid) and M-GITM (dash) for the low (blue) and high (red) solar activity cases at equinox ($L_s = 180°$).

VII.5. Thermal O mixing ratio, O/(O+CO₂)

Thermal oxygen and carbon dioxide are the dominant thermospheric species. The O density surpasses that of CO_2 in the lower exosphere or the upper thermosphere, where the hot atomic corona is situated (see figure 7.13 - background species profiles). The altitude at which O surpasses CO_2 is dependent on the solar fluxes, since the thermosphere expands and the base of the exobase rises with increasing solar activity. The spatial distributions of O and CO_2 densities change in accordance with increasing heliocentric distance, where the local distributions of the sources and losses are driven by the effect of the global wind system and temperature.

As discussed in the previous section, the locations of high and low density regions of O and CO_2 are anti-correlated. In both models, the MTGCM and M-GITM, the model atmosphere below the homopause (~120 km) is where all species have the same horizontal velocity and scale

height. Above the homopause, which is the domain of this study, the atmospheric circulation modifies the mixing of the atmosphere. The model background species are expected to diffuse, according to their mass, both vertically and horizontally. This mechanism is one of the characteristics only inherent in 3D atmosphere models.

The effects of the global winds on the thermospheric species are clearly apparent in the distribution of the mixing ratio of thermal O, $O/(O+CO_2)$. In order to illustrate the influence of the wind diffusion, one can compare the polar regions for two extreme conditions (*i.e.,* aphelion low solar activity and perihelion high solar activity). Figure 7.15 illustrates the O mixing ratio for extreme conditions modeled by the MTGCM and M-GITM. Both of the modeled O mixing ratios show high O mixing ratios near the winter poles of two extreme cases. These effects are consistent with the winter polar warming that results from an increased adiabatic heating by the atmospheric circulation.
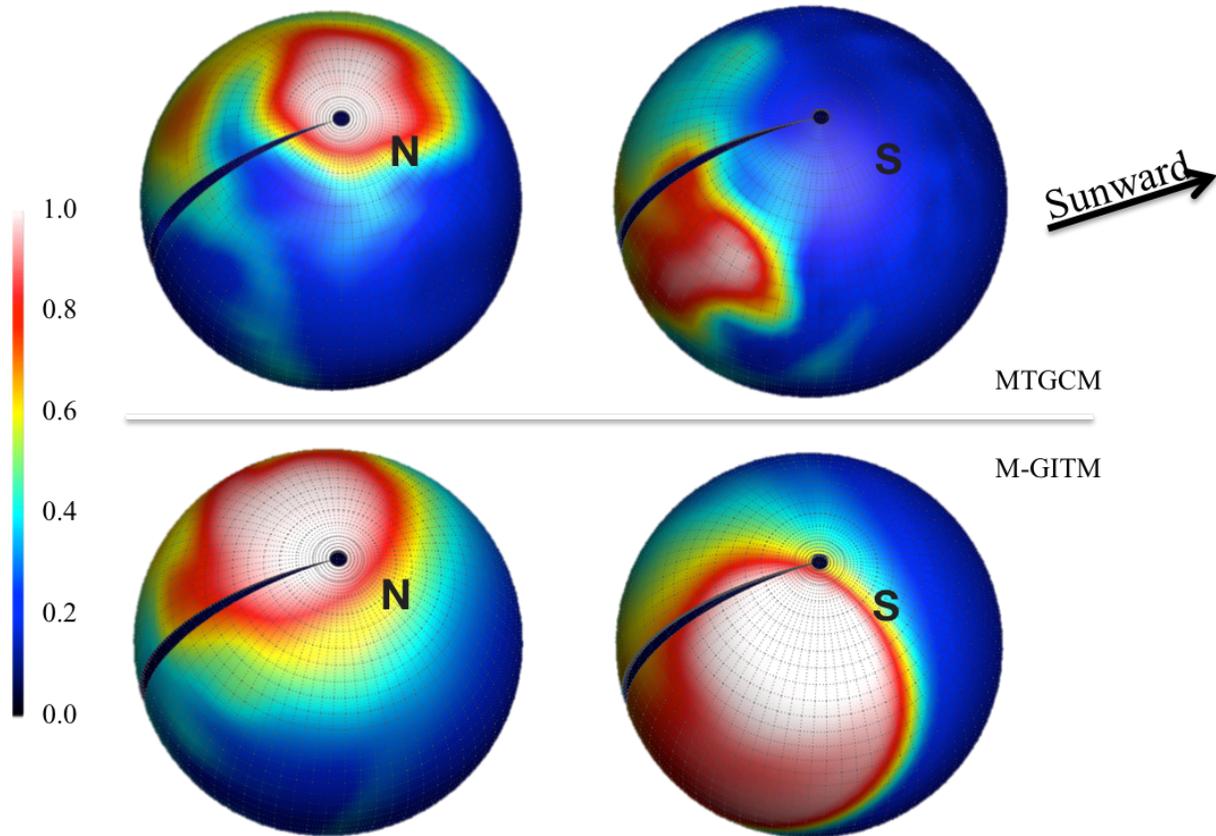
Figure 7.15. O mixing ratio, $O/(O+CO_2)$, from MTGCM and M-GITM for the perihelion/solar high (left) and aphelion/solar low cases.

The high O mixing ratio near the polar regions appears more broadly distributed in the M-GITM case, including the mid to high latitude regions. This may be caused by fewer features in the spatial distribution of density simulated by the current M-GITM. The explicit treatment of the vertical momentum of each constituent in M-GITM may provide a better description of this localized influence resulting from the atmospheric circulation.

Chapter VIII

Hot O corona with M-GITM

Understanding the mechanisms and structure of the Martian hot O corona is crucial for estimating the inventory of water and CO_2 on Mars. Comprehensive studies have included many theoretical and numerical modeling efforts. This chapter presents for the first time the hot O corona simulations with a newly developed thermosphere/ionosphere model, M-GITM, for a range of different solar activities and seasons. Also, exospheric O brightness is computed separately from the modeled hot O corona and is compared with the measurements obtained by ALICE onboard *Rosetta*.

VIII.1. Introduction to hot oxygen corona investigation

Investigating the nature of the escape of oxygen on Mars is critical to obtain a better understanding of the evolution of water and CO_2 inventory at Mars. Recent observations of the surface geomorphology suggest that water and CO_2 have played a key role in forming the present environment. As discussed in chapter 4, the main source mechanism of the Martian hot O corona at the current epoch is considered to be dissociative recombination of O_2^+ [*Cipriani et al.*, 2007; *Fox and Hać*, 1997b; *Fox and Hać*, 2009; *Fox and Hać*, 2014; *Hodges*, 2000; *Hodges,* 2002; *Kim et al.*, 1998; *Valeille et al.*, 2009a, 2009b; *Valeille et al.*, 2010a; *Yagi et al.*, 2012;], which is a nonthermal mechanism that can produce hot O atoms with a range of the energy above the escape energy. A few other minor source mechanisms have been suggested, such as dissociative

recombination of CO^+ and photodissociation of CO_2. Hot O produced in the lower thermosphere participates in heating the neutral atmosphere by transferring energy via collisions with other thermospheric constituents. Depending on the availability of its energy, the hot O that reaches near the upper thermosphere may escape to space or fall back to the thermosphere, forming the hot O corona.

The hot oxygen corona was observed by the ALICE instrument onboard the Rosetta spacecraft during a swing-by for gravity assist of Mars in February 2007 [*Feldman et al.*, 2011]. The detected OI 1304Å brightness from limb scans has been compared with the estimated brightness from the model simulation [*Lee et al.*, 2012]. This observed hot corona shows that hot neutral species play an important role in forming the current Martian upper atmosphere and exosphere.

The Martian hot O corona and escape of hot O atoms have been extensively modeled using various computation methods with a range of model parameters. Recent 3D atmospheric models have added more a realistic description of the atmospheric features and escape process to the simulation studies, which are inherently absent in lower dimension atmospheric models (1D/2D). Yet, the effects of adjusting model parameters have not been comprehensively explored in the 3D hot corona simulations.

All simulations of the Martian hot O corona presented in this chapter are conducted by using M-GITM as the thermosphere/ionosphere input to the kinetic particle simulator. This hot O corona study is the result from the framework that coupled M-GITM and Mars-AMPS for the first time (one-way coupling). Many of the model results contained in this chapter are being included in the MAVEN mission model library. While performing the exploratory model parameter investigation, a number of the final model parameters are chosen, which were

mutually agreed upon by several groups of modelers in order to fairly compare the model results with one another. In the following sections, representative model parameters are examined to understand the effects of each model parameter on the 3D escape processes. The solar cycle and seasonal variabilities of the hot O corona are investigated, followed by comparison studies with observations.

VIII.2. Model parameters – Autumnal equinox and low solar activity

M-GITM is used here as the model thermosphere/ionosphere for the first time for simulating the hot O corona model. In this section, M-GITM is pre-simulated at fixed solar and seasonal conditions by adopting F10.7 = 70 at Earth (low solar activity) and L_s = 180° (autumnal equinox). This section investigates the effects of different model parameters in the 3D coupled framework, which adopt the newly improved thermosphere/ionosphere model. The model parameters that will be considered in this section are (1) the initial energy of the parent molecular ion (O_2^+), (2) the number of hot atom's collision partners in the local background atmosphere, and (3) collision schemes for the collisions between a hot atom and cold atom/molecule in the Martian atmosphere.

VIII.2.1. O_2^+ vibrational distribution

Previous 3D hot O corona studies have considered the vibrational and rotational ground state of the parent molecular ion, O_2^+, for computing the exothermicities in the dissociative recombination reaction. As discussed in chapter IV, O_2^+ is a homonuclear diatomic ion that exhibits nonthermal distributions in the vibrational levels. This vibrational distribution of O_2^+ has computed by *Fox and Hać* [2009] (see also, *Fox and Hać,* 1997b; *Fox,* 1985, 1986) as a function

of altitude from 80 km to 400 km. *Fox and Hać* [2009] included additional vibrational levels of the vibrationally and electronically excited state of O_2^+ in their basic ionosphere model. Figure 8.1 shows the fractional population of vibrational level computed by *Fox and Hać* [2009] for levels of $v = 0 - 5$ for low and high solar activities. The modeled vibrational distribution below an altitude of about 150 km tends to become thermal, having most of the O_2^+ in the vibrational ground state, due to the highly collisional nature in the thermosphere.
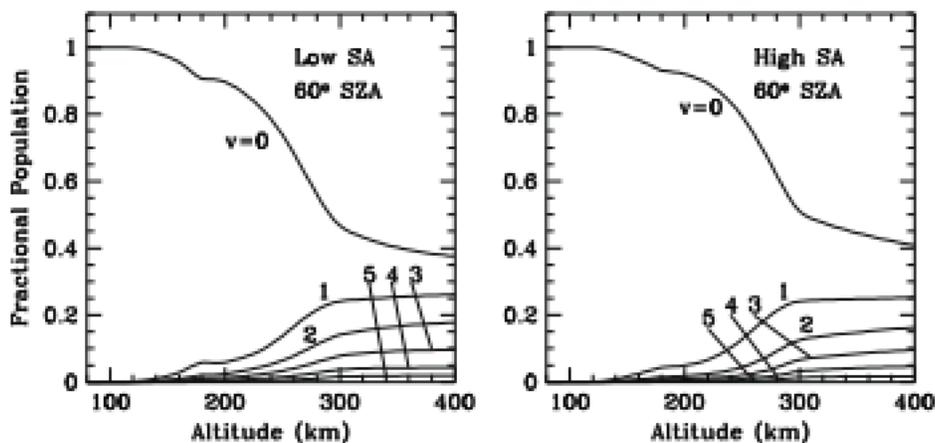
Figure 8.1. Computed vibrational distribution of O_2^+ for low (left) and high (right) solar activities by *Fox and Hać* [2009]. This is figure 6 in *Fox and Hać* [2009] study.

The computed energy distributions of the nascent hot O atoms are shown in figure 8.1. The energies of hot O atoms in the distribution are obtained from the source reaction, dissociative recombination of O_2^+, and have not been affected by any collisions with the ambient atmosphere. The contours show the probability density of the particles' energies as calculated in the laboratory frame. The white solid line indicates the escape energy of hot O, which is ~1.97 eV. There are three cases considered in this computation: (a) consideration of only vibrational ground state of the parent ion, (b) implementation of the vibrational levels of O_2^+, and (c)

inclusion of the vibrational dependence of the branching ratio. Case (c) is conducted by adapting the branching ratio variation with increasing vibrational level from an experimental study using the heavy-ion storage ring (CRYRING) [*Petrignani et al.,* 2005]. *Petrignani et al.* [2005] carried out a laboratory study that provides the vibrational dependence of the dissociative recombination reaction. The branching ratio dependence of vibrational levels is shown in table 8.1.

υ	$O(^1D)+O(^1S)$	$O(^1D)+O(^1D)$	$O(^3P)+O(^1D)$	$O(^3P)+O(^3P)$
0	5.8 ± 0.5	20.4 ± 0.3	47.3 ± 0.8	26.5 ± 0.8
1	13.9 ± 3.1	51.0 ± 5.4	27.8 ± 5.1	7.3 ± 7.5
2	21.1 ± 2.5	2.5 ± 2.1	76.4 ± 2.2	0.02 ± 0.03

Table 8.1. The branching ratio dependence of the vibrational levels of O_2^+. The branching ratio is in %. These values are obtained from the study by *Petrignani et al.* [2005].

As shown in the energy distribution of case (a) (figure 8.2), the energies of nascent hot O produced at lower altitudes are highly peaked in energies corresponding to the exothermicities in the dissociative recombination reaction. As altitude increases, the energy distribution becomes broadened due to the higher ion temperature at higher altitudes. The inclusion of vibrational information (figure 8.1) does not affect the energy distribution of case (a) by a large degree. The difference in the results is almost not noticeable, due to the fact that ~99% of the parent ions are predicted to be in their vibrational ground state in the lower atmosphere, where collisions are considerably frequent. Since the vibrational dependence is not considered in case (a) and (b), the relative probability density is consistent for both cases.

(a)

(b)

(c)
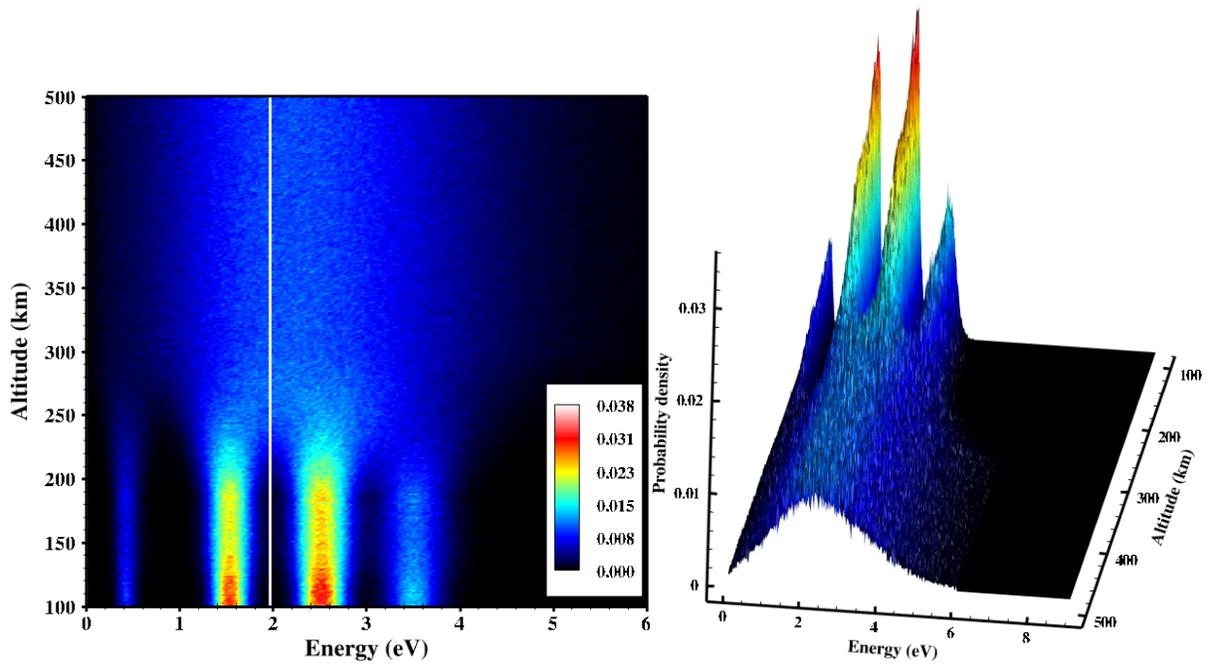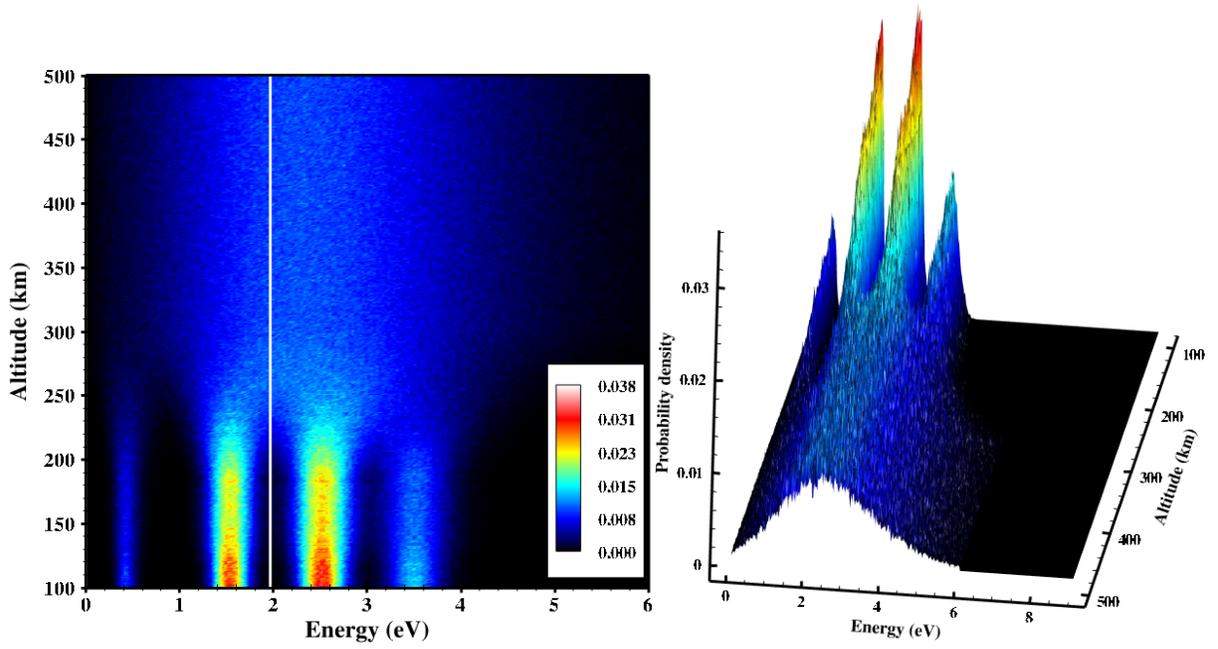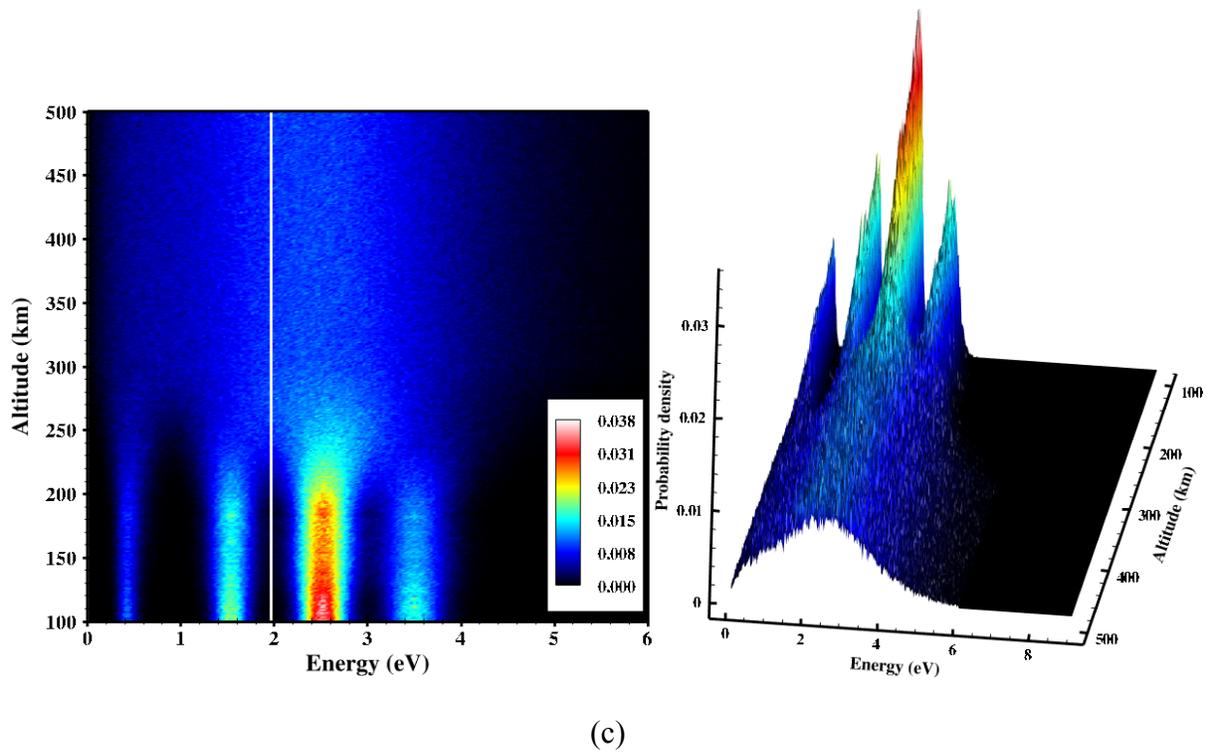
Figure 8.2. The computed energy distribution of the nascent hot O atoms for the altitude of 100 km − 500 km. All three distributions share the same contour scheme.

In case (c), the branching ratio is strongly dependent on the vibrational levels of O_2^+. The channels *C5* and *C2* in equation 4.10 (chapter IV) show substantial increasing in the $O(^1D)$ + $O(^1S)$ and $O(^3P)$ + $O(^1D)$ yields with increasing vibrational level from $\upsilon = 0 - 2$. As a result, the production of hot O via *C5* and *C2* noticeably increases compared to case (a) and (b). There are more hot O atoms produced with energy above the escape energy and more low energy O atoms at high altitudes in case (c).

172

(a)	(b)
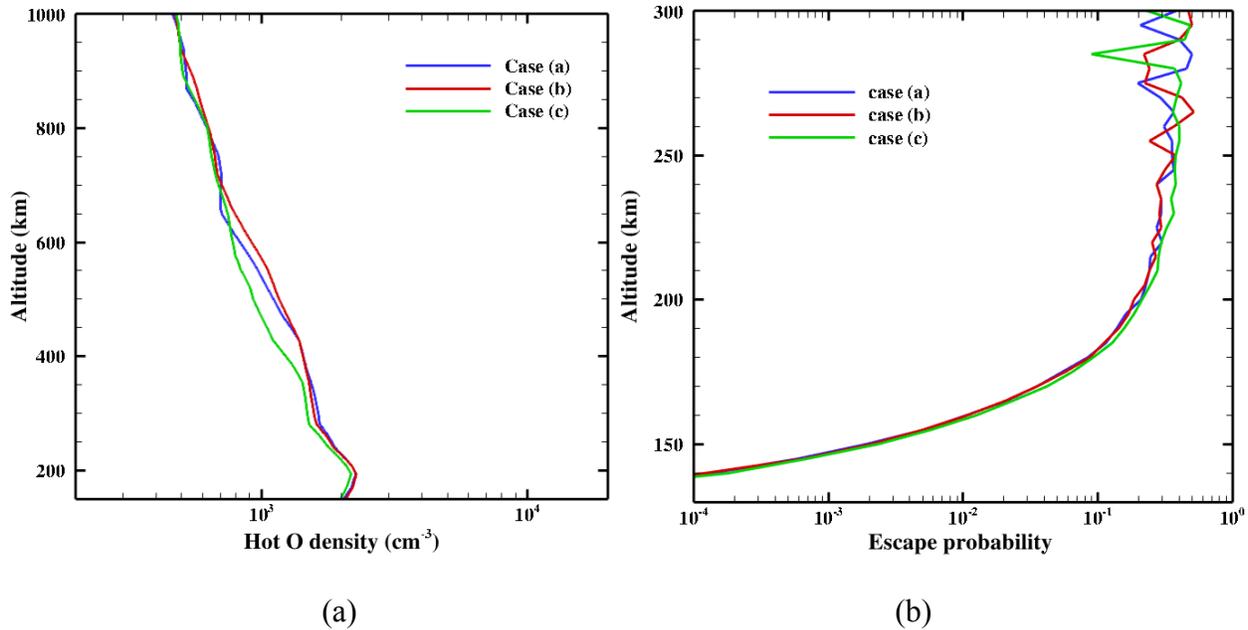
Figure 8.3. (a) Hot O density and (b) escape probability computed for case (a), (b), and (c).

Figure 8.3a and 8.3b show the simulated hot O densities and escape probabilities, respectively, from all three cases. The hot O densities shown here are extracted at SZA 60° in the direction of the equatorial east (late afternoon). It is logical to expect the differences in the results to be insignificant. The computed density profile for each case does not substantially deviate from each other, which indicates that the influence from each case is not considerable. It is expected that the escape probabilities also show the negligible effects from case (b) compared to case (a). For case (c), the computed escape probability slightly diverges from case (a) and (b) at high altitudes, which allows more escape of hot O in the sparse collision regime. As mentioned earlier, the contribution from the inclusion of the vibrational level is expected to be small, since the majority of the parent ions are in the ground state in the regions of high production of hot O. The implementation of the vibrational dependence of branching ratio is more effective in lower altitudes, where the local thermalization of hot O is high. An

independent but as yet unpublished 3D study by another modeling group [*Leblanc,* private communication, 2014] reached the same conclusion.

Case (a)	Case (b)	Case (c)
1.61×10^{25} s^{-1}	1.62×10^{25} s^{-1}	1.87×10^{25} s^{-1}

Table 8.2. Escape rates from case (a), (b), and (c).

The effects from case (b) and (c) is negligible to the density structure of the hot O corona. However, a slight increase in the resulting escape rates is shown in case (c) compared to that from case (a). The main difference between case (b) and (c) was the variable branching ratio, which allows more production of hot O with energy above the escape energy at higher altitudes. As a consequence, case (c) induces more escape of hot O than other cases, resulting in the increase of the escape rate by ~16% (table 8.2).

VIII.2.2. Scattering approximations

As pointed out earlier in chapter II, where two different collision schemes are exclusively investigated, the collision approximation in modeling of the hot O corona is crucial for determining the energy distribution of hot O. In reality, the collision cross section for each collision partner is certainly not an idealized hard sphere collision with isotropic scattering. However, there are only a few realistic descriptions (*i.e.,* differential scattering) of scattering that are available, and angular dependency is not often considered.

This section studies the impacts of the forward scattering assumption versus isotropic scattering assumption for the collisions with thermal oxygen. For the purpose of comparing the

174

effects of using different collision schemes, O_2^+ ions in the dissociative recombination reaction are assumed to be electronically and vibrationally in the ground state.

The momentum transfer cross sections for both schemes were calculated earlier, and the momentum transfer mean free path is given by,

$$\lambda_M = \frac{1}{n_{cold}\sigma_M},$$

(8.1)

where n_{cold} is thermal constituent's number density, and σ_M is the integrated momentum transfer cross section for the collisions between hot and cold particles. Knowing the mean free path of momentum transfer or the transport mean free path, the collision frequency for momentum transfer is defined as

$$\upsilon_M = \frac{\upsilon_{hot}}{\lambda_M},$$

(8.2)

where υ_{hot} is the mean velocity of hot particles.

For instance, for the isotropic scattering case of O_{hot}-O_{cold} collisions, the collision frequency is always equivalent to the collision frequency for momentum transfer, since $\sigma_T = \sigma_M$. Contrarily, in the case of forward scattering, the momentum transfer mean free path that is longer than the mean free path ($\sigma_T > \sigma_M$) results in the smaller collision frequency for momentum transfer than in the isotropic scattering case. Despite the large total cross section due to the highly peaked cross sections in forward direction, the rate of momentum transfer is always inversely related to the total cross section in the forward scattering scheme.
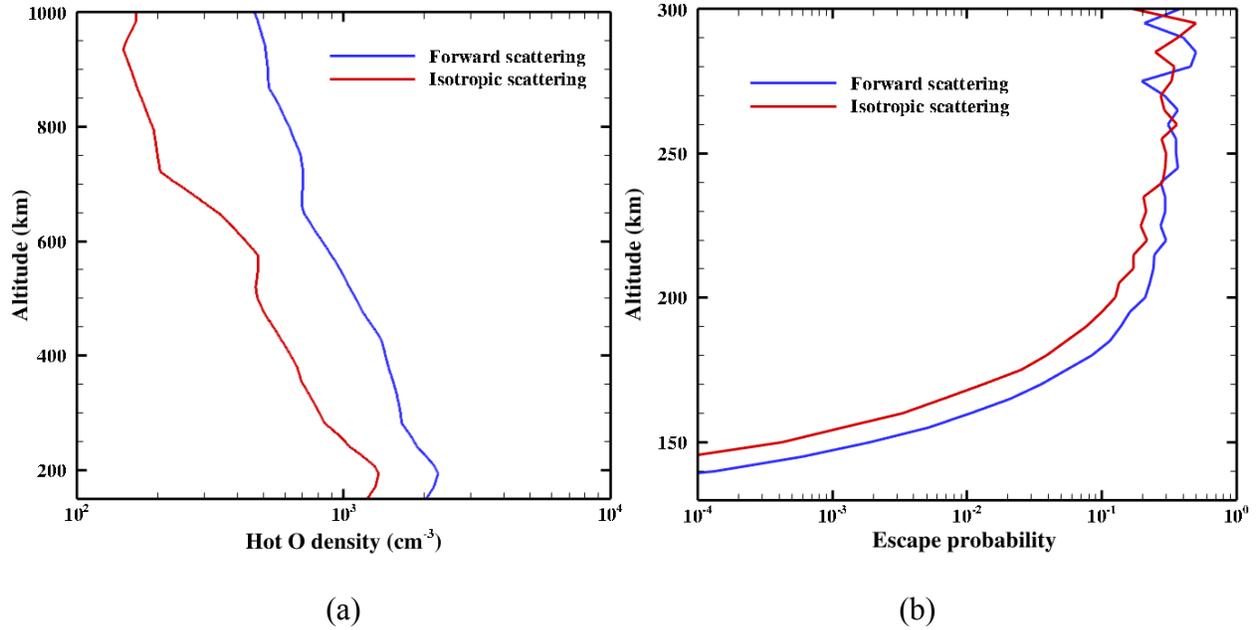
Figure 8.4. (a) Hot O density and (b) escape probability computed using forward scattering and isotropic scattering schemes.

Since the scattering of hot particles with other neutrals in the thermosphere governs the ultimate energy distribution of hot particles, changes in the density structure of the simulated hot O might be expected. Figure 8.4 shows the difference resulting in the simulation by using different scattering assumptions. The density computed from the isotropic scattering case is decreased by a factor of ~ 2.5, and this difference becomes slightly larger at higher altitudes. As expected, the isotropic scattering scheme transfers the momentum and energy more effectively than the forward scattering scheme does. At ~190 km altitude, where the probability curves show a sharp turn and begin to converge, the escape probability for the forward scattering case is larger by a factor of about 1.5 than the isotropic scattering case.

Scattering scheme	Isotropic scattering	Forward scattering
Escape rate	0.77×10^{25} s^{-1}	1.61×10^{25} s^{-1}

Table 8.3. Escape rates computed using two different scattering schemes.

The global escape rate for the isotropic scattering case is estimated to be about 50 % less than that for the forward scattering case (table 8.3). For a more realistic description of the hot O corona, these results imply the importance of describing the nature of collisions in detail. However, this difference in the total escape rates is not as large as estimated by *Fox and Hać* [2009].

VIII.2.3. Background atmospheric constituents

A newly produced hot O atom on Mars will encounter collisions with a background atom or molecule in the thermosphere. The local collision frequency is highly dependent on the densities of the local background collision partners and is directly related to the thermalization of hot particles. The coupled framework does not include all thermospheric constituents that reside in the atmosphere as collision partners for a hot particle, due to (1) the limitation of computational time and resources and (2) lack of studies on the collision cross sections for collisions of O with the thermospheric species except for a few species.

Presently, O and CO_2 are the most commonly chosen collision partners of hot O in many studies, since they are the major constituents in the thermosphere. Besides O and CO_2, CO and N_2 may also play important roles in the thermalization process of hot O in the upper thermosphere. As shown in the profiles of all collision partners (figure 7.13, chapter VII), the CO and N_2 densities are comparable with O and CO_2 above an altitude of ~150 km for low solar activity condition. They exceed the CO_2 density in the exosphere where the inclusion of CO and

N_2 may promote more thermalization of hot O near the exosphere. The inclusion of two more species as collision partners provides a more realistic description of the mechanisms that impact the structure of the hot O corona.

Figure 8.5 displays the spatial distributions (~200 km altitude) of all 4 collision partners of hot O for the equinox and low solar activity condition (M-GITM). The CO and N_2 density distribution patterns resemble that of the CO_2 density. The high-density regions are situated in the subsolar region and the late evening region from the equator to the mid latitudes. The minimum density is achieved at the nightside for both CO and N_2. The N_2 density is even more comparable to that of CO_2 at high altitudes than the CO density, which indicates that inclusion of CO and N_2 will provide nonnegligible impacts on the total simulation result.

As expected, additional collision partners resulted in greater thermalization of the hot O density. The extracted hot O density in figure 8.6 shows that the overall hot O density is decreased by a constant factor of ~1.5. The effect of including CO and N_2 in the background atmosphere is quite large, which suggests that the background species for the hot corona simulation should include at least these four species, O, CO_2, CO, and N_2.
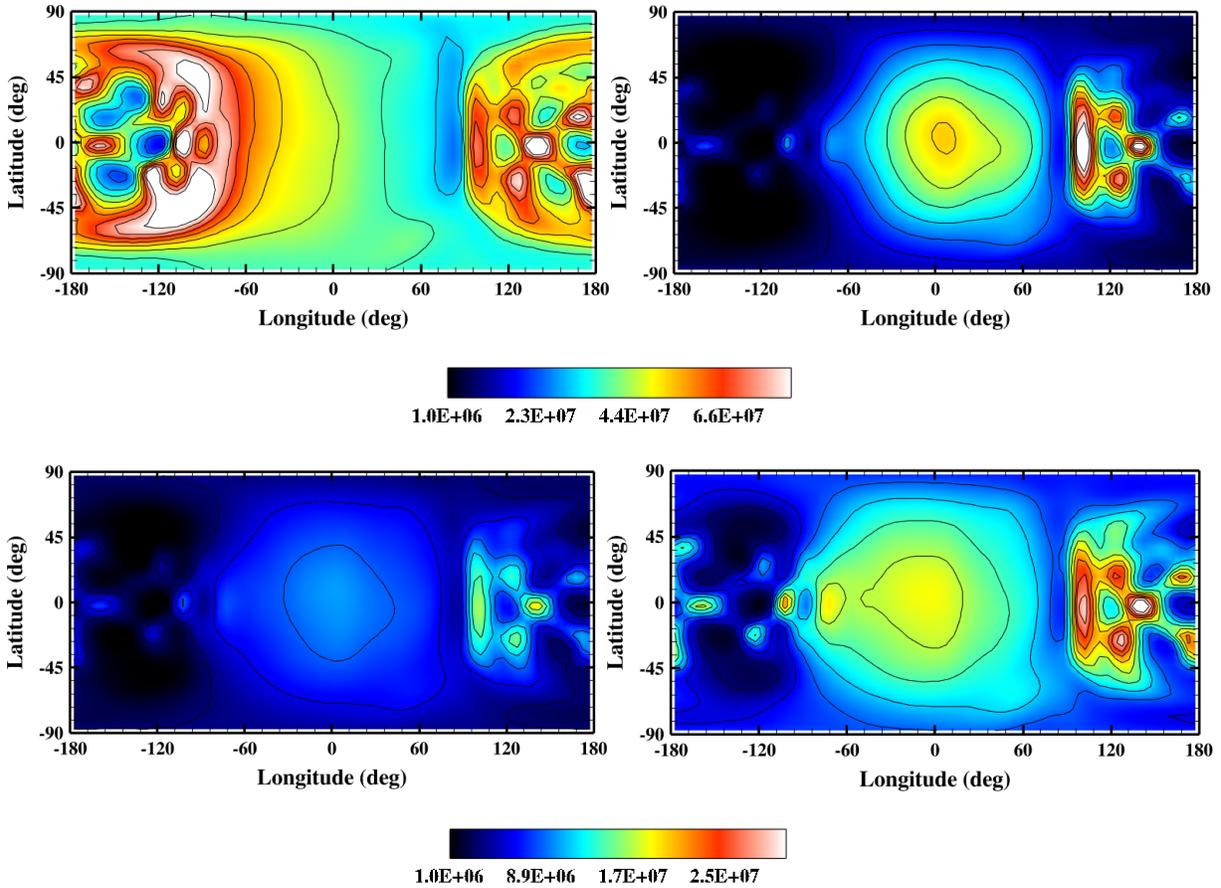
Figure 8.5. O, CO_2, CO, and N_2 density distribution at an altitude of ~200 km for the equinox and low solar activity condition. The color contours are considered separately for O-CO_2 and CO-N_2.

The escape of hot O is less probable when CO and N_2 are added as collision partners. Figure 8.6b shows the decrease in the escape probability of hot O for all altitudes, where the concentration of all four collision partners are dense enough to thermalize more hot O than just two species (O and CO_2) can do. Above ~210 km altitude, the collisions becomes so infrequent that additional background species do not make a large difference in the escape probability.

(a)   (b)
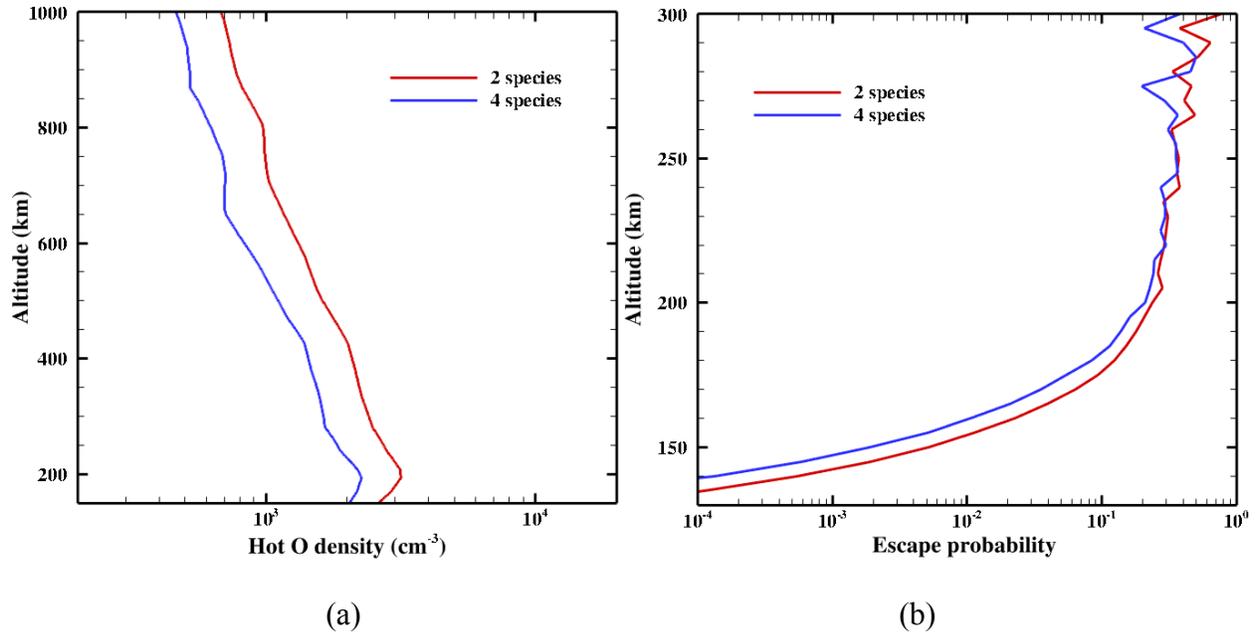
Figure 8.6. (a) Hot O density and (b) escape probability computed using different number of collision partners in the background atmosphere.

Table 8.4 lists the computed escape rates from the two models for the cases considered in this section. The escape rate is decreased about 40 % from the case in which only O and CO_2 are the background species. This significantly impacts the hot atomic corona simulation, which requires more detailed models for the O_{hot}-CO_{cold} and O_{hot}-$N_{2,cold}$ collisions.

Number of collision partners	2 (O and CO_2)	4 (O, CO_2, CO, and N_2)
Escape rates	2.67×10^{25} s^{-1}	1.61×10^{25} s^{-1}

Table 8.4. Escape rates computed by using 2 background species (O and CO_2) and 4 background species (O, CO_2, CO, and N_2).

VIII.2.4. Escape probability

Escape probabilities are computed for the cases considered in the previous section, using a different set of model parameters − implementation of O_2^+ vibration levels, different collision schemes, and inclusion of neutral collision partners in the background atmosphere. Since model

180

parameters play a crucial role in controlling the escape process of hot atoms, the escape probability is important to be checked to see the effects of model parameters at different levels of altitude.
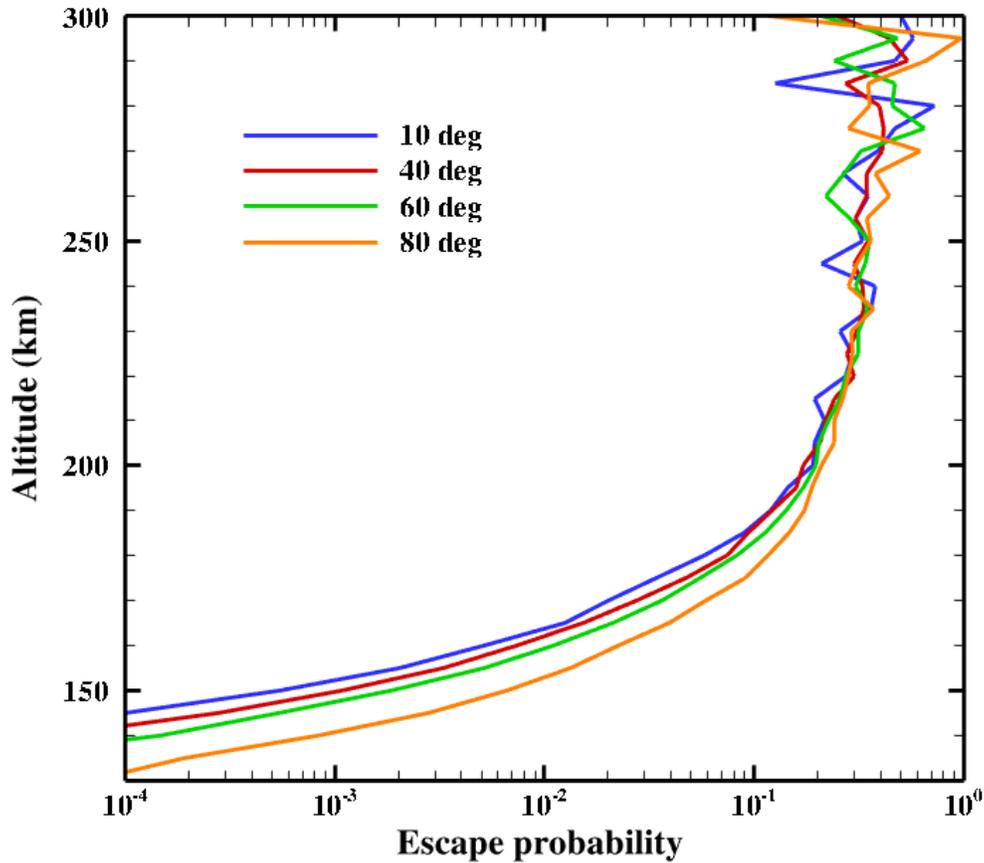
Figure 8.7. Escape probability calculated by selecting different SZA regions as hot O source.

In 1D atmospheric models, the escape probability calculation does not require an assumption of horizontal variation of the atmosphere since a 1D model is based on the plane-parallel and/or 1D-spherical atmosphere assumption. In order to calculate the escape probability in the 3D atmosphere model, a particular section of the dayside atmosphere should be selected for injecting hot particles. For example, a typical escape probability computation chooses a cone

with its apex angle of 60°, where this angle corresponds to solar zenith angle and the apex point is at the center of the planet, as the location of generating hot atoms. Utilizing the advantage of the 3D atmospheric model, escape probabilities are calculated for different solar zenith angle (SZA) (figure 8.7) to see the SZA dependence of escape probabilities.

The SZA considered here are 10°, 40°, 60°, and 80°, where 10° and 80° are considered to represent the extreme SZA's (*i.e.,* near the subsolar and polar regions). The resulting escape probabilities are shown in figure 8.7. The irregularities at high altitudes are caused by the sparse particles in the upper atmosphere. Generally, the escape probabilities at low altitudes show the strong dependence of SZA. The probabilities converge to a value (~0.5) as altitude increases. The spatial distributions of thermal O and CO_2 discussed in the previous section show that both densities reach the local minimum (for equinox) in the regions near the poles. Consequently, the escape probability becomes higher with increasing SZA due to the decrease in the density of species that are responsible for the effective thermalization of hot O. These phenomenon ceases as altitude increases since collisions are infrequent in the upper atmosphere.

VIII.2.5. Summary of model parameter analysis

This section (chapter 8.2) investigated the functionality of important model parameters and emphasized the characteristics of the three-dimensional atmosphere. The hot O density was least affected by the different treatments for the vibrational distribution of O_2^+. Although effects were not significant, it was found that the distribution of nascent O was changed the most by including the variation of branching ratio as a function of vibrational level. The model parameter change with the largest influence was using different scattering assumptions. The effect is much larger than that by including additional atmospheric constituents. Overall, the forward scattering

assumption and four species (O, CO_2, CO, and N_2) in the neutral atmosphere with the O_2^+ in the vibrational ground state are found to generate the most realistic and reasonable results. Figure 8.8 shows the total O density simulated using this set of parameters. Both the hot O and cold O profiles were extracted at SZA 60°. The ratio between cold O and hot O describes the transition from the cold O populated region to the hot O populated region. The approximated transition altitude varies and is strongly dependent on the atmospheric conditions.
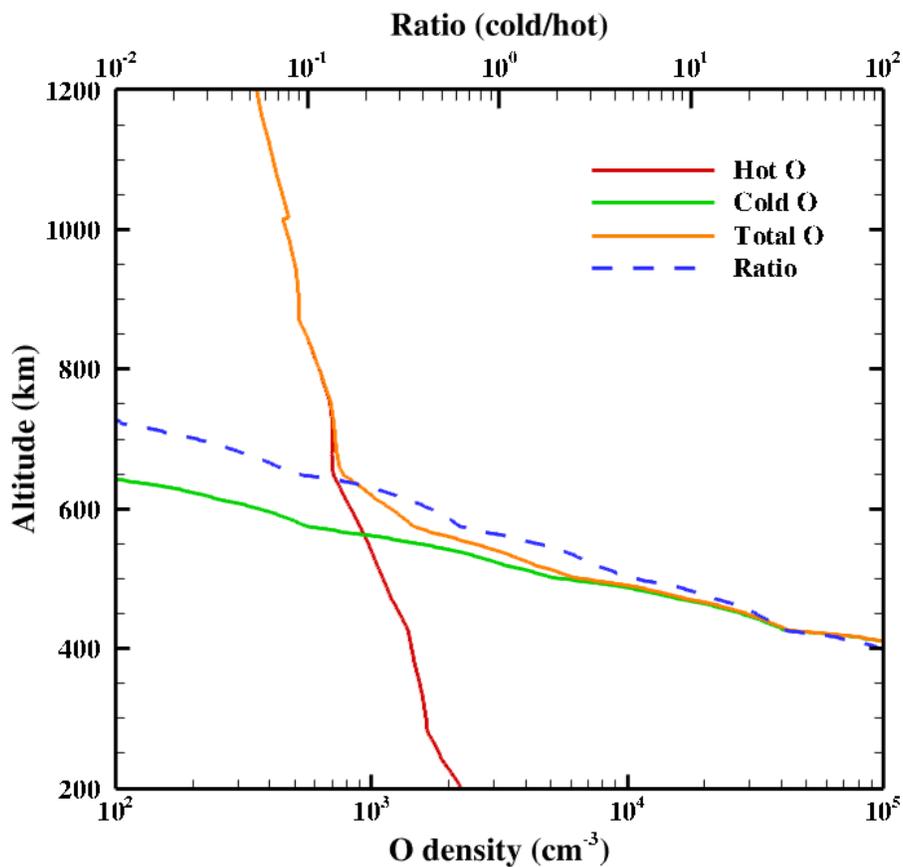
Figure 8.8. Total O (solid) density profile for the autumnal equinox and low solar activity case. The density profile of the hot O produced from the dissociative recombination reaction (red) is extracted at SZA 60°. Thermal O (cold O) density profile (green) is extracted from M-GITM. The cold C/hot C ratio is shown in blue dash line.

VIII.3. Solar cycle and seasonal variabilities

The escape process is strongly dependent on the variable solar EUV-UV fluxes and the orbital position of Mars. This hot oxygen study is carried out by using M-GITM as thermosphere/ionosphere input to the particle simulator. As introduced earlier, the variability of solar cycle is described by utilizing three different F10.7 indices measured at Earth – F10.7 = 70 (low solar activity), 130 (moderate solar activity), and 200 (high solar activity). The seasonal variability of the hot O corona is represented by considering four different orbital positions of Mars – aphelion (L_s = 90°), autumnal / vernal equinox (L_s = 180° / 0°), and perihelion (L_s = 270°).

VIII.3.1. Solar cycle variability

The variation of the solar EUV-UV fluxes on the top of the atmosphere drives a strong solar activity dependence of the Martian hot O corona. As in the hot C corona investigation in chapter VI, the solar cycle variability in the hot O corona is also characterized as the enhancement of the hot O density and the expansion of the overall volume of the corona. Using M-GITM as the thermosphere/ionosphere input to the exosphere model, the solar cycle variability is described by three solar activity conditions with a fixed orbital position (autumnal equinox, L_s = 180°). In any case, these cases can be abbreviated as AEQUMIN, AEQUMED, and AEQUMAX, respectively, as defined in chapter 7.
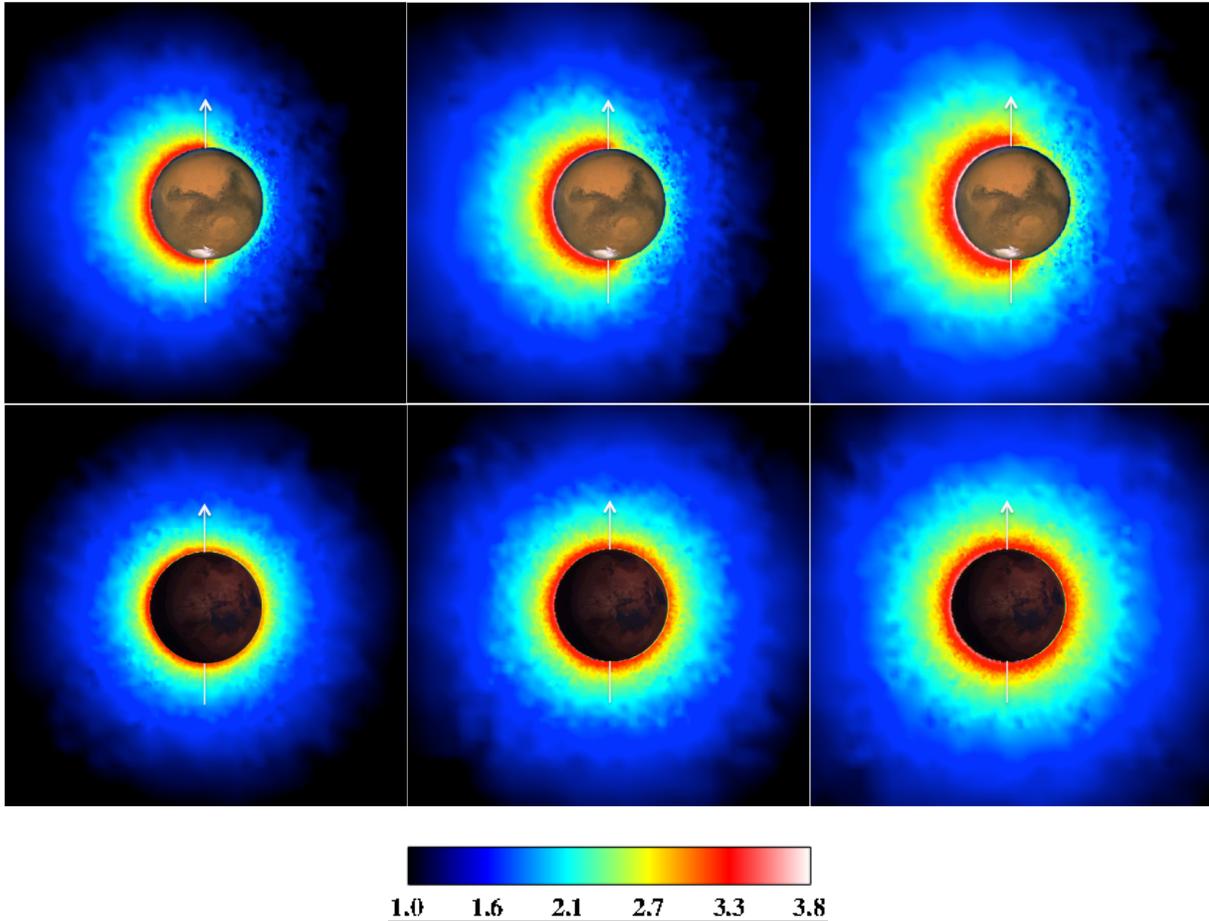
Figure 8.9. The simulated hot O densities, from the left to right, for the AEQUMIN, AEQUMED, and AEQUMAX cases. Top panel show the noon-midnight meridional plane. Bottom panel show the nightside (dawn-dusk plane). The color contours indicates the logarithm of density (cm^{-3}).

The simulated hot O densities for the AEQUMIN, AEQUMED, and AEQUMAX cases are displayed in figure 8.9. The overall spatial features of the hot corona are consistent from solar low to high, where the shape of the hot corona is an elongated spheroid with a radially expanded dayside and flatter nightside. As a consequence of high source densities near the subsolar region, the hot O density reached a maximum on the dayside centered at the subsolar region and exponentially decreases with increasing distance from the planet. The bottom panel of figure 8.9 illustrates the slightly low hot O density near the morning terminator regions. This is due to the

local minimum of the source and more thermalization by thermal O in this region. The nightside also exhibits hot O density, which is the aforementioned "bouncing effect," resulting in the diurnal variation in density by a factor of about 10. The hot O density in the dayside varies by a factor of ~2.5 from the low to high solar activity conditions.

VIII.3.2. Seasonal variability

For the investigation of seasonal variability, the pre-simulated cases by M-GITM are the aphelion, vernal equinox, autumnal equinox, and perihelion case at a fixed solar condition (low solar activity, F10.7 = 70) – hereafter, APHMIN, VEQUMIN, AEQUMIN, and PERMIN cases. In addition to the MTGCM cases, one additional seasonal cases, vernal equinox, in the hot corona simulations using M-GITM as the thermosphere/ionosphere input expands the seasonal investigation. At vernal equinox ($L_s = 0°$), spring in the Northern hemisphere, the temperature and global winds structure are somewhat different from those at autumnal equinox, *i.e.,* fall in the Northern hemisphere.
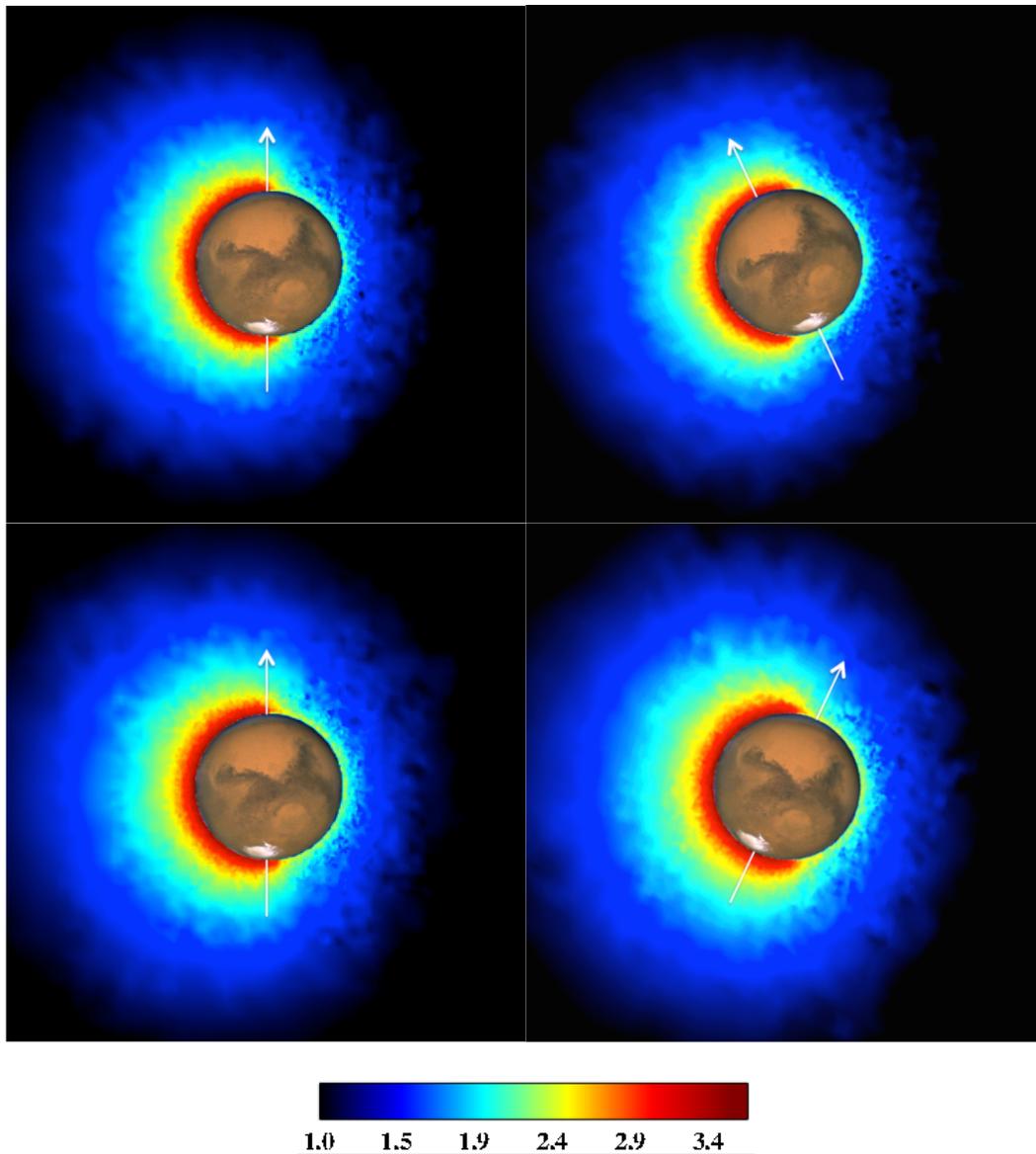
Figure 8.10. The simulated hot O densities, from the top left figure in clockwise direction, for the VEQUMIN, APHMIN, AEQUMIN, and PERMIN cases. The noon-midnight meridional plane is shown where Sun is located to the left. The color contours indicates the logarithm of density (cm^{-3}).

The seasonal variability of the hot O corona is characterized by the structure of the corona rather than the magnitude of the density. The geometrical shape of the hot corona (*i.e.,* elongated spheroid) remains the same for different seasons, as shown in the simulated hot O coronae in figure 8.10. However, the shift in the subsolar point toward the North and South for

the aphelion and perihelion cases, respectively, produces a shift of the maximum hot O regions over the summer pole. Unlike the solar cycle variation in the hot O corona, the magnitude of the hot O density in the corona does not change significantly. As discussed before, the solar cycle variability of the hot corona is characterized as the variable solar EUV-UV in the upper atmosphere. At a fixed solar condition, the impact on the atmosphere at different orbital positions of Mars are rather characterized as the influence of the longer wave solar IR flux, in the lower atmosphere. Consequently, the lower atmosphere expands because of the absorption of the solar IR with increasing heliocentric distance.

Overall, the size of the hot O corona is not changed dramatically over the seasons. The hot O corona for the AEQUMIN case shown in figure 8.10 (left top and bottom) appears to be slightly more enhanced and expanded (almost not noticeable in the figure), compared to that of the VEQUMIN case. This slight enhancement is due to higher temperature and O_2^+ density in the AEQUMIN case, which produce the difference between the two equinoxes separated by 180° solar longitude. The diurnal variation is a factor of about 10-11 for all seasons, which is similar to that in the solar cycle variability discussion.
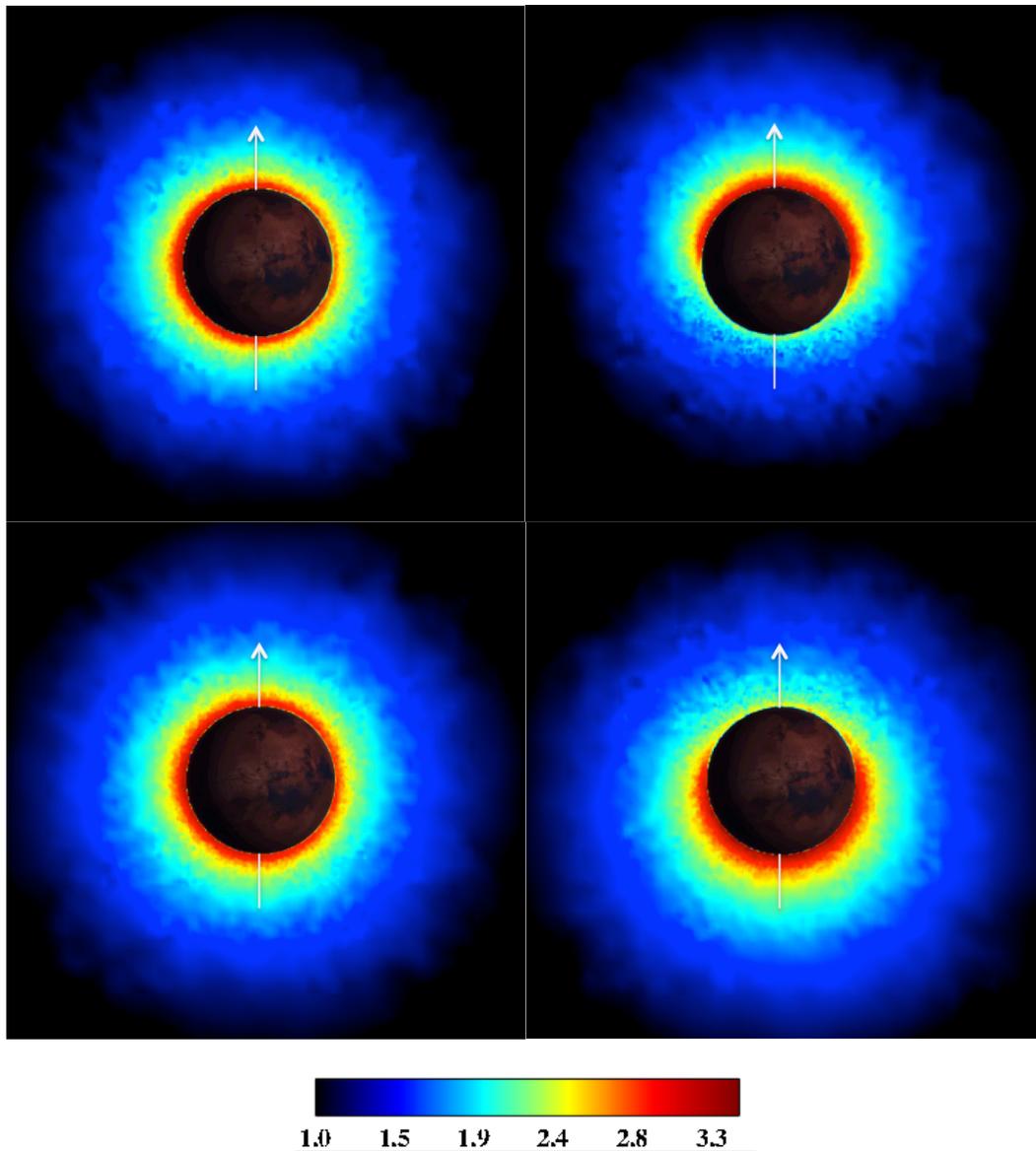
Figure 8.11. The simulated hot O densities, from the top left figure in clockwise direction, for the VEQUMIN, APHMIN, AEQUMIN, and PERMIN cases. The plane shown is the dawn-dusk plane. The color contours indicates the logarithm of density (cm^{-3}).

Figure 8.11 shows the dawn-dusk plane of the hot O corona to illustrate the seasonal variation from a different perspective. It is easy to see the strong dependency of the spatial features of hot O on the source distribution when viewed in the dawn-dusk plane. For example, the seasonal variability of the hot O corona is apparent from the shift of the envelopes of the hot

corona toward the North and South Poles at aphelion and perihelion, respectively. Moreover, the two equinox cases show slightly different hot O production between the two terminators.

VIII.3.3. Density profiles and escape probability variation

The density profiles are extracted at SZA 60° on the Northern hemisphere along the meridian from the 3D simulations for the AEQUMIN, AEQUMED, and AEQUMAX cases to represent the solar cycle variability and the APHMIN and PERMAX to represent the extreme cases in the combination of solar cycle and season. Figure 8.12 shows the density profiles for different solar conditions. For all thee solar activity cases, the simulated hot O densities peak at an altitude of ~180 km, which does not vary significantly from low to high solar activity. The peak altitude is rather related to the spatial location, where the increase of peak altitude is about 10 km. The peak densities are ~2.3×10^3 cm^{-3}, 3.8×10^3 cm^{-3}, and 5.0×10^3 cm^{-3} for the low, moderate and high solar activity cases, respectively, showing the enhancement of density by a factor of about 2 from low to high solar activity.

As mentioned previously, the seasonal variation in the hot O density (8.12b) is not significant. Since the heliocentric distance varies throughout a whole Martian year, it is logical to expect that the simulated hot O density is the lowest for the aphelion case, while the perihelion case shows the highest density for the altitude range considered. The hot O densities during both northern spring and fall seasons are similar, but show a slightly larger hot O density in autumnal equinox. The difference between the vernal and autumnal equinox cases is obvious, since the temperature and winds are slightly different. The peak altitude of hot O is ~180 km altitude, and the peak densities are ~2.0×10^3 cm^{-3}, 2.3×10^3 cm^{-3}, 1.8×10^3 cm^{-3}, and 3.0×10^3 cm^{-3} for the

VEQUMIN, AEQUMIN, APHMIN, and PERMIN cases, respectively. The overall hot O density

increases by a factor of ~1.6 during the seasons from aphelion to perihelion.
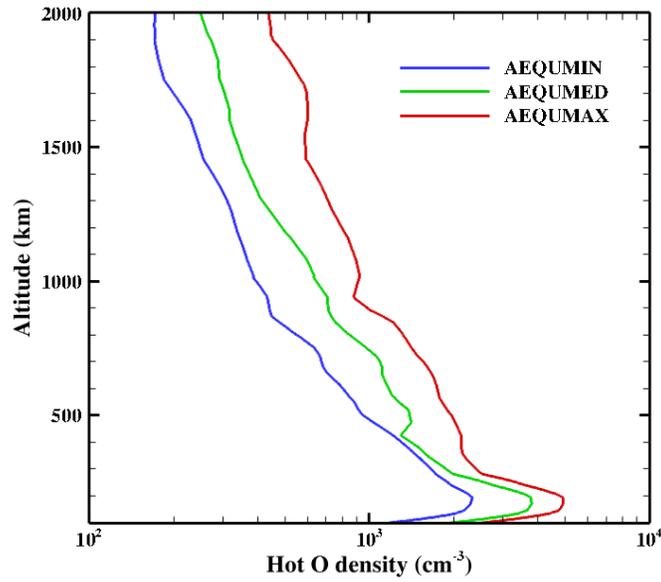
(a)
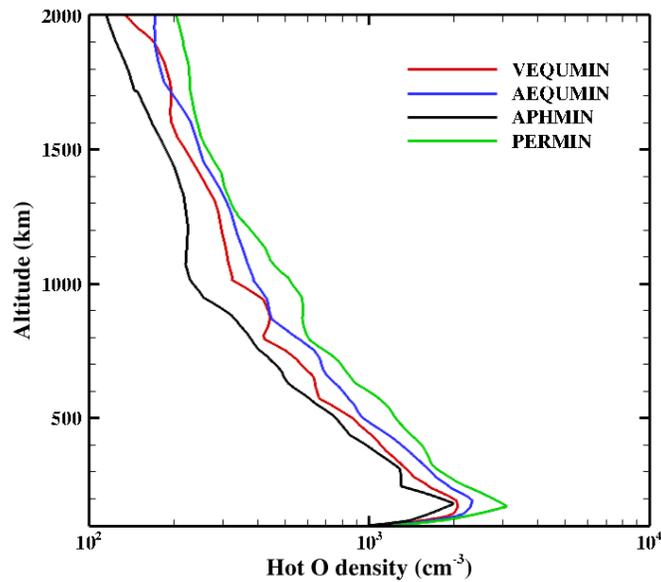
(b)

Figure 8.12. The extracted hot O profiles at SZA 60° on the Northern hemisphere along the meridian for (a) the AEQUMIN, AEQUMED and AEQUMAX cases; (b) the VEQUMIN, AEQUMIN, APHMIN, and PERMIN cases.

Here, the escape probabilities for all solar cycle and seasonal variations are computed. The computed escape probabilities are displayed as a function of the log of atmospheric pressure in units of dyne cm^{-2} to remove the effect of the expansion of the atmosphere due to the variable solar flux. The escape probabilities from all cases begin to converge to 0.5 above an altitude where the log pressures for two extrema cases are ~2.3 × 10^{-6} for APHMIN and ~4.7 × 10^{-6} for PERMAX, which correspond to a range of altitudes as shown in the altitude reference plot (figure 8.13b) - ~185 km (APHMIN) – 249 km (PERMAX). Unlike in the density of hot corona, escape probability is more affected by heliocentric distance than by the solar EUV fluxes. The seasonal variation is illustrated by different colors in figure 8.13. The groups of the same colors indicates that the seasonal variability of the hot O corona is characterized by a different thermospheric/ionospheric structure, which results in the deviation of the probability curves below the base of the exosphere. The atmospheric pressure in the lower atmosphere for the maximum condition (*i.e.,* perihelion and high solar activity) is the highest among all solar or seasonal conditions. Indeed, the computed probabilities are about an order of magnitude smaller than the minimum condition (*i.e.,* aphelion and low solar activity) at lower altitudes and converge to 0.5 quickly with increasing altitude. Although the production rates of hot O are much higher in the high solar activity case, the escape probabilities are found to be lower than those of other lower solar activity cases.
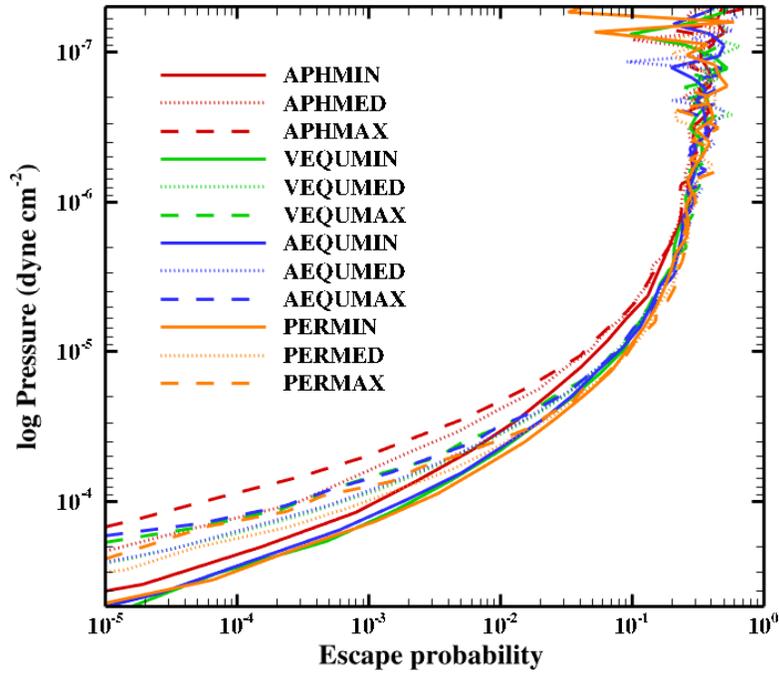
(a)
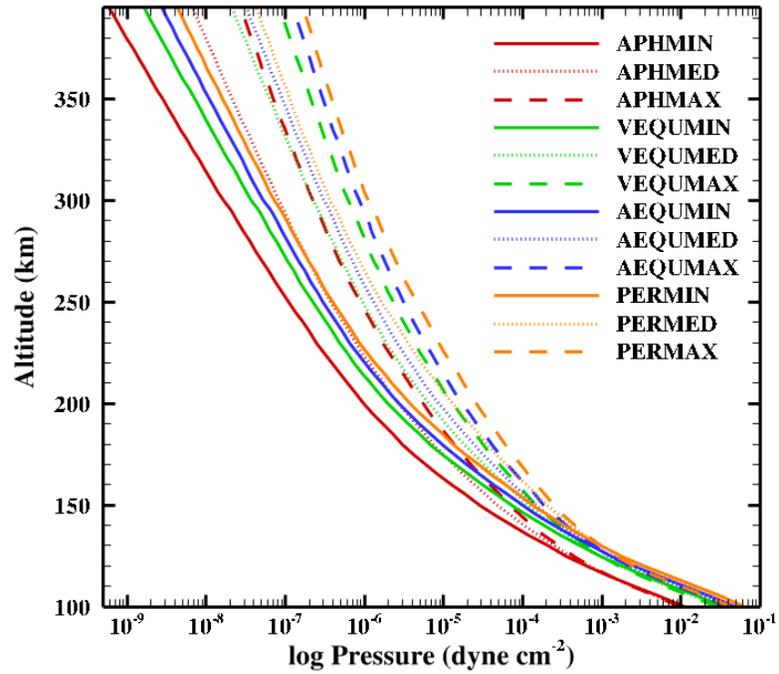
(b)

Figure 8.13. (a) The computed escape probability of hot O and (b) altitude reference plot for all solar cycle and seasonal cases.

VIII.3.4. Global escape rates and model comparison

The computed global escape rates from all 12 cases are shown in table 8.5. The smallest and largest escape rates are achieved by the aphelion and low solar activity case and the perihelion and high solar activity case, respectively. Due to the larger atmospheric temperature and source densities, the escape rates at autumnal equinox are not much similar, and the difference is even slightly larger at high solar activity. The zonal and meridional winds at autumnal equinox are slightly faster than at vernal equinox, resulting in a stronger horizontal atmospheric flow. The effect of this enhanced horizontal flow is combined with larger vertical wind whose velocity is about 3 – 4 times larger than that at vernal equinox. As a result, the background temperature is warmer at autumnal equinox due to stronger downwelling and converging flow. Moreover, the enhanced source densities of hot species induce more production than the vernal equinox case. The resulting escape rates at autumnal equinox for all three solar activity cases are ~23 – 33% larger than those at vernal equinox.

The solar cycle variability of the modeled hot O corona is represented by the global escape variation with the change in solar activity. The solar cycle variation of escape rate is more or less consistent throughout a Martian year, which is a factor of ~2.2 – 2.9 increase with increasing solar activity. The seasonal variability is characterized as much smaller variation in escape rate than the solar cycle variability. The average variation is a factor of ~1.2, and the variation between extreme seasons, aphelion and perihelion, is a factor of ~1.5.

Escape rate $(10^{25}\ s^{-1})$	Aphelion $(L_s = 90°)$	Vernal Equinox $(L_s = 0°)$	Autumnal Equinox $(L_s = 180°)$	Perihelion $(L_s = 270°)$
Solar Minimum	1.14	1.30	1.61	1.74
Solar Moderate	1.82	2.03	2.50	3.29
Solar Maximum	2.71	2.87	3.83	5.18

Table 8.5. Computed escape rates for all solar activity and seasonal cases considered.

The loss of O from the Martian atmosphere has been investigated by a number of studies using various numerical schemes and assumptions. The escape rates from the previous models that carried out the Monte Carlo calculations for the low and high solar activity cases are shown in table 8.6. The some model estimations are substantially larger or smaller than other models, and it is more or less difficult to identify the cause of the difference. Some previous models often do not provide the detailed descriptions about their models, such as the assumptions in the model atmosphere and information about the model parameters, making a direct comparison problematic. Although various approaches have improved our understanding about the Martian atmospheric loss, more information about models will allow more precise model comparisons.

Models	Low solar activity	High solar activity	Thermosphere/Ionosphere model
Hodges [2000][a]	2.8		1D; *Kim et al.* [1998]
Hodges [2002][b]	4.4	18	1D; *Kim et al.* [1998]
Krestyanikova and Shematovich [2005][c]	0.13	3.4	1D; *Kim et al.* [1998]
Krestyanikova and Shematovich [2005][d]	9.9	150	1D; *Kim et al.* [1998]
Krestyanikova and Shematovich [2005][e]	1.3	22	1D; *Kim et al.* [1998]
Krestyanikova and Shematovich [2006][f]	0.33		1D; *Kim et al.* [1998]
Krestyanikova and Shematovich [2006][g]	0.45		1D; *Kim et al.* [1998]
Cipriani et al. [2007]	2.1	5.0	1D; *Kim et al.* [1998]
Chaufray et al. [2007]	1.0	4.0	1D; *Krasnopolsky* [2002]
Valeille et al. [2009][h]	6.0	19	3D; MTGCM
Fox and Hać [2009][i]	0.71	0.63	1D
Fox and Hać [2009][j]	14.4	21	1D
Yagi et al. [2012][k]	4.7		3D; LMD-MGCM
Fox and Hać [2014][l]	0.65	1.6	1D
This study[m]	1.6	3.8	3D; M-GITM

Table 8.6. Summary of the various model calculations of O loss rate (10^{25} s^{-1}) for low and high solar activities.

[a] Mars-L case

[b] Account for collisional quenching and excitation transfer of O(^{1}D) and O(^{1}S); day-only ionosphere case.

[c] Isotropic solid sphere collisions.

[d] Model A case; differential scattering cross section for elastic channels only.

[e] Model B case; differential scattering cross section for elastic and inelastic channels; includes the excitation of rotational-vibrational levels of the CO_2 molecule.

[f] Model A case; elastic and inelastic channels; without quenching O-O and O-CO_2 collisions; includes the excitation of rotational-vibrational levels of the CO_2 molecule.

[g] Model B case; elastic and inelastic channels; without quenching O-O and O-CO_2 collisions.

[h] Atmospheric input is the MTGCM (full 3D thermosphere/ionosphere model).

[i] Eroded ionosphere and isotropic case; assumes that O escape flux at SZA 60° is average over the dayside.

[j] Eroded ionosphere and forward scattering case; assumes that O escape flux at SZA 60° is the average over the dayside.

[k] Four different seasons at average solar condition are considered.

[l] Model 1, eroded.

[m] Four background species as neutral collision partners / forward scattering / differential scattering cross section by *Kharchenko et al.* [2000].

According to table 8.6, at low solar activity, the computed global O escape rate from the model show good agreement with the results from *Hodges* [2000][a], *Krestyanikova and Shematovich* [2005][e], *Cipriani et al.* [2007], *Chaufray et al.* [2007], and *Fox and Haċ* [2009][I], where the difference is within a factor of 2. *Fox and Haċ* [2014][l] examined the sensitivity to the elastic cross sections by adopting different cross sections for hot O with five different background species. Their estimated escape rate for the model that is close to the model setting is a factor of about 2.4 lower than this study's value. The escape rates estimated by "Mars-L" model in *Hodges* [2002] and the LMD-MGCM in *Yagi et al.* [2012] are about 3 times larger than the rate calculated in this study, and the previous model, *Valeille et al.* [2009][h], estimated the rate about ~3.7 times higher than the current model's value. The difference between the results from this study and *Valeille et al.* [2009][h] may be largely due to the different scattering scheme (isotropic scattering in *Valeille et al.* [2009][h]) and the number of the ambient thermospheric constituents. The isotropic solid sphere collision approximation case in *Krestyanikova and Shematovich* [2005][c] and model A and B in *Krestyanikova and Shematovich* [2006][f,g] found the escape rates only about ~10 − 30% of this study's value. The models utilized the forward scattering with differential scattering cross section, *Krestyanikova and Shematovich* [2005][d] and *Fox and Haċ* [2009][j] resulted in the escape rates a factor of ~6 and 9 larger than this study's value.

At high solar activity, the calculations by *Krestyanikova and Shematovich* [2005][c], *Cipriani et al.* [2007], and *Chaufray et al.* [2007] are in good agreement with this work's calculation for the high solar activity case. However, the rest of the models that also computed for the high solar activity case shows a larger ratio between low and high solar activities, except for that of *Fox and Haċ* [2009][i] and *Fox and Haċ* [2014][l] than that of this study. It is difficult to

197

directly compare model by model due to the lack of the detailed model information, but it is clear that the main factor may be the consideration of CO and N_2 as additional background atmospheric constituents.

VIII.3.5. Correlation between the density at a certain altitude (~200 km) and escape rates

As will be discussed in details later in chapter 9, MAVEN will measure the densities of hot and cold neutral atoms, not the global escape rates of neutral species. The escape rates will be estimated by numerical models by using the *in situ* measurements of the thermospheric and ionospheric density from MAVEN. In search of seeking a convenient reference tool for a 3D model, this section explores the relation between the density at a certain altitude (~200 km) and escape rates for the solar and seasonal cases considered.

The 12 cases of M-GITM atmospheric inputs consist of a full range of solar activity and a Martian year by taking advantage of variable model parameters – F10.7 index (at Earth) and the solar longitude of Mars (L_s). This full coverage of solar activity levels and seasons allows the examination of any relations between the hot O density near the base of the exosphere and the corresponding global escape rates. Table 8.7 shows the SZA 60° hot O density at an altitude of 200 km and the corresponding integrated global escape rates for all 12 cases considered for this study.

M-GITM cases	Hot O density at 200 km (10^3 cm^{-3})	Escape rate (10^{25} s^{-1})
Vernal equinox ($L_s = 0°$)		
VEQUMIN	2.0	1.30
VEQUMED	2.8	2.03
VEQUMAX	4.2	2.87
Aphelion ($L_s = 90°$)		
APHMIN	1.8	1.14
APHMED	2.9	1.82
APHMAX	3.9	2.71
Autumnal equinox ($L_s = 180°$)		
AEQUMIN	2.3	1.61
AEQUMED	3.7	2.50
AEQUMAX	4.8	3.82
Perihelion ($L_s = 270°$)		
PERMIN	2.8	1.72
PERMED	3.6	3.29
PERMAX	5.0	5.18

Table 8.7. Relationship between the hot O density at 200 km altitude and corresponding global escape rate.

In figure 8.14a, the density and global escape rate of O are plotted together for three solar activities (*i.e.,* low, moderate, and high). Each solar activity case is represented with different color and is described by the corresponding solar activity case at each seasonal case. For example, the first and second data points in the red curve indicate the aphelion / low solar activity and vernal equinox / low solar activity cases, respectively. The density and escape rate increase with increasing solar activity, resulting in three separate curves with similar increasing trends. The magnitude of the density and escape rate is larger with increasing solar activity, and the seasonal variation trend is similar for different solar activities.

Figure 8.14b illustrates the seasonal trends in the simulated hot O densities and escape rates. The three data points in each seasonal case represent the low, moderate, and high solar activities at that season. These curves describe the variation of the estimated escape rates and hot O density (at 200 km altitude) from solar low to high in the model. Likewise, the slopes of four seasonal cases show good agreement with that of one another. Compared to the curves in figure 8.14a, this family of seasonal curves also shows the similar increasing trend with increasing solar activity. The small seasonal variation of the magnitudes of the densities and escape rates over seasons is evident in the overlaps of the curves for the lower densities. Overall, the computed global escape rates of O show some correlations with the simulated hot O densities at 200 km altitude, as in the case of figure 8.14a.
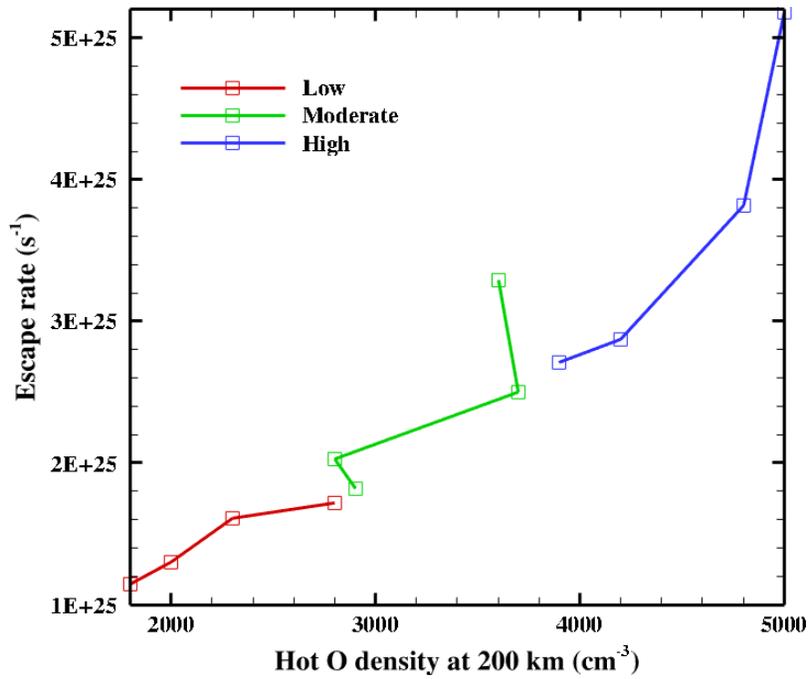
(a)
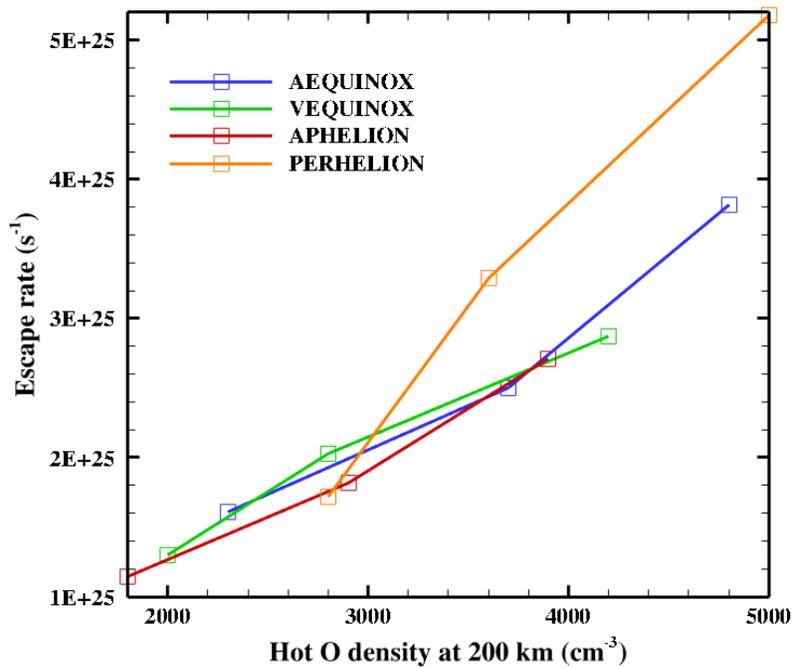
(b)

Figure 8.14. Family of curves that represent the hot O densities at 200 km and corresponding global escape rates for (a) three solar activities and (b) four seasonal cases. In the line legend in (b), AEQUINOX, VEQUINOX, APHELION, and PERHELION correspond to autumnal equinox, vernal equinox, aphelion, and perihelion.

VIII.4. Comparison with observation

Rosetta mission, the European Space Agency's 'comet chaser,' made an observation of the Martian hot oxygen corona during its gravity assist swing-by of Mars on 25th of February 2007. The ALICE instrument on board the *Rosetta* spacecraft, a far-ultraviolet (FUV) imaging spectrograph, detected 1304Å atomic oxygen emission for the altitude range of 400 km – 1000 km during the spacecraft's closest approach. The Martian exospheric atomic oxygen at such high altitudes was first observed above the limb during the limb scan mode of the spacecraft.
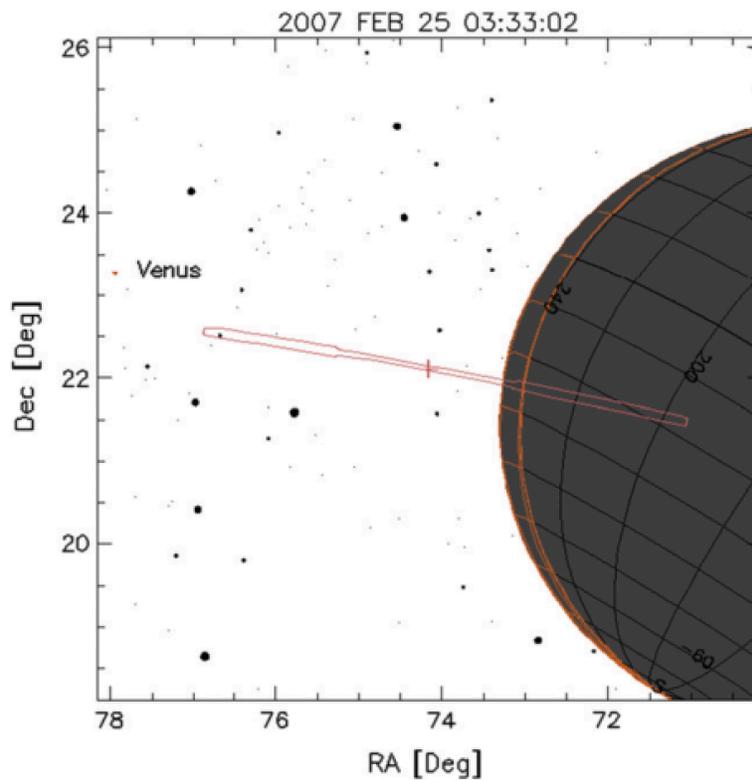
Figure 8.15. Projection of the ALICE slit and geometry of the observation site. The boresight is indicated by +. This is figure 2 in *Feldman et al.* [2011].

Figure 8.15 shows the observation geometry from the spacecraft's observational view. Projection of the ALICE instrument slit is shown in orange solid line, which is extended radially

above the limb of Mars. At the time of observation, solar minimum (F10.7 $\approx$ 72 measured at Earth) condition was observed at Earth, and the northern hemisphere of Mars was close to autumnal equinox season (L_s = 189.9°), locating at a distance of 1.445 AU from Sun. The configuration of the observation closely matches the low solar activity and autumnal equinox case in the model simulation – EL case in MTGCM and AEQUMIN case in M-GITM.

The geometry of the observation site is shown within the computational domain in figure 8.16. The trajectory of the spacecraft during the observation period was acquired from the SPICE kernels of ALICE/*Rosetta*. The line of sight shows the path of integration of oxygen density for the computation of the exospheric oxygen brightness. Since the look direction of the ALICE instrument points toward the dayside from the nightside of Mars, the instrument could observe the extended dayside hot O corona.

The tangent point of ALICE observations at the limb is determined by finding a point on the line of the instrument's sight, which is the closest to the surface of Mars. The resulting tangent point is situated at latitude and solar zenith angle of about -26.5° and 67.9°, respectively, matching the observational parameters (table 1 in *Feldman et al.* [2011]). To compare with the observed OI 1304Å brightness, several altitude points, which are radial to the tangent point, are chosen to calculate the oxygen brightness from the simulated hot O corona and cold background O thermosphere.
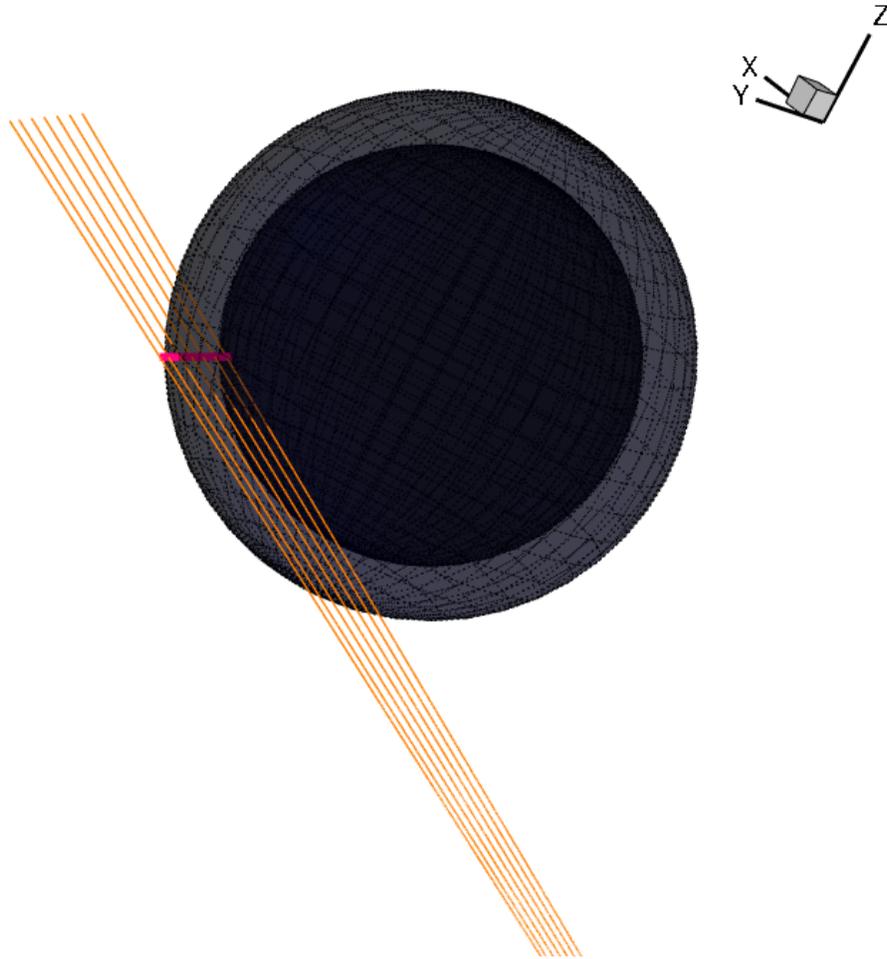
Figure 8.16. Geometry of the line of sight for the computation of OI brightness. The orange solid lines represents the lines of sight, and the pink vertical line indicates the altitude range of the observation. The black shaded sphere corresponds to Mars. The x-axis point towards the Sun, and z-axis is the rotational axis of Mars. The y-axis completes the right-hand rule.

VIII.4.1. Previous studies

According to their observation paper, *Feldman et al.* [2011] analyzed their OI 1304 Å profile by adapting a two-component oxygen model. They took 200 K and 1200 K as the scale height temperatures of the cold and hot component with oxygen densities of 3.0×10^7 cm^{-3} and 1.0×10^5 cm^{-3} at 200 km altitude, respectively. They found that their oxygen model displayed a faster decreasing trend in density at high altitudes than other recently published model results

[*Chaufray et al.*, 2009; *Valeille et al.* 2009a, 2009b, 2010a]. Figure 8.17 shows the extracted OI 1304Å brightness with their two-component oxygen model calculation as a function of altitude above the limb of Mars. There are only four data points available for model comparison, and the statistical uncertainty (horizontal bars) in the count rate is quite large above an altitude of 1000 km.
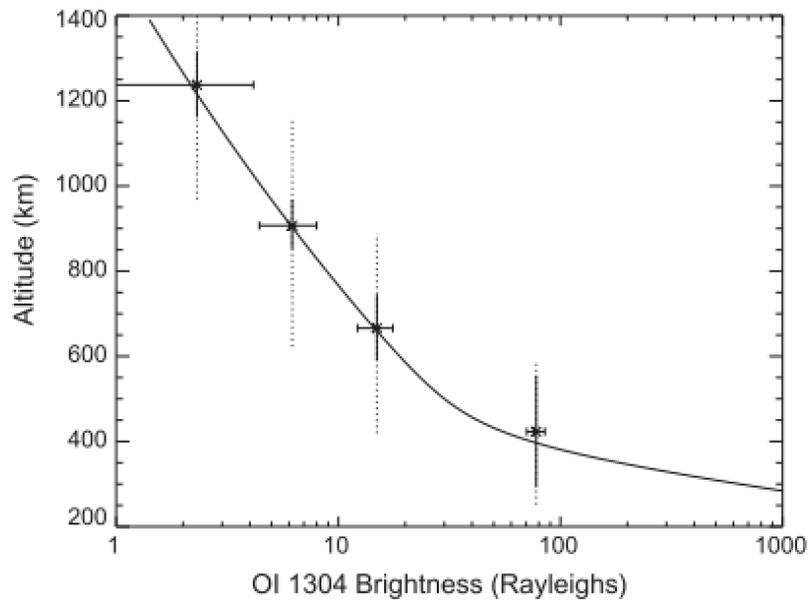
Figure 8.17. OI 1304Å brightness measurements (4 data points) and the two-component oxygen model. This is figure 8 in *Feldman et al.,* [2011].

Recently, *Yagi et al.* [2012] have compared their model calculation of OI 1304Å brightness with the ALICE/*Rosetta* observations [*Feldman et al.,* 2011] and model calculations of *Feldman et al.* [2011]. *Yagi et al.* [2012] reported that their calculated density profile corresponds well to the two-component model of *Feldman et al.* [2011]. Their reconstructed OI 1304Å brightness showed a reasonable agreement with the observations by taking into account the large statistical uncertainties in the count rate. The thermosphere in the calculation by *Yagi et*

al. [2012] is described by the LMD-MGCM. Their exosphere model is built for average solar condition, which is used to simulate the seasonal variation of O density. Although the solar condition during the observation was close to low solar activity at equinox, the model by *Yagi et al.* [2012] uses their average solar condition atmosphere for the calculation, and the results show good agreement with the observations. The dotted grey curves shown in both figures 8.18a and 8.18b indicate their three different approaches using various slit sizes. Our results shown in the next section comparing the model hot O distribution for different solar conditions imply that, had *Yagi et al.* [2012] actually used the appropriate solar minimum condition, their comparison with the observations would not have shown good agreement.

VIII.4.2. Comparison and discussion

The hot O corona in this study is simulated with appropriate background thermospheric / ionospheric and kinetic parameters and solar activity conditions in order to describe as similar as atmospheric condition at the time of the spacecraft's fly-by of Mars as possible. First, the spacecraft's trajectory is mapped together with the simulated Martian hot O corona, using the SPICE kernels obtained from Planetary Data System (http://pdssbn.astro.umd.edu/). The model configures the instrument's line-of-sight and executes line integrations of the simulated local density along the path. The local number density of total oxygen (hot O + cold O) is converted to the local column density and multiplied by the *g-factor* or emission rate per molecule to determine the brightness of OI 1304Å emission line.

Although the solar and seasonal condition during the observation was close to the autumnal equinox and low solar activity case in the model, which is pre-simulated by M-GITM by adjusting the solar and orbital parameters within the model, the OI 1304Å brightness for

several other different model atmosphere conditions is also computed to examine the difference between the observation and the model results. Utilizing the analysis of the model parameters in previous sections, (1) the case with the vibrational levels of O_2^+ added, (2) the case with the branching ratio dependency on altitude, (3) forward and isotropic scattering, and (4) different number of the background neutral species (see also table 8.8) are considered.

Both (1) and (2) assume the forward scattering and only O and CO_2 as the background species. (1) and (2) are described by the FW2BG-vib (solid purple) and FW2BG-vib-BR (solid green) cases as shown in figure 8.18a. The case that considers only the ground state of O_2^+ is shown together as the FW2BG (solid grey) case. Apparently, it is difficult to find any difference in the results with the different treatments for O_2^+. (1) and (2) may show a difference in the energy distribution of nascent O, but their effects on the simulated macroscopic values are not significant.

(3) is investigated by the FW2BG (solid grey) and HS2BG (solid orange) cases in figure 8.18a. The controlled parameters for this comparison is the number of the background species, which is chosen as 2 (O and CO_2). (3) comparison shows the largest difference in the computed OI 1304Å brightness. Since the intensity of the O density is correlated to the available O density at that site, it is expected that the brightness for the isotropic case is the lowest of all. The brightness in the isotropic scattering case is lower by a factor of ~3 at ~1000 km altitude.
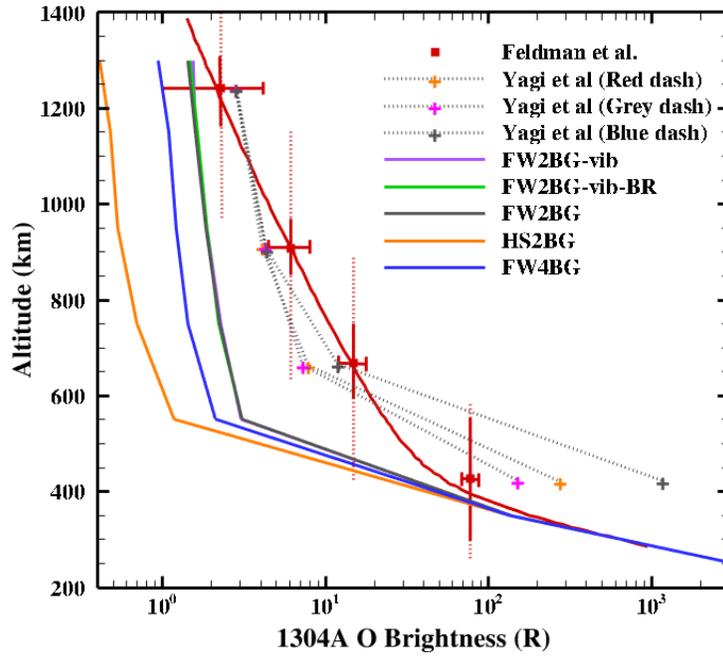
(a)
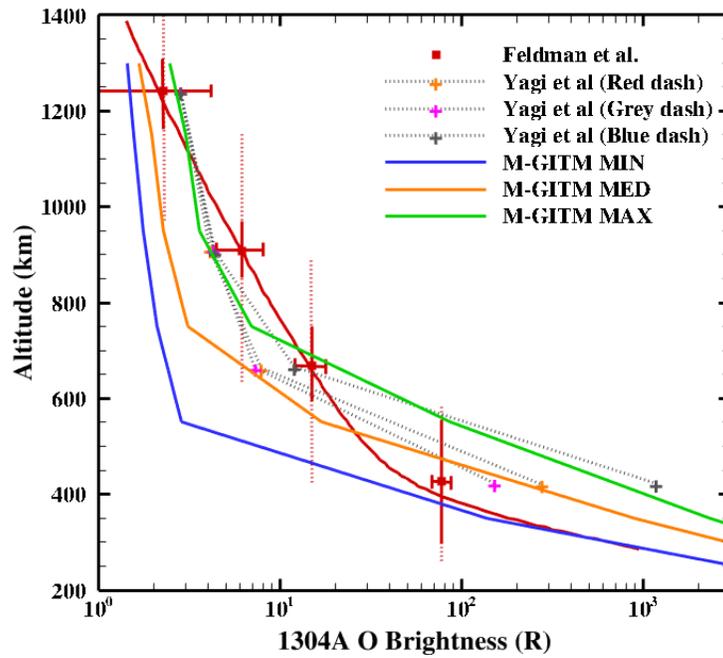
(b)

Figure 8.18. Comparisons between the ALICE measurements and the brightness computed from the simulated hot O corona for (a) various cases using different model parameters and (b) different solar activities. The red vertical (both dotted and solid) and horizontal bars indicate the extent of trapezoidal altitude weighting function for each row and the statistical uncertainty in the count rate, respectively.

208

(4) corresponds to the FW2BG (solid grey) and FW4BG (solid blue) cases. The collision type is kept as the forward scattering assumption, and the only varied parameter is the number of the background neutrals. By adding two more neutrals (*i.e.,* CO and N_2) as the collision partners of hot O, it is logical to see more thermalization of O and less escape of O. As a consequence, there are less O density available in the exosphere and lower OI 1304Å brightness by a factor of ~1.5 at ~1000 km altitude.

The detected OI (1304 nm) brightness from limb scans has been compared with the all the cases considered above and some additional cases. From the above comparisons, the best set of model parameters that corresponds well to the observation is the forward scattering assumption with O and CO_2 only as the background neutrals and the assumption of the vibrational ground state of O_2^+. The observation is shown as a red solid curve and 4 data points derived by *Feldman et al.* [2011]. In figure 8.18a, all those cases that examined the model parameters are simulated at autumnal and low solar activity. In the lower atmosphere where the thermal O density surpasses that of hot O, the computed brightness shows great agreement with the observation. However, as hot O becomes a dominant species with increasing altitude, the computed brightness for all cases are far apart from the observation. This separation becomes converged at higher altitudes, and the computed brightness shows good agreement with the observation again. The slopes of the brightness curves corresponding to the region where hot O is dominant (> ~550 km) from the model are very different from the observation. In order to test the cases with more hot O production, three different solar flux cases have also been examined: low, moderate, and high solar activities as shown in figure 8.18b. The brightness of OI becomes larger as the solar fluxes increase from F10.7 = 70 to 200. More hot O production results in a larger O brightness. The solid green curve, which is the high solar activity case, shows the best

agreement with observation above an altitude of ~650 km, where the low solar activity case show a factor of ~10 less brightness. However, since the real solar condition during the observation was at low solar activity, it is not correct to use a different solar activity case. Despite the good agreement between the high solar activity case and the observation, there is a large discrepancy at lower altitudes. As mentioned earlier, *Yagi et al.* [2012] used the moderate solar condition instead of the more appropriate low solar condition. The three approaches by *Yagi et al.* [2012] found to overestimate the brightness below an altitude of ~600 km and exhibit similar slopes at higher altitudes, which are found in the model results. In order to improve the agreement of the hot O model with any data set, it is likely necessary to improve the description of the source mechanisms and background atmosphere (*i.e.,* scattering environment) in M-GITM first.

Chapter IX

Future work

The development of the model has been accelerated since the time when this thesis began. This thesis explored the 3D nature of the Martian hot heavy atomic coronae and its global loss rate to space at current epoch for a range of different conditions. As a next step, this chapter introduces a number of topics that need to be investigated utilizing our model.

IX.1. Cold and hot hydrogen

The Martian hydrogen corona was observed for the first time by the UV spectrometer onboard Mariner 6,7, and 9 flyby missions [*Barth et al.*, 1969, 1971, and 1972]. The analysis of Lyman-α emission data found that there are two components of the hydrogen population instead of a single cold hydrogen population. More recently, Lyman-α airglow observations were carried out by ASPERA-3 [*Galli et al.,* 2006] and SPICAM [*Chaufray et al.,* 2008] onboard Mars Express. The detected profiles showed that the temperatures of the cold and hot population are ~180 K and ~1000 K at the base of the exosphere. Similar results were also reported by the ALICE UV spectrometer on *Rosetta* [*Feldman et al.,* 2011].

The hydrogen corona is an intriguing subject of study that allows a better understanding of the inventory of water at present epoch. Among the important source mechanisms of hot hydrogen, the reaction,

$$H + O_{hot} \rightarrow O + H_{hot}, \qquad (9.1)$$

describes the energy transfer with hot O from the hot O corona. Recently, interesting studies have been conducted on nonthermal escape of molecular hydrogen, H_2, which is induced by collisions between hot O and molecular hydrogen [*Gacesa et al.,* 2012]. *Matta et* al [2013] found that the composition of the topside ionosphere is very sensitive to molecular hydrogen abundance. Since thermal hydrogen also exists at higher altitudes due to its light mass, it is important to carefully investigate the atomic and molecular hydrogen chemistry in the upper atmosphere. Both source mechanisms mentioned above require a complete 3D description of the hot O corona and thermal H and H_2 distributions. Since the comprehensive hot O corona investigation has been carried out, the hydrogen corona simulation can be conducted if necessary source distributions are available from M-GITM.

IX.2. Hot nitrogen

The Viking 1 and 2 missions have identified that the fractional ratio of atomic ^{15}N over ^{14}N is about 1.62 times the Earth's value [*Nier and McElroy,* 1977]. Mars has lost significant amounts of its nitrogen over geological time by absorbing the solar EUV radiation in the thermosphere and ionosphere and producing hot atomic nitrogen with its energy in excess of the escape energy.

In order to escape to space, a nitrogen atom needs an energy of ~1.73 eV and ~1.86 eV for ^{14}N and ^{15}N, respectively [*Fox and Dalgarno,* 1979]. The proposed main mechanisms that produce the escaping hot N are photodissociation of N_2 [*Brinkmann,* 1971],

$$N_2 + h\upsilon \rightarrow N + N, \tag{9.2}$$

and dissociative recombination of N_2^+ with three exothermic channels [*Wallis,* 1978; *Fox and Dalgarno,* 1983],

$$N_2^+ + e \rightarrow N(^4S) + N(^2D) + 3.44 \text{ eV},$$

$$N_2^+ + e \rightarrow N(^4S) + N(^2P) + 2.24 \text{ eV}, \tag{9.3}$$

$$N_2^+ + e \rightarrow N(^4D) + N(^2D) + 1.06 \text{ eV}.$$
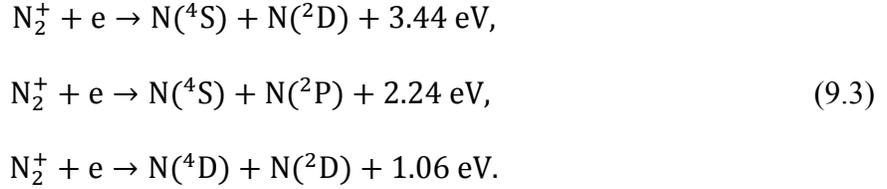
The estimated nonthermal atomic nitrogen escape fluxes by several Monte Carlo models are listed in table 1.1.

IX.3. Two-way coupling of M-GITM/MF-MHD/Mars-AMPS

The 3D Martian hot atomic corona has been simulated and explored via one-way coupling from M-GITM to the Mars exosphere code with Mars-AMPS. Figure 9.2 shows a diagram of the flow of the coupling between models and the exchanging of information. The additional model shown in the diagram is the 3D Multifluid Block Adaptive Tree Solar-wind Roe Upwind Scheme (BATS-R-US) MHD code (MF-MHD), which has been one-way coupled with the MTGCM to investigate the ion escape rate and solar wind interaction with the Martian upper atmosphere [*Dong et al.,* 2014a; *Dong et al.,* 2014b].

The flow denoted by red arrows shows the completed coupled frameworks. M-GITM provides the densities of neutrals and ions, neutral, ion, and electron temperatures, and three components of neutral winds to Mars-AMPS for modeling the hot corona, which is incorporated into MF-MHD, along with cold atmosphere from M-GITM, for the analysis of the Sun-Mars interaction. The remaining arrows in blue will be performed for a complete two-way coupling system. Each model will be implemented into SWMF, where the models can exchange their information simultaneously during the runs. As indicated by the blue arrows, the two-way coupling in SWMF environment will allow a self-consistent description of the mechanisms that require feedback between two models.
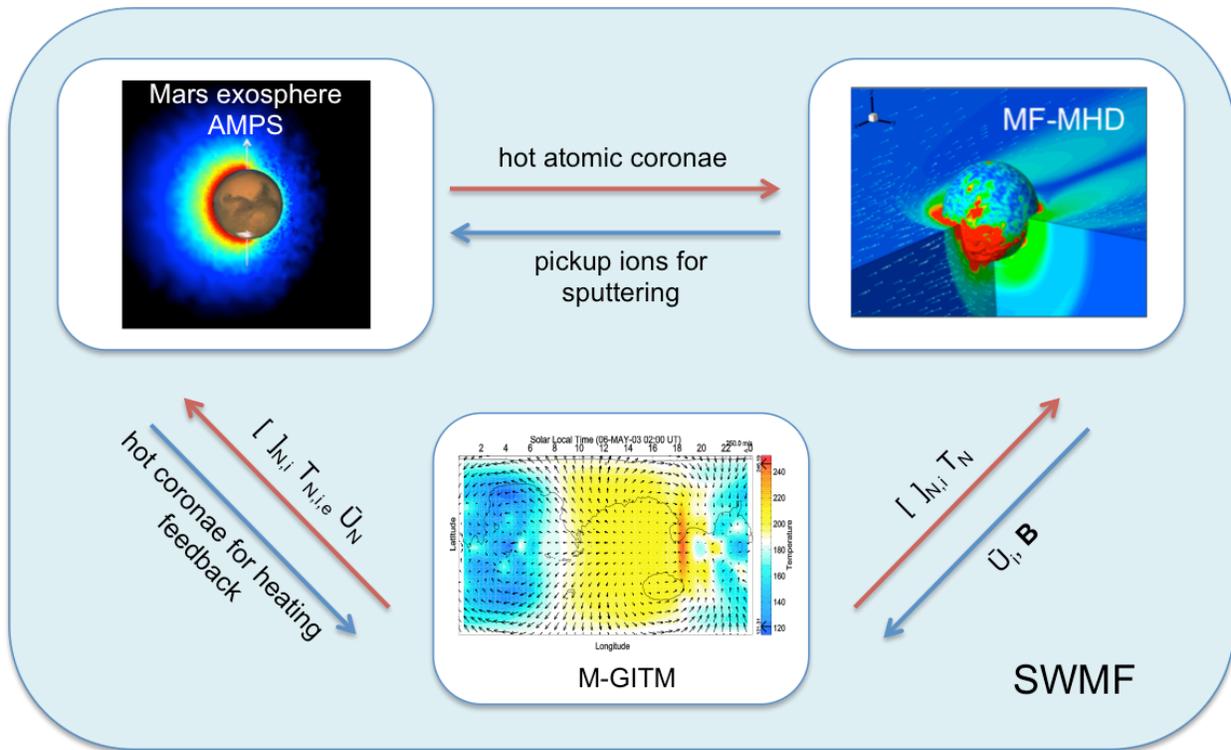
Figure 9.1. Two-way coupling loop integrated into the SWMF for Mars-AMPS, M-GITM [*Bougher et al.,* 2014], and MF-MHD [*Dong et al.,* 2014a; *Dong et al.,* 2014b].

IX.4. Measurements from MAVEN

The Mars Atmosphere and Volatile Evolution mission (MAVEN) is the first Mars mission devoting to understanding the Martian upper atmosphere. It was launched on November 18th, 2013, and is scheduled to arrive at Mars on September 21st, 2014. MAVEN will investigate the planet's thermosphere, ionosphere, exosphere, and interaction with the Sun and solar wind. The goal of the mission is to determine the role that loss of volatiles, such as water and CO_2, to space played in changing the Martian climate through time.

As shown in the diagram in figure 9.2, there are three instrument packages onboard the MAVEN, which include total eight instruments. The mechanisms between the Sun and Mars will be extensively explored by addressing three scientific topics: (1) the current status of the Martian

upper atmosphere structure and composition and the controlling processes, (2) the global escape rate at the present epoch and the relationship with the controlling processes, and (3) the past evolution of the total atmospheric loss to space over geologic time.
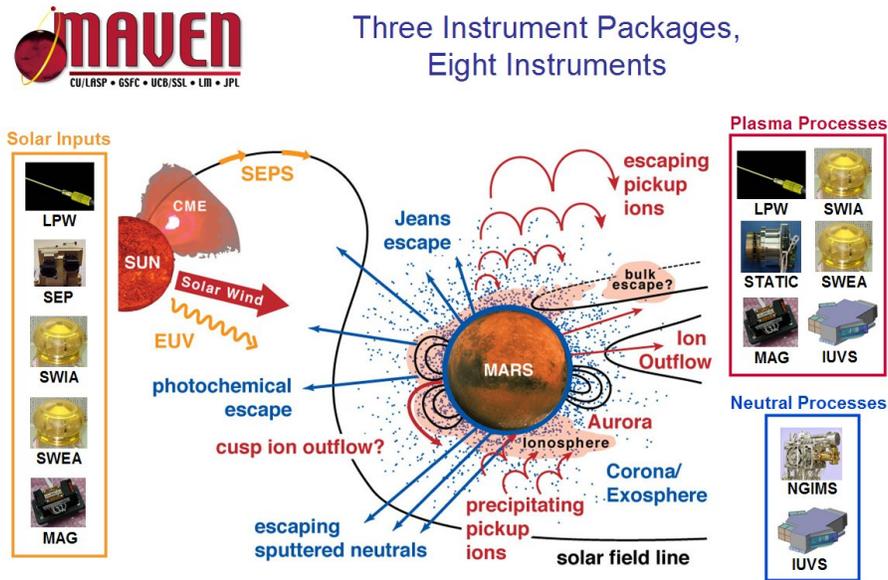
Figure 9.2. Schematic of instrument packages onboard the MAVEN. Various mechanisms between the Sun and Mars are also shown together (http://lasp.colorado.edu/home/maven).

Modeling teams will utilize the data taken by MAVEN and calculate the global atmospheric escape and simulate the evolution of the loss of atmosphere to space. The models will simulate the exosphere and hot corona with the atmospheric condition observed by MAVEN. Our model will participate as a complete 3D simulator in the construction of the coupled model library of the global interactions and provide the most realistic description to the computation of the global atmospheric loss. It is significant to build model libraries since they will function as operational tools for estimating photochemical escape rates and interpreting measurements.

Figure 9.3a shows a sample trajectory of MAVEN for the first complete orbit of the day on November 4th, 2014. It is a 4-sec sampling of the trajectory up to an altitude of ~1000 km. Along this trajectory, the spacecraft moves from the dayside to the nightside crossing the evening terminator near the North Pole. The 3D hot O corona shown together is the simulation from our model for the equinox and low solar activity case. The hot O density can be extracted along this trajectory to compare with observations and estimate the densities in the regions that are not covered by the instruments and the corresponding hot O global escape rate.
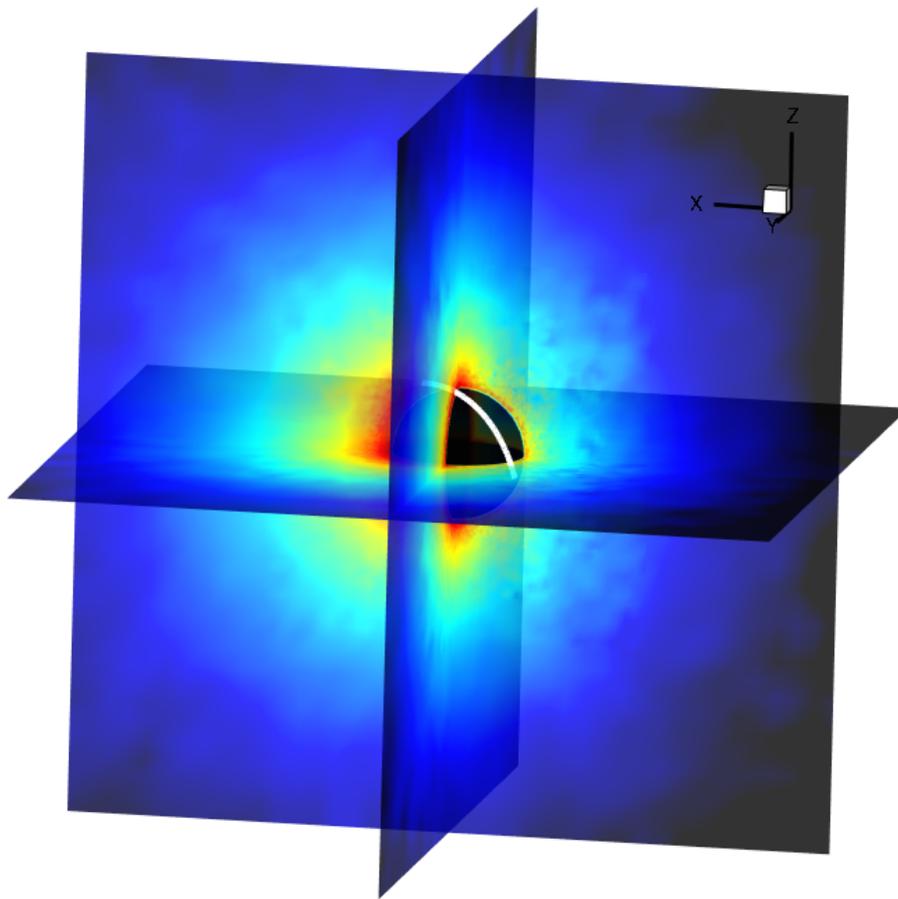
(a)
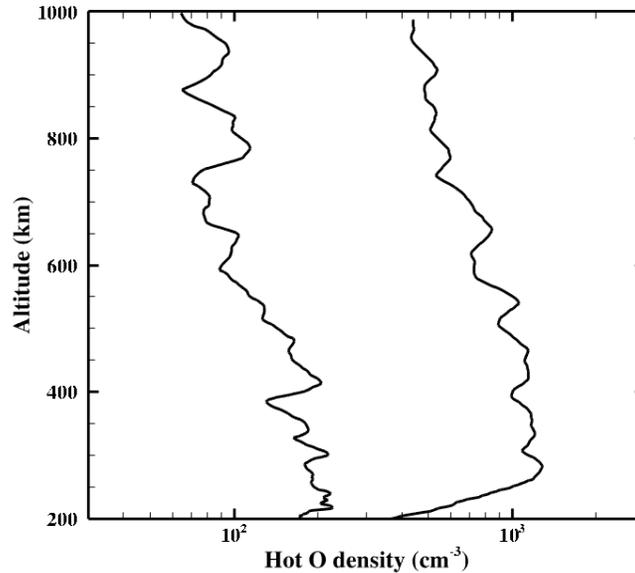
(b)

Figure 9.3. (a) A sample trajectory of the MAVEN for the first complete orbit of the day on November 4th, 2014. A 4-sec sampling of the trajectory, up to an altitude of 1000 km. The trajectory of MAVEN is shown as a white curve extending from the dayside to nightside crossing the evening terminator. The simulation drawn together is the modeled hot O corona for the equinox and low solar activity case. (b) The density of the simulated hot O extracted along the sample trajectory.

The simulated hot O density extracted along the sample trajectory is shown in figure 9.3b. The hot corona simulation will be carried out iteratively by adjusting the model parameters and inputs to model the upper atmosphere as realistically as possible. A flowchart shown in figure 9.4 describes the process from the data to estimation of the global escape rate. Our coupled framework between Mars-AMPS and M-GITM indicated as the process colored as pink, which is a sophisticated 3D investigation but is much slower than other less accurate and simple models. The coupled framework will also provide input to the plasma model to compute the global ion escape rates. Thus, the MAVEN's measurements of the properties and processes will allow the models to estimate the integrated atmospheric loss of both neutrals and ions to space both today and through time.

217
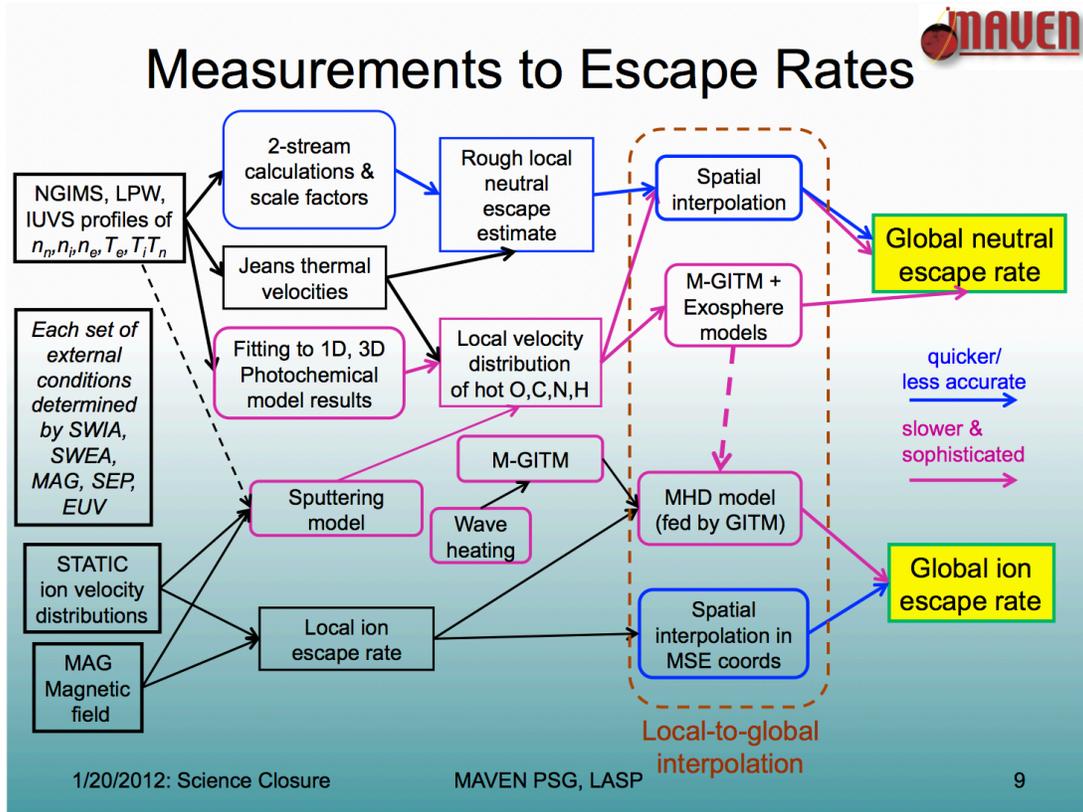
Figure 9.4. A flowchart describing the process from the measurement to escape rate estimation. This is presented as a part of the presentation by Robert Lillis during the MAVEN science community workshop held on December 2nd, 2012.

Chapter X

Conclusion

Investigating the loss of the Martian atmospheric constituents and its mechanisms and variation is key to a better understanding of the current state of the Martian upper atmosphere and the evolution of the water and CO_2 inventories over geologic time. The initial study of the 3D Martian hot corona was completed by *Valeille et al.* [2009a, 2009b, 2010a, 2010b], which successfully finished the first fully 3D implementation of the DSMC code and modeled the hot O corona for various spatial and time scales. Subsequently, the numerical performance of our DSMC code has been significantly enhanced by employing a new adaptive Cartesian mesh with cut cells [*Tenishev et al.,* 2013]. With the newly developed DSMC code, re-named AMPS (3D kinetic particle simulator), this thesis began by implementing a Mars' exosphere model into the AMPS code. The implementation of the exosphere model required the incorporation of all the Mars-related physics and model parameters. In this thesis, the first comprehensive investigation on the Martian hot carbon is carried out by coupling the AMPS code with the Martian exosphere code (Mars-AMPS) and a 3D thermosphere/ionosphere model, MTGCM. The first coupling of Mars-AMPS and a newly developed thermosphere/ionosphere model, M-GITM, is also completed, which greatly improves our past hot oxygen study. This new hot oxygen model has been utilized in preparation for the MAVEN mission for constructing a model library using Mars-AMPS for a complete model parameter study and intercomparison with other models. A

self-consistent 3D global description of the Martian upper thermosphere, ionosphere, and exosphere is provided for studying the variations associated with different solar activities and seasons in the hot atomic coronae from a local to global perspective.

The main advantage of using full 3D thermosphere/ionosphere input is the ability of incorporating the effects of nonaxisymmetric features (*e.g.*, planetary rotation and thermospheric winds), which are inherently absent in other 1D atmospheric models. These 3D features are found to greatly impact the structure of the density profiles of hot species and the shape of the hot atomic corona.

Among the various sources mechanisms, two important mechanisms for hot C are considered, namely photodissociation of CO and dissociative recombination CO^+. For hot O dissociative recombination of O_2^+ is considered to be the major source mechanism in this thesis. The entire set of hot C corona simulations are carried out by using the MTGCM, and hot O corona is simulated using M-GITM, replacing the MTGCM from now on. M-GITM provides a more improved description and solves the previous limitations in the MTGCM.

The density distributions of the thermospheric constituents are more responsive to either the background temperatures or global winds, depending on the mass of the species. For both hot C and hot O corona studies, the effects of the background temperatures and global atmospheric circulation are exhibited in the resulting spatial distributions of hot species. The modeled densities of hot species are distributed with respect to the local production rate and local thermalization rate. These two processes operate as the source and loss of hot atoms, which can be characterized by the combination of local macroscopic parameters from the thermosphere/ionosphere model, such as the local densities of the thermospheric constituents and electron and ion temperatures.

The solar cycle and seasonal dependencies of background temperatures and global winds are large with regard not only to the magnitudes of the local parameters but also to the spatial distributions of the parent molecule and ion of the source reactions. The 3D effects of the background temperatures and global atmospheric circulation are shown as different responses by the thermosphere/ionosphere and allow the implementation of realistic features such as the winter polar warming and the tilted axis effect. The spatial variation of the local thermalization rates due to the local collisional frequencies corresponds to the reasonable distributions and fluxes of hot species for the cases in combination of different solar activities and seasons.

The overall characteristics of the hot corona structure show a strong dependence on the model parameters that represent the micro- and macroscopic processes that determine the energy distribution of hot particles. Various model parameters are examined and employed into the coupled framework. Consequently, the best set of parameters and description of the hot particle mechanics are suggested that the hot O corona simulation needs to include hot O and thermal O collisions using the angular dependence of the differential collision cross section of *Kharchenko et al.* [2000] and consider four cold neutral collision partners in the ambient atmosphere (O, CO_2, CO, and N_2). However, such basic information for hot carbon collisions is not currently available.

The estimated global escape rates of hot carbon atoms range from about 5.2×10^{23} s^{-1} to about 57.1×10^{23} s^{-1} for the aphelion and solar low case and the perihelion and solar high case, respectively. For hot oxygen, the revised global escape rates are estimated to be in the range from about 1.14×10^{25} s^{-1} to about 5.18×10^{25} s^{-1}. The discrepancies between the various published models are difficult to identify because of various different factors including usage of different numerical schemes and the descriptions of background atmosphere and the interaction

between nascent and ambient species. At present, the escape of C due to nonthermal mechanisms plays a slightly more dominant role. However, at earlier epochs, the modeling for the ancient Martian atmosphere is expected to show much more vulnerability to sputtering by solar wind pickup ions than to other processes.

In addition to future work discussed in chapter 9, the entire suite of the hot carbon corona simulation will be carried out with M-GITM. M-GITM is able to provide improved descriptions to the ionospheric peak of CO^+ at high altitudes, where the MTGCM requires extrapolations of CO^+ from below the peak. M-GITM can also include the effects of crustal magnetic fields to the thermosphere and ionosphere. The resulting hot corona from our coupled framework will be investigated to understand the effects of crustal magnetic fields on the hot corona.

Finally, we expect greatly renewed interest in studying the physics of Martian hot coronae in depth with the in situ and remote measurements of the upper atmosphere from the Mars Atmosphere and Volatile EvolutioN (MAVEN) mission, which will shed light on our understanding of the Martian atmosphere.

References

Acuña, M. H., et al. (1998), Magnetic field and plasma observations at Mars: Initial results of the Mars Global Surveyor mission, *Science*, 279, 1676, doi:10.1126/science.279.5357.1676.

Acuña, M. H., G. Kletetschka, and J. E. P. Connerney (2008), "Mars' Crustal Magnetization: A Window into the Past", in The Martian Surface: Composition, Mineralogy, and Physical Properties , ed. J. F. Bell III, Cambridge University Press.

Anderson, D. E. (1974), Mariner 6, 7, and 9 ultraviolet spectrometer experiment: Analysis of hydrogen lyman alpha data, *J. Geophys. Res.,* 79, 10.

Anderson, D. E., and C. W. Hord (1971), Mariner 6 and 7 ultraviolet spectrometer experiment: Analysis of hydrogen lyman-alpha data, *J. Geophys. Res.,* 76, 28.

Ayres, T. (1997), Evolution of the solar ionizing flux, *J. Geophys. Res.,* 102, 1641.

Bakalian, F. (2006), Production of hot nitrogen atoms in the Martian thermosphere, *Icarus*, 183, 69-78, doi:10.1016/j.icarus.2006.02.005.

Barth, C. A. (1969), Planetary ultraviolet spectroscopy, *Appl. Opt.,* 8, 7, doi: 10.1364/AO.8.00129.

Barth, C. A., A. I. Steward, and C. W. Hord (1972), Mariner 9 ultraviolet spectrometer experiment: Mars airglow spectroscopy and variations in lyman alpha, *Icarus,* 17, 457-468.

Barth, C. A., C. W. Hord, J. B. Pearce, K. K. Kelly, G. P. Anderson, and A. I. Stewart (1971), Mariner 6 and 7 ultraviolet spectrometer experiment: Upper atmosphere data, *J. Geophys. Res.,* 76, 10.

Bell, J. M., S. W. Bougher, and J. R. Murphy (2007), Vertical dust mixing and the interannual variations in the Mars thermosphere, *J. Geophys, Res.,* 112, E12002, doi:10.1029/2006JE002856.

Bell, J. M., et al. (2010), Simulating the one-dimensional structure of Titan's upper atmosphere: 1. Formulation of the Titan Global Ionosphere-Thermosphere Model and benchmark simulations, *J. Geophys. Re.,* 115, E12002, doi:10.1029/2010JE003636.

Berger, M. J., and P. Colella (1989), Local adaptive mesh refinement for shock hydrodynamics, *J. Comput. Phys.*, 82, 64-84.

Bird, G. A. (1994), Molecular gas dynamics and the direct simulation of gas flows, Clarendon Press, Oxford.

Bougher, S. W., et al. (2008), Neutral upper atmosphere and ionosphere modeling, *Space Sci. Rev.*, 139, 107-141, doi:10.1007/s11214-008-9401-9.

Bougher, S. W., D. A. Brain, J. L. Fox, F. Gonzalez-Galindo, C. Simon-Wedlund, and P. G. Wither (2014a), Chapter 14: Upper Atmosphere and Ionosphere, In: Haberle, B., M. Smith, T. Clancy, F. Forget, and R. Zurek (Eds.), *Mars Book II*, Cambridge University Press, Accepted.

Bougher, S. W., et al. (2014b), Mars Global Ionosphere Thermosphere Model (M-GITM): Solar cycle, seasonal, and diurnal variations of the upper atmosphere, J. Geophys. Res., Submitted.

Bougher, S. W., J. M. Bell, J. R. Murphy, M. A. López-Valverde, and P. G. Withers (2006), Polar warming in the Mars thermosphere: Seasonal variations owing to changing insolation and dust distributions, *Geophys. Res. Lett.,* 32, doi:10.1029/ 2005GL024059. L02203.

Bougher, S. W., R. E. Dickinson, E. C. Ridley, and R. G. Roble (1988), Venus mesosphere and thermosphere, III, Three-dimensional general circulation with coupled dynamics and composition, *Icarus,* 73, 545-575.

Bougher, S. W., R. G. Roble, E. C. Ridley, and R. E. Dickinson (1990), The Mars Thermosphere 2. General Circulation With Coupled Dynamics and Composition, *J. Geophys. Res.*, 95, 14,811-14,827.

Bougher, S. W., R. G. Roble, and T. J. Fuller-Rowell (2002), Simulations of the upper atmospheres of the terrestrial planets, In: Mendillo, M., A. F. Nagy, and J. H. Waite (Eds.), *Atmospheres in the Solar System: Comparative Aeronomy*, American Geophysical Union, Washington, DC.

Bougher, S. W., S. Engel, R. G. Roble, and B. Foster (1999), Comparative terrestrial planet thermospheres 2. Solar cycle variation of global structure and winds at equinox, *J. Geophys. Res.,* 104, 16,591–16,611.

Bougher, S. W., S. Engel, R. G. Roble, and B. Foster (2000), Comparative terrestrial planet thermospheres. 3. Solar cycle variation of global structure and winds at solstices, *J. Geophys. Res.,* 105, 17,669–17,692.

Bougher, S. W., S. Engle, D. P. Hinson, and J. M. Forbes (2001), Mars Global Surveyor radio science electron density profiles: Neutral atmosphere implications, *Geophys. Res. Lett.,* 28, 3091-3094.

Bougher, S. W., S. Engel, D. P. Hinson, and J. R. Murphy (2004), MGS Radio Science electron density profiles: Interannual variability and implications for the neutral atmosphere, *J. Geophys. Res.,* 109, doi:10.1029/2003JE002154. E03010.

Bougher, S. W., T. M. McDunn, K. A. Zoldak, and J. M. Forbes (2009), Solar cycle variability of Mars dayside exospheric temperatures: Model evaluation of underlying thermal balances, *Geophys. Res. Lett.*, 36, L05201, doi:10.1029/2008GL036376.

Brinkmann, R. T. (1971), Mars: Has nitrogen escaped?, *Science*, 174, 4012, 944-945.

Carr, M. H. (1986), Mars: A water-rich planet?, Icarus, 68, 187-216.

Chamberlain, J. W. (1963), Planetary coronae and atmospheric evaporation, *Planet. Space Sci.,* 11, 901-960.

Chassefiére, E., F. Leblanc, and B. Langlais (2007), The combined effects of escape and magnetic field histories at Mars, *Planet. Space Sci.*, 55, 343-257, doi:10.1016/j.pss.2006.02.003.

Chaufray, J. Y., F. Leblanc, E. Quémerais, and J. L. Bertaux (2009), Martian oxygen density at the exobase deduced from O I 130.4-nm observations by Spectroscopy for the Investigation of the Characteristics of the Atmosphere of Mars on Mars Express, *J. Geophys, Res.,* 114, E02006, doi:10.1029/2008JE003130.

Chaufray, J. Y., J. L. Bertaux, F. Leblanc, and E. Quémerais (2008), Observation of the hydrogen corona with SPICAM on Mars Express, *Icarus*, 195, 598-613.

Chaufray, J. Y., R. Modolo, F. Leblanc, G. Chanteur, R. E. Johnson, and J. G. Luhmann (2007), Mars solar wind interaction: Formation of the Martian corona and atmospheric loss to space, *J. Geophys. Res.,* 112, E09009, doi:10.1029/2007JE002915.

Cipriani, F., F. Leblanc, and J. J. Berthelier (2007), Martian corona: Nonthermal sources of hot heavy species, *J. Geophys. Res.,* 112, doi:10.1029/2006JE002818.E07001.

Cloutier, P. A., and R. E. Daniell, JR. (1979), An electrodynamic model of the solar wind interaction with the ionospheres of Mars and Venus, *Planet. Space Sci.,* 27, 1111-1121.

Combi, M. R. (1996), Time-dependent gas kinetics in tenuous planetary atmosphere: The cometary coma, *Icarus*, 123, 297-226.

Crifo, J. –F., G. A. Loukianov, A. V. Rodionov, and V. V. Zakharov (2005), Direct Monte Carlo and multifluid modeling of the circumnuclear dust coma Spherical grain dynamics revisited, *Icarus*, 176, 192-219, doi:10.1016/j.icrus.2005.01.003.

Curry, S. M., M. Liemohn, X. Fang, Y. Ma, and J. Espley (2013), The influence of production mechanisms on pick-up ion loss at Mars, *J. Geophys, Res.,* 118, 554-569, doi:10.1029/2012JA017665.

Dong, C., S. W. Bougher, Y. Ma, G. Tóth, A. F. Nagy, and D. Najib (2014a), Solar wind interaction with Mars upper atmosphere: Results from the one-way coupling between the multifluid MHD model and the MTGCM model, *Geophys. Res. Lett.,* 41, 2708-2715, doi:10.1002/2014GL059515.

Dong, C., S. W. Bougher, Y. Ma, G. Tóth, Y. Lee, A. F. Nagy, V. Tenishev, D. J. Pawlowski, and M. R. Combi (2014b), Effects of 3-D cold neutral atmosphere and hot corona on the Martian upper atmosphere ion escape, *6th Alfven Conference,* University College London, London, UK, 7-11 July.

Fang, X., et al. (2008), Pickup oxygen ion velocity space and spatial distribution around Mars, *J. Geophys. Res.,* 113, A02210, doi:10.1029/2007JA012736.

Fang X., et al. (2013), The importance of pickup oxygen ion precipitation to the Mars upper atmosphere under extreme solar wind conditions, *Geophys. Res. Lett.,* 40, 1,922-1,927, doi:10.1002/grl.50415.

Feldman, P. D., et al. (2011), Rosetta-Alice observations of exospheric hydrogen and oxygen on Mars, *Icarus*, 214, 394-399, doi:10.1016/j.icarus.2011.06.013.

Fjeldbo, G., W. C. Fjeldbo, and V. R. Eshleman (1966), Model for the atmosphere of Mars based on the Mariner 4 occultation experiment, *J. Geophys. Res.,* 71, 9.

Forbes, J. M., et al. (2002), Nonmigrating tides in the thermosphere of Mars, *J. Geophys. Res.,* 107, 5113, doi:10.1029/2001JE001582.

Forget, F., et al. (2009), Density and temperatures of the upper Martian atmosphere measured by stellar occultations with Mars Express SPICAM, *J. Geophys. Res.*, 114, E01004, doi:10.1029/2008JE003086.

Fougere, N., M. R. Combi, M. Rubin, and V. Tenishev (2013), Modeling the heterogeneous ice and gas coma of Comet 103P/Hartley 2, *Icarus,* 225, 688-702.

Fox, J. L. (1985), The O_2^+ vibrational distribution in the Venusian ionosphere, *Adv. Space Res.,* 5, 9, 165-169.

Fox, J. L. (1986), The vibrational distribution of O_2^+ in the dayside ionosphere, *Planet. Space Sci.,* 34, 12, 1251-1252.

Fox, J. L. (1993), The production and escape of nitrogen atoms on Mars, *J. Geophys. Res.,* 98, 3297-3310.

Fox, J. L. (1997), Upper limits to the outflow of ions at Mars: Implications for atmospheric evolution, *Geophys. Res. Lett.,* 24, 2,901-2,904.

Fox, J. L. (2004), CO_2^+ dissociative recombination: A source of thermal and nonthermal C on Mars, *J. Geophys. Res.,* 109, doi:10.1029/2004JA010514.

Fox, J. L., and A. B. Hać (1997a), The N-15/N-14 isotope fractionation in dissociative recombination of N-2(+), *J. Geophys. Res.,* 104, 24729-24738, doi:10.1029/1999JA900330.

Fox, J. L., and A. B. Hać (1997b), Spectrum of hot O at the exobases of the terrestrial planets, *J. Geophys. Res.*, 102, 24,005-24,011, doi:10.1029/97JA02089.

Fox, J. L., and A. B. Hać (1999), Velocity distributions of C atoms in CO^+ dissociative recombination: Implications for photochemical escape of C from Mars, *J. Geophys. Res.*, 104, 24729-24737, doi:10.1029/1999JA900330.

Fox, J. L., and A. B. Hać (2009), Photochemical escape of oxygen from Mars: A comparison of the exobase approximation to a Monte Carlo method, *Icarus*, 204, 527-544, doi:10.1016/j.icarus.2009.07.005.

Fox, J. L., and A. B. Hać (2014), The escape of O from Mars: Sensitivity to the elastic cross sections, *Icarus,* 228, 375-385, doi:10.1016/j.icarus.2013.10.014.

Fox, J. L., and A. Dalgarno (1979), Ionization, luminosity, and heating of the upper atmosphere of Mars, *J. Geophys, Res.,* 84, A12.

Fox, J. L., and A. Dalgarno (1983), Nitrogen escape from Mars, *J. Geophys. Res.,* 88, A11, 9027-9032.

Fox, J. L., and F. M. Bakalian (2001), Photochemical escape of atomic carbon from Mars, *J. Geophys. Res.,* 106, 28,785-28,795, doi:10.1029/2001JA000108.

Fox, J. L., and J. H. Black (1989), Photodissociation of CO in the thermosphere of Venus, *Geophys. Res. Lett.,* 16, 291-294.

Fox, J. L., and K. E. Yeager (2006), Morphology of the near-terminator Martian ionosphere: A comparison of models and data, *J. Geophys. Res.,* 111, doi:10.1029/2006JA011697.

Fox, J. L., and K. Y. Sung (2001), Solar activity variations of the Venus thermosphere/ionosphere, *J. Geophys. Res.,* 106, 21,305–21,335.

Gacesa, M., P. Zhang, and V. Kharchenko (2012), Non-thermal escape of molecular hydrogen from Mars, *Geophys. Res. Lett.,* 39, L10203, doi:10.1029/2012GK050904.

Galli, A., et al. (2006), The hydrogen exospheric density profile measured with ASPERA-3/NPD, *Space Sci. Rev.,* 126, 447-467, doi:10.1007/s11214-006-9089-7.

Haberle, R. M., et al. (1999), General circulation model simulations of the Mars Pathfinder atmospheric structure investigation/meteorology data, *J. Geophys. Res.,* 104, 8957–8974.

Hagenbuch, K. M., and R. E. Hartle (1969), Simple model for a rotating neutral planetary exosphere, *Phys. Fluids,* 12, 1551, doi:/10.1063/1.1692710.

Hanson, W. B., S. Sanatani, and D. R. Zuccaro (1977), The Martian ionosphere as observed by the Viking Retarding Potential Analyzers, *J. Geophys. Res.*, 82, 28.

Hartle, R. E. (1971), Model for rotating and nonuniform planetary exospheres, *Phys. Fluids,* 14, 2592, doi:10.1063/1/1693379.

Hartle, R. E., and H. G. Mayr (1976), Wind-enhanced escape with application to terrestrial helium, *J. Geophys. Res.,* 81, 7.

Herring, J., and L. Kyle (1961), Density in a planetary exosphere, *J. Geophys. Res.,* 66, 6.

Hinson, D. P., G. L. Tyler, J. L. Hollingsworth, and R. J. Wilson (2001), Radio occultation measurements of forced atmospheric waves on Mars, *J. Geophys. Res.,* 106, 1,463–1,480.

Hochstim, A. R. (1969), Kinetic Processes in Gases and Plasmas, Academic Press, New York.

Hodges, R. R. (2000), Distributions of hot oxygen for Venus and Mars, *J. Geophys. Res.,* 105, 6971-6981.

Hodges, R. R. (2002), The rate of loss of water from mars, *Geophys. Res. Lett.*, 29, 3, 1038, doi:10.1029/2001GL013853.

Huebner, W. F., J. J. Keady, and S. P. Lyon (1992), Solar photo rates for planetary atmospheres and atmospheric pollutants, *Astrophys. Space. Sci.,* 195, 1-294.

Jakosky, B. M. (1991), Mars volatile evolution: Evidence from stable isotopes, *Icarus*, 96, 14-31.

Jakosky, B. M., et al. (1994), Mars atmospheric loss and isotropic fractionation by solar-wind-induced sputtering and photochemical escape, *Icarus*, 111, 271-288.

Jakosky, B. M., and J. H. Jones (1997), The history of Martian volatiles, *Rev. Geophys.,* 35, 1-16.

Jakosky, B. M., and R. J. Phillips (2001), Mars' volatile and climate history, *Nature*, 412, 237-244.

Johnson, R. E. (1994), Plasma-induced sputtering of an atmosphere, *Space Sci. Rev.,* 69, 215-253.

Keating, G. M., et al. (1998), The structure of the upper atmosphere of Mars: In situ accelerometer measurements from Mars Global Surveyor, *Science,* 279, 1672, doi:10.1126/science.279.5357.1672.

Keating, G. M., et al. (2003), Brief review on the results obtained with the MGS and Mars Odyssey 2001 Accelerometer Experiments, paper presented at International Workshop: Mars Atmosphere Modeling and Observations, Inst. de Astrofis. De Andalucia, Granada, Spain, 13 – 15 January.

Kella, D., L. Vejby-Christensen, P. J. Johnson, H. B. Pederson, and L. H. Andersen (1997), The source of green light emission determined from a heavy-ion storage ring experiment, *Science,* 276, 1530, doi:10.1126/science.276.5318.1530.

Kharchenko, V., A. Dalgarno, B. Zygelman, and J. –H. Yee (2000), Energy transfer in collisions of oxygen atoms in the terrestrial atmosphere, *J. Geophys. Res.,* 105, A11, 24,899-24,906.

Kim, J., A. F. Nagy, J. L. Fox, and T. E. Cravens (1998), Solar cycle variability of hot oxygen atoms at Mars, *J. Geophys. Res.,* 103, 29,339–29,342.

Kim, Y. H., and S. Son (2000), The effects of planetary rotation on the exospheric density distributions of the Earth and Mars, *J. Korean Astron. Soc.,* 33, 127-135.

Kliore, A., D. L. Cain, G. S. Levy, V. R. Eshleman, G. Fjeldbo, and F. D. Drake (1965), Occultation experiment: Results of the first direct measurement of Mars's atmosphere and ionosphere, *Science,* 149, 3689, 1243-1248, doi:10.1126/science.149.3689.1243.

Krestyanikova, M. A., and V. I. Shematovich (2005), Stochastic models of hot Planetary and satellite coronas: A photochemical source of hot oxygen in the upper atmosphere of Mars, *Solar Syst. Res.,* 39, 1, 22-32.

Krestyanikova, M. A., and V. I. Shematovich (2006), Stochastic models of hot planetary and satellite coronas: A hot oxygen corona of Mars, *Solar Syst. Res.,* 40, 418-427.

Krupenie, P. H., and S. Weissman (1965), Potential-energy curves for CO and CO$^+$, *J. Chem. Phys.,* 43.

Lawrence, G. M. (1972), Photodissociation of CO_2 to produce $CO(a^3\Pi)$, *J. Chem. Phys.,* 56, 7.

Leblanc, F., and R. E. Johnson (2001), Sputtering of the Martian atmosphere by solar wind pick-up ions, *Planet. Space Sci.,* 49, 645-656.

Leblanc, F., and R. E. Johnson (2002), Role of molecular species in pickup ion sputtering of the Martian atmosphere, *J. Geophys. Res.,* 107(E2), 5010, doi:10.1029/2000JE001473.

Lee, Y., M. R. Combi, V. Tenishev, and S.W. Bougher (2012), Global dynamics of hot atomic oxygen in Mars' upper atmosphere and comparison with recent observation, *American Geophysical Union Fall Meeting 2012,* #SA51A-2146, San Francisco, CA, 3-7 December.

Lee, Y., M. R. Combi, V. Tenishev, and S. W. Bougher (2014a), Hot carbon corona in Mars' upper thermosphere and exosphere: 1. Mechanisms and structure of the hot corona for low solar activity at equinox, *J. Geophys. Res. Planets,* 119, doi:10.1002/2013JE004552.

Lee, Y., M. R. Combi, V. Tenishev, and S. W. Bougher (2014b), Hot carbon corona in Mars' upper thermosphere and exosphere: 2. Solar cycle and seasonal variability, *J. Geophys. Res. Planets,* submitted.

Liu, Y., A. F. Nagy, C. P. T. Groth, D. L. DeZeeuw, and T. I. Gombosi (1999), 3D Multi-fluid MHD studies of the solar wind interaction with Mars, *Geophys. Res. Lett.,* 26, 2,689.

Liu, Y., A. F. Nagy, T. I. Gombosi, D. L. DeZeeuw, and K. G. Powell (2001), The solar wind interaction with Mars: Results of three-dimensional three species MHD studies, *Adv. Space Res.*, 27, 1,837-1,846.

López-Valverde, M. A., D. T. Edwards, M. López-Puertas, and C. Roldán (1998), Non-local thermodynamic equilibrium in general circulation models of the Martian atmosphere 1. Effects of the local thermodynamic equilibrium approximation on thermal cooling and solar heating, *J. Geophys. Res.,* 103, 16,799-16,811.

Luhmann, J. G. (1992), Mars atmosphere evolution: Escape to space, In Lunar and Planetary Inst., Workshop on the Martian Surface and Atmosphere Through Time, 91-92.

Luhmann, J. G., and J. U. Kozyra (1991), Dayside pickup oxygen ion precipitation at Venus and Mars: Spatial distributions, energy deposition, and consequences, *J. Geophys. Res.,* 96, 5,457-5,467.

Luhmann, J. G., R. E. Johnson, and M. H. G. Zhang (1992), Evolutionary impact of sputtering of the Martian atmosphere by O^+ pickup ions, *Geophys. Res. Lett.,* 19, 2,151-2,154.

Lundin, R., et al. (1990), Aspera/Phobos measurements of the ion outflow from the martian ionosphere, *Geophys. Res. Lett.,* 17, 873-876.

Ma, Y., A. F. Nagy, I. V. Sokolov, and K. C. Hansen (2004), Three-dimensional, multispecies, high spatial resolution MHD studies of the solar wind interaction with Mars, *J. Geophys. Res.,* 109(A18), D15515, doi:10.1029/2003JA0010367.

Ma, Y, and A. F. Nagy (2007), Ion escape fluxes from Mars, *Geophys. Res. Lett.,* 34, L08201, doi:10.1029/2006GL029208.

Markelov, G. N., Y. V. Skorov, and H. U. Keller (2006), DSMC modeling of dusty innermost cometary atmosphere around non-spherical nucleus, AIAA, 2006-3392.

Matta, M., P. Withers, and M. Mendillo (2013), The composition of Mars' topside ionosphere: Effects of hydrogen, *J. Geophys. Res.,* 118, 2681-2693.

McDunn, T. L., et al. (2010), Simulating the density and thermal structure of the middle atmosphere (~80-130 km) of Mars using the MGCM-MTGCM: A comparison with MEX/SPICAM observations, *Icarus*, 206, 5-17, doi:10.1016/j.icarus.2009.06.034.

McElroy, M. B. (1972), Mars: An evolving atmosphere, *Science,* 175, 443-445.

McElroy, M. B., T. Y. Kong, and Y. L. Yung (1977), Photochemistry and evolution of Mars' atmosphere: A Viking Perspective, *J. Geophys. Res.,* 82, 28.

Mehr, F. J., and M. A. Biondi (1969), Electron temperature dependence of recombination of O_2^+ and N_2^+ ions with electrons, *Phys. Rev.,* 181, 1.

Melosh, H. J., and A. M. Vickery (1989), Impact erosion of the primordial atmosphere of Mars, *Nature*, 338. 487-489.

Morgan, D. D., et al. (2008), Variation of the Martian ionospheric electron density from Mars Express radar soundings, *J. Geophys. Res.,* 113, A09303, doi:10.1029/2008JA013313.

Nagy, A. F., M. W. Liemohn, J. L. Fox, and J. Kim (2001), Hot carbon densities in the exosphere of Mars, *J. Geophys. Res.,* 106, 21,565-21,568.

Nier, A. O., and McElroy, M. B. (1977), Composition and structure of Mars' upper atmosphere: Results from the neutral mass spectrometers on Viking 1 and 2, *J. Geophys. Res.*, 82, 28.

Öpik, E. J., and S. F. Singer (1959), Distribution of density in a planetary exosphere, *Phys. Fluids,* 2, 653, doi:10.1063/1.1705968.

Öpik, E. J., and S. F. Singer (1961), Distribution of density in a planetary exosphere. II, *Phys. Fluids,* 4, 221, doi:10.1063/1.1724432.

Pätzold, M, S. Tellmann, B. Häusler, D. Hinson, R. Schaa, and G. L. Tyler (2005), A sporadic third layer in the ionosphere of Mars, *Science,* 310, doi:10.1126/science.1117755.

Paxton, L. J. (1985), Pioneer Venus Orbiter Ultraviolet Spectrometer Limb Observations: Analysis and Interpretation of the 166- and 156-nm data, *J. Geophys. Res.,* 90, 5089-5096.

Pepin, R. O. (1994), Evolution of the Martian atmosphere, *Icarus*, 111, 289-304.

Petrignani, A., F. Hellberg, R. D. Thomas, M. Larsson, P. C. Cosby, and W. J. van der Zande (2005), Vibrationally resolved rate coefficients and branching fractions in the dissociative recombination of O_2^+, *J. Chem. Phys.,* 122, 014302.

Peverall, R., et al. (2001), Dissociative recombination and excitation of O_2^+: Cross sections, product yields and implications for studies of ionospheric airglows, *J. Chem. Phys.,* 114, 6679-6689.

Ridley, A. J., Y. Deng, and G. Tóth (2006), The global ionosphere–thermosphere model, *J. Atmos. Sol-Terr. Phy.,* 68, 8, doi:10.1016/j.jastp.2006.01.008.

Rosén, S., et al. (1998), Absolute cross sections and final-state distributions for dissociative recombination and excitation of CO^+ (v=0) using an ion storage ring, *Phys. Rev. A.,* 57, 4462.

Rosenbauer, H., et al. (1989), Ions of martian origin and plasma sheet in the martian magnetosphere: initial results of the TAUS experiment, *Nature,* 341, 612-614.

Simon, C., O. Witasse, F. Leblanc, G. Gronoff, and J.-L. Bertaux (2009), Dayglow on Mars: Kinetic modelling with SPICAM UV limb data, *Planet. Space Sci.,* 57, 1008-1021, doi:10.1016/j.pss.2008.08.012.

Smith, E. J., L. Davis, Jr., P. J. Coleman, Jr., and D. E. Jones (1965), Magnetic field measurements near Mars, *Science*, 149, 3689, 1241-1242.

Stewart, A. I. F., (1980), Design and operation of the Pioneer Venus Orbiter ultraviolet spectrometer, *IEEE Trans. Geosci. Remote Sens.,* GE-18, 65-70, doi:10.1109/TGRS.1980.350283.

Stolow, A., and Y. T. Lee (1992), Photodissociation dynamics of CO_2 at 157.6 nm by photofragment-translational spectroscopy, *J. Chem. Phys.,* 98, 3.

Strickland, D. J., G. E. Thomas, and P. R. Sparks (1972), Mariner 6 and 7 ultraviolet spectrometer experiment: Analysis of the OI 1304- and 1356-A emissions, *J. Geophys. Res.,* 77, 22.

Tenishev, V., M. R. Combi, and B. Davidsson (2008), A Global kinetic model for cometary comae. The evolution of the coma of the Rosetta target comet Churyumov–Gerasimenko throughout the mission, *Astrophys. J.,* 685, 659–677.

Tenishev, V., M. R. Combi, and M. Rubin (2011), Numerical simulation of dust in a cometary coma: Application to comet 67P/Churyumov-Gerasimenko, *Astrophys. J.,* 732, 104, doi:10.1088/0004-637X/732/2/104.

Tenishev, V., M. Rubin, O. J. Tucker, M. R. Combi, M. Sarantos (2013), Kinetic modeling of sodium in the lunar exosphere, Icarus, 226, 1538-1549, doi:10.1016/j.icarus.2013.08.021.

Torr, M. R., D. G. Torr, and R. A. Omg (1979), Ionization frequencies for major thermospheric constituents as a function of solar cycle 21, *Geophys. Res. Lett.,* 6, 10.

Tóth, G., et al. (2012), Adaptive numerical algorithms in space weather modeling, *J. Comput. Phys.,* 231, 870–903.

Valeille, A., V. Tenishev, S. W. Bougher, M. R. Combi, and A. F. Nagy (2009a), Three-dimensional study of Mars upper thermosphere/ionosphere and hot oxygen corona: 1. General description and results at equinox for solar low conditions, *J. Geophys. Res.,* 114, E11005, doi:10.1029/2009JE003388.

Valeille, A., M. R. Combi, S. W. Bougher, V. Tenishev, and A. F. Nagy (2009b), Three-dimensional study of Mars upper thermosphere/ionosphere and hot oxygen corona: 2. Solar cycle, seasonal variations, and evolution over history, *J. Geophys. Res.,* 114, E11006, doi:10.1029/2009JE003389.

Valeille, A., M. R. Combi, V. Tenishev, S. W. Bougher, and A. F. Nagy (2010a), A study of suprathermal oxygen atoms in Mars upper thermosphere and exosphere over the range of limiting conditions, *Icarus,* 206, 18-27, doi:10.1016/j.icarus.2008.08.018.

Valeille, A., M. R. Combi, V. Tenishev, S. W. Bougher, and A. F. Nagy (2010b), Water loss and evolution of the upper atmosphere and exosphere over martian history, *Icarus,* 206, 28-39, doi:10.1016/j.icarus.2009.04.036.

Verigin, M. I., et al. (1991), Ions of planetary origin in the Martian magnetosphere (PHOBOS 2/TAUS experiment), *Planet. Space Sci.,* 39, 131-137.

Vidal-Madjar, A., and J. L. Bertaux (1972), A calculated hydrogen distribution in the exosphere, *Planet. Space Sci.,* 20, 1147-1162.

Wallis, M. K. (1978), Exospheric density and escape fluxed of atomic isotopes on Venus and Mars, *Planet. Space Sci.,* 26, 949-953.

Walls, F. L., and G. H. Dunn (1974), Measurement of total cross sections for electron recombination with NO^+ and O_2^+ using ion storage techniques, *J. Geophys. Res.,* 79, 13.

Wilson, R. J. (2002), Evidence for nonmigrating thermal tides in the Mars upper atmosphere from the Mars Global Surveyor Accelerometer Experiment, *Geophys. Res. Lett.,* 29(7), doi:10.1029/2001GL013975.

Withers, P., and M. Mendillo (2005), Response of peak electron densities in the Martian ionosphere to day-to-day changes in solar flux due to solar rotation, *Planet. Space Sci.,* 53, 1402-1418, doi:10.1016/j.pss.2005.07.010.

Withers, P., M. Mendillo, D. P. Hinson, and K. Cahoy (2008), Physical characteristics and occurrence rates of meteoric plasma layers detected in the Martian ionosphere by the Mars Global Surveyor radio science experiment, *J. Geophys. Res.,* 113, A12314, doi:10.1029/2008JA013636.

Withers, P., S. W. Bougher, and G. M. Keating (2003), The effects of topographically-controlled thermal tides in the Martian upper atmosphere as seen by the MGS accelerometer, *Icarus*, 164, 14-32, doi:10.1016/S0019-1035(03)00135-0.

Yagi, M., F. Leblanc, J. Y. Chaufray, F. Gonzalez-Galindo, S. Hess, and R. Modolo (2012), Mars exospheric thermal and non-thermal components: Seasonal and local variations, *Icarus*, 221, 682-693.

Zhang, M. H. G., J G. Luhmann, A. J. Kliore, and J. Kim (1990), A post–Pioneer Venus reassessment of the Martian dayside ionosphere as observed by radio occultation methods, *J. Geophys. Res.*, 95, 14,829-14,839.

Zhang, M. H. G., J. G. Luhmann, S. W. Bougher, and A. F. Nagy (1993), The ancient oxygen exosphere of Mars – Implications for atmosphere evolution, *J. Geophys. Res.,* 98(17), 10,915.